The extended atmospheres of red supergiants

Modelling spectroscopic and interferometric observations

Gemma González i Torà

A thesis submitted in partial fulfillment of the requirements of the
Liverpool John Moores University
for the degree of Doctor of Philosophy

May, 2023

Declaration

The work presented in this thesis was carried out at the Astrophysics Research Institute, Liverpool John Moores University, and at the European Southern Observatory (ESO). Unless otherwise stated, it is the original work of the author.

While registered as a candidate for the degree of Doctor of Philosophy, for which submission is now made, the author has not been registered as a candidate for any other award. This thesis has not been submitted in whole, or in part, for any other degree.

Gemma González i Torà

Astrophysics Research Institute

Liverpool John Moores University

IC2, Liverpool Science Park

146 Brownlow Hill

Liverpool

L3 5RF

UK

Abstract

Red supergiants (RSGs) are evolved massive stars in a stage preceding core-collapse supernova. Investigating evolved-phases of these stars is key to understanding the cosmic matter cycle of our Universe, since they enrich the cosmos with newly formed elements. The work shown in this thesis has two main focuses: one of these aims is to probe the temperature dependence of RSGs on metallicity. In context, the temperatures of RSGs are thought to be a manifestation of the Hayashi limit, which fixes the minimum effective temperature a star can have while still maintaining hydrostatic equilibrium. The Hayashi limit is expected to depend on metallicity (Z) in such a way that lower-Z RSGs are warmer. This prediction could be tested by studying the average effective temperatures of RSGs in galaxies with different metallicities.

We investigate the Z-dependence of the Hayashi limit by analysing RSGs in the low-Z galaxy Wolf-Lundmark-Mellote (WLM), and compare with the RSGs in the higher-Z environments of the Small Magellanic Cloud (SMC) and Large Magellanic Cloud (LMC). We find a correlation between metallicity and the observed effective temperatures. We also compare the observations with evolutionary models, and find that while the trend is similar, there is a shift between observations and model predictions. This mismatch between observations and models could be due to wrong assumptions in the description of convection for massive stars.

Secondly, the work in this thesis succeeds on modelling the spatially extended atmospheres of RSGs, where the mass loss is initiated, by plugging in the effect of a stellar wind in a stellar structure model. The physical processes that extend the atmospheres of RSGs are still not fully understood, and remain one of the key

questions in stellar astrophysics. In this thesis, we propose a new 1D method to study the extended atmospheres of these cold stars, by adding the effect of a semi-empirical stellar wind based on observations of Betelgeuse. We then can compute the intensities, spectral energy distributions and visibilities matching the observations for the different instruments in the Very Large Telescope Interferometer (VLTI).

Specifically, the work first discusses the robustness of our results when comparing with the atmospheric structure of HD 56879 and V602 Car of published VLTI/AMBER data, comprising the wavelength range of $1.8 < \lambda < 2.5\,\mu$m. Then, we also compare our extended model to newly acquired data of AH Sco, KW Sgr, V602 Car, CK Car and V460 Car with the instruments VLTI/GRAVITY and MATISSE, that comprise a broader wavelength range ($1.8 < \lambda < 13\,\mu$m). This later work represents the most complete spectro-interferometric study up to date of RSGs. We find that our model can accurately match these observations for the first time, showing the enormous potential of this methodology to reproduce extended atmospheres of RSGs and to constrain temperature and density stratifications as well as mass-loss rates.

Publications

In the course of completing the work presented in this thesis, the following papers have been submitted for publication:

Refereed

- **González-Torà G.,** Wittkowski M., Davies B., Plez B. et al., 2023, to be submitted in A&A - *The effect of winds on atmospheric layers of red supergiants, II. Modelling VLTI/GRAVITY and MATISSE observations of KW Sgr, AH Sco and V602 Car, CK Car and V460 Car*

- **González-Torà G.,** Wittkowski M., Davies B., Plez B. and Kravchenko K., 2023, A&A, 669, A76 - *The effect of winds on atmospheric layers of red supergiants, I. Modelling for interferometric observations*

- **González-Torà G.,** Davies B., Kudritzki R. P., Plez B., 2021, MNRAS, 505, 4422-4443 - *The temperatures of red supergiants in low metallicity environments*

- Rosales-Guzman A., Sanchez-Bermudez J., Paladini C., **(incl. González-Torà G.,)** et al., 2023, accepted in A&A (arXiv:2303.00056) - *Resolving the temporal asymmetries in the closest vicinity of the M-type Mira star R Car with VLTI/GRAVITY, A K-band interferometric study*

Proceedings

- **González-Torà G.,** Wittkowski M., Davies B. and Plez B., 2022, Proceedings of the IAUS370: Winds of Stars and Exoplanets, in press - *The effect of winds in red supergiants: modelling for interferometry*

Acknowledgements

This thesis would have not been possible without the support of several people. Firstly, I would like to thank my supervisor Ben for giving me a chance when I decided to change topics of my PhD five months in. Although we have not seen each other much in person because of the whole pandemic and my ESO studentship, he has always been helpful and encouraging. He has also lifted me up when I was feeling like an impostor, and helped me remain calm when I was stressed. He also always supported me to take breaks when I was feeling overwhelmed.

I also want to thank my supervisor at ESO, Markus. First of all because he supported me when I sent him the first contact email to discuss about the studentship application. And from there on he has always been available to give me feedback and help. With patience and encouragement, he has guided my through reducing interferometric data and writing my first successful observing proposals. I really enjoyed our weekly meetings and it has been a pleasure to work together. I have learned a lot of new and interesting stuff thanks to him.

I am also very lucky to have been part of the ESO community. After a year of lockdown, I was feeling very lonely and missing support. When I arrived at ESO, I found a wonderful community of students and fellows that helped me settle in and made me feel like I was not alone. I want to thank specially Steve, for talking to me about the PhD studentship and encouraging me to apply. I also want to thank all the students at ESO for creating such a beautiful environment, in particular Steve, Tuts, Cami, Tere, Alice, Ivanna, Irene, Amanda, Giulia, Simone, Marie-Liis, Simon, Joshiwa and Samuel for all their encouragement. The crochet club

"Success is not just about hard work, it is about hard work with a side of exasperation."

Contents

List of Figures

List of Tables

Chapter 1

Introduction

1.1 Massive stars

Massive stars ($M > 8\,M_\odot$) play a crucial role in the composition and structure of the universe. During their late evolutionary stages, they produce heavy elements, chemically enriching the interstellar matter and triggering the formation of new stars and planetary systems (e.g., Spitzer, 1978; Heger et al., 2003). Moreover, their deaths leading to supernovae are important to understand the current expansion rate and evolution of the universe (e.g., Schaye et al., 2015; Crain et al., 2015).

In this chapter, we will talk about the evolution of massive stars, focusing on one of their late evolutionary stages: the red supergiant phase. We will study the internal and atmospheric structure of red supergiants, and learn about the observational tools to observe these stars. Finally, we will introduce the goals of this thesis.

1.2 Massive stellar evolution

In 1910 Ejnar Hertzsprung and Henry Norris Russell both independently created a diagram to classify the stars using their absolute magnitudes (or luminosities) and effective temperatures (T_{eff}). Later called the Hertzsprung-Russell diagram (HRD), it allowed to better understand stellar evolution, since stars follow a specific path along it during their lives. Figure 1.1 shows a simplified HRD with stars
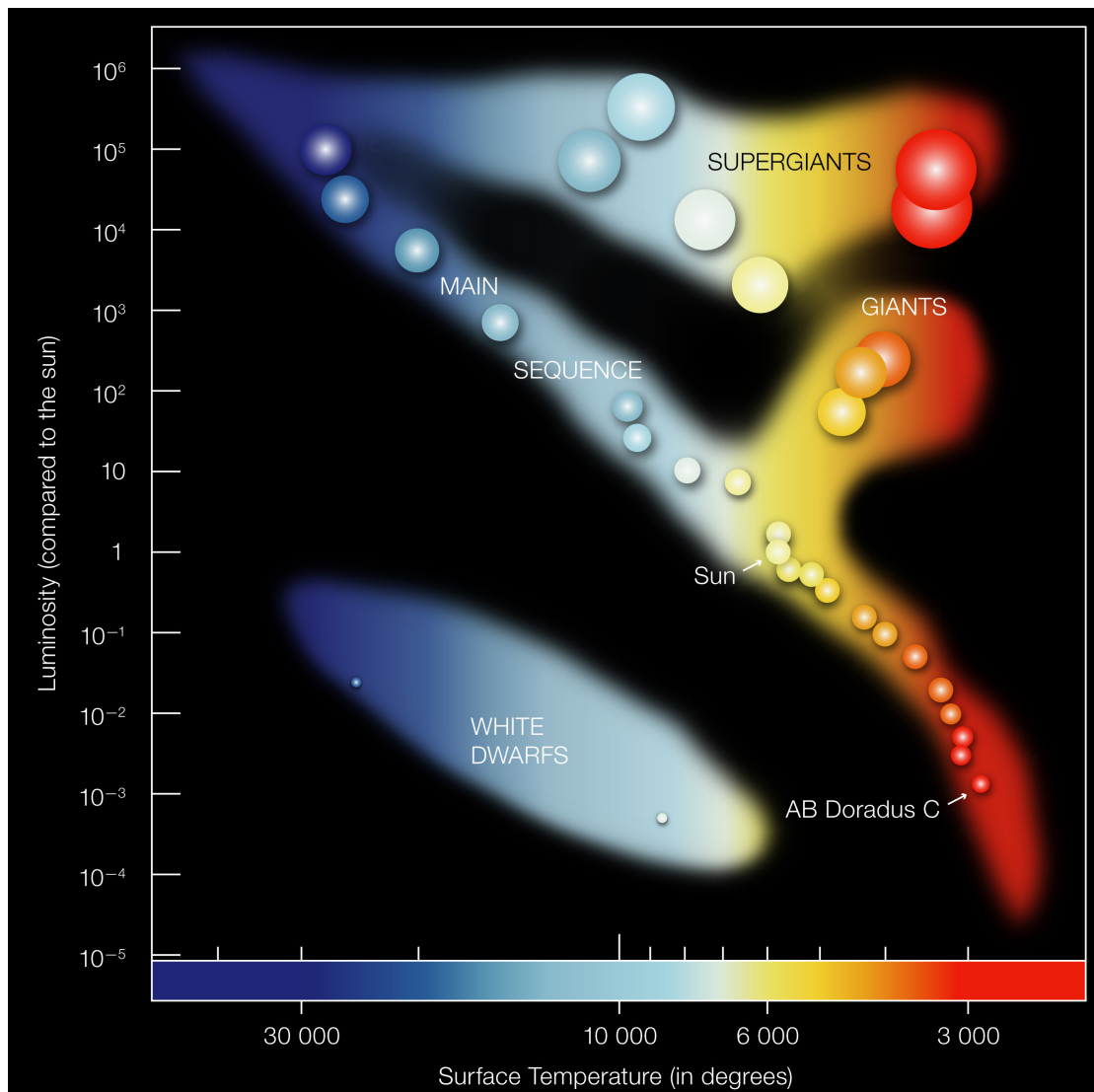
FIGURE 1.1: A simplified HRD. Credits by ESO.

in different evolutionary stages. Here, we will focus on the evolutionary path along the HRD for stars with $M > 8\,M_\odot$.

A star is formed once the hydrogen burning in the core produces enough energy to counter balance the gravitational collapse. This initial phase is called *zero-age main sequence* (ZAMS). During the rest of the *main sequence* (MS) phase, the star continues burning hydrogen in the core and producing helium. This is the longest phase on the stellar evolution of the star, about $\sim 90\%$ of its life is spent on the MS (e.g., Bertelli et al., 1994; Brott et al., 2011; Ekström et al., 2012; Meynet et al., 2015; Groh et al., 2019).

Stellar evolution is strongly affected by the initial mass of the star: while on the MS, stars with $M > 1.5\,M_\odot$ will burn hydrogen and produce helium in the

core through the so-called CNO cycle. The energy produced by the CNO cycle depends on the temperature as $\epsilon_{\mathrm{CNO}} \sim T^{16}$, while stars with $M < 1.5\,M_\odot$ produce the energy with a process that has a lower temperature dependence, $\epsilon_{\mathrm{pp}} \sim T^5$. A steeper power dependence results in convection being driven in the stellar core of massive stars. In the outer layers of the massive star (e.g., the envelope) the temperature at the surface is hot enough to ionise hydrogen, which will allow the flow of ultraviolet photons. Radiation carries then the energy in the envelope of massive stars (Hansen et al., 2012).

As the hydrogen in the core gets exhausted, the energy production stops. The core of the star will contract and to conserve potential energy, the envelope will expand (known as the *mirror principle*). As the star expands, the T_{eff} will decrease; the star will then move to the cool side of the HRD. This stage is schematically represented as the *supergiants* cluster in Figure 1.1. The star then crosses the HRD on a thermal time scale ($\sim 10^3 - 10^4$ years Meynet et al., 2015), which is very short compared to its overall lifetime. Due to this short timescale, as the star crosses the HRD there is no loss of energy and the expansion of the envelope happens quasi-adiabatically. During this stage, the star has a smooth transition to helium core burning. This helium core is surrounded by a radiative hydrogen shell and a convective envelope.

While the temperature in the envelope decreases, the opacity rises, making it harder for the radiative energy transport to occur. The envelope becomes unstable to convection and a large fraction of its mass will become convective. The star is then located at the coolest side of the HRD, becoming highly convective while still maintaining hydrostatic equilibrium. This region of the HRD is know as the Hayashi limit (Hayashi and Hoshi, 1961).

1.3   Red supergiants

Red supergiants (RSGs) are evolved stars thought to be at a stage preceding core-collapse supernova (SN). They have luminosities of $\sim 10^{4.39-5.53}\,L_\odot$ (e.g., Davies et al., 2018a; McDonald et al., 2022), a typical temperature range of $T_{\mathrm{eff}} \sim 3400 - 4500\,\mathrm{K}$, and comparing with evolutionary models by Georgy et al. 2013, a mass range of $\sim 8-25\,M_\odot$. Their luminosities are so high that they are comparable with those of globular clusters or dwarf galaxies.
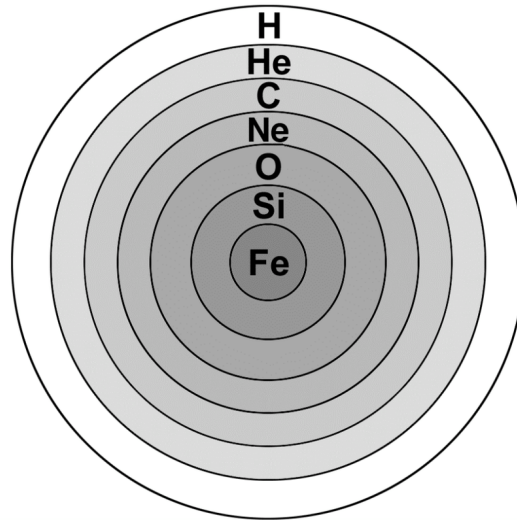
FIGURE 1.2: The onion-like structure at the core during the end evolution of a RSG. Credits by NASA.

A massive star moves all the way to the right side of the HRD while smoothly starting a helium core burning phase. As the helium core grows, the core temperature increases and the star becomes brighter and bigger. The RSG phase starts. The evolution to the RSG phase will depend on the various physical processes involved in the evolution of massive stars such as convection, rotation, mass loss, metallicity and binary interaction (see Farrell et al., 2022).

Eventually, the helium in the core will be depleted and fused into carbon, leaving the RSG with hydrogen and helium burning shells surrounding the core. The nuclear burning will fuse heavier elements in the core leaving different shells of elements until iron is produced. These different shells of elements form an onion-like structure at the centre of the RSG. Figure 1.2 shows an schematic representation of this onion-like structure. At the iron production stage, no further elements can be fused and the star will stop thermally supporting itself, causing a gravitational collapse. This will produce a core collapse SN explosion.

We now focus on explaining both the internal and atmospheric structure of RSGs, prior to their end evolutionary stages and core collapse.

1.3.1   Internal structure

As the star becomes cooler, the convective region increases to the point that RSGs are highly convective stars. Accurately describing stellar convection processes requires an in depth knowledge of 3D magneto-hydrodynamical processes, which requires extreme computational power (e.g, Freytag et al., 2010; Ahmad et al., 2023). Most stellar evolution codes need a faster and less computationally demanding way to describe stellar convection. An approximation to describe convection is the *mixing length theory* (MLT).

1.3.1.1   The Mixing Length Theory (MLT)

The MLT (Böhm-Vitense, 1958) is a rough approximation to describe the convective region of stars. It assumes that a fluid parcel can travel a distance l before dispersing into the surrounding material, l is defined as:

$$l = \alpha H_p \tag{1.1}$$

where α is the so called mixing length parameter and H_p is the pressure scale height, defined as $H_p = P/(\mathrm{d}P/\mathrm{d}r)$ (Prandtl, 1925) where P is the total pressure of the gas and r the distance. Therefore, H_p is defined as the distance over which the pressure decreases by a factor of e.

Figure 1.3 is an artist representation of the principle behind the MLT: a bubble or parcel rises and travels a distance l before dissolving with the surrounding medium. As the bubble rises, it maintains pressure equilibrium with its surroundings. Since the parcel starts to rise at a higher heat content than where it dissolves, heat will be transported from the starting position to a level with height l.

Although it is a very rough approximation that does not take into account 3D effects, relies on flimsy assumptions and a non-physical free parameter α which is hard to calibrate (see e.g., Chun et al., 2018), the MLT has been widely used to describe stellar interiors. However, this theory comes with some difficulties. The most important problem is the proper calibration of α, since we need a good knowledge of the stellar interior to find an accurate value. A solar-like mixing length parameter $\alpha_\odot$ has been assumed for all stellar structure and evolutionary codes, despite some studies arguing against the accuracy of this assumption (Chun
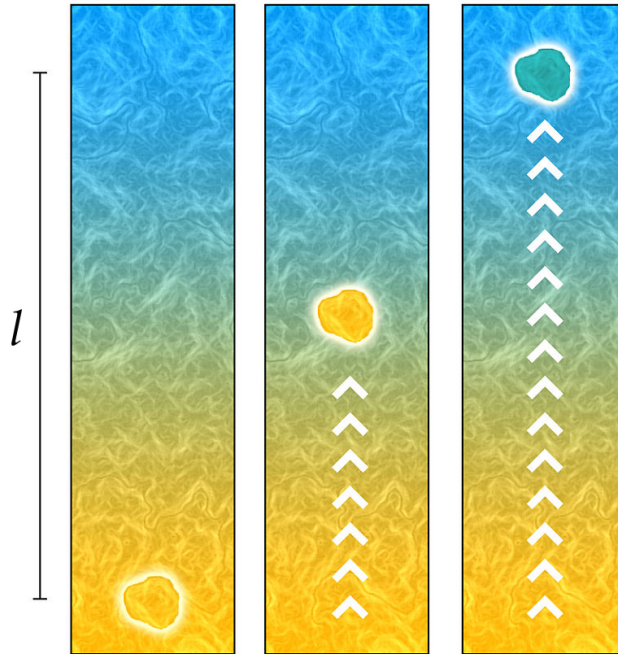
FIGURE 1.3: The principle of the MLT: a bubble or parcel travels upwards a distance l until it dissolves and transfers energy. Credits by Nedtheprotist.

et al., 2018; González-Torà et al., 2021, see Chapter 2). Assuming a different $\alpha_\odot$ for massive stars will have consequences on evolutionary tracks, as well as on model-determined stellar parameters such as the T_{eff} and stellar colours. This means that integrated stellar populations such as galaxies or clusters, where red light of such stars dominates, will also be affected. One of the goals of this thesis is studying the limitations of the MLT in RSGs (see Chapter 2).

1.3.2   Metallicity dependence

Theoretical predictions show a dependency between the Hayashi limit and the metallicity (Z) of RSGs (see for instance the series Meynet and Maeder, 2000, 2002; Maeder and Meynet, 2001, where stellar evolution in low metallicities has been extensively studied). The Hayashi limit (Hayashi and Hoshi, 1961) fixes the minimum T_{eff} of the star and its maximum radius, where the star is known to have their most extended convective region and still maintaining hydrostatic equilibrium.

A possible explanation to this Z dependency from a physical point of view could be the following: when the star has a lower metallicity, it means that its opacity

is also lower. In consequence, the energy radiated can escape more efficiently. Therefore the star will be smaller and hotter for the same luminosity. As the star leaves the MS, since the temperature at the core is hotter, it does not need to contract as much to reach a high enough core temperature to ignite helium. The star does not contract as much, so it stays on the left side of the HRD, and therefore appears overall warmer (e.g., Choi et al., 2016; Dotter, 2016).

Figure 1.4 shows the evolutionary tracks for a star of initial mass $10\,M_\odot$ and different metallicities, from the ZAMS up to the end of the red giant branch (RGB) using the MESA Isochrones and Stellar Tracks (MIST) by Choi et al. (2016) and Dotter (2016). We observe in Figure 1.4 that there is a trend for stars of lower metallicities to move to the right of the HRD, hence to warmer temperatures on the RGB.

The Hayashi limit is a representation of the T_{eff} for RSGs. Levesque et al. (2005) studied RSGs in the Large Magellanic Cloud (LMC) and Small Magellanic Cloud (SMC) and found their T_{eff} to be cooler than the Galactic by $50 - 150$ K. To obtain the T_{eff} of RSGs, Levesque et al. (2005, 2006) performed spectroscopic analysis by fitting the TiO lines, since for cold stars it is the most prominent feature in their spectra. Follow-up studies at the Magellanic Clouds (MCs) by Levesque et al. (2007a,b) also determined the stars to be colder, and therefore on the right of the Hayashi track. The targets found by Levesque et al. where located at the "forbidden zone", where the star could no longer hold equilibrium. The unexpected cold temperatures were justified by their variable extinction (since RSGs suffer dramatic changes on monthly timescales), their supersonic velocities, poor knowledge of RSGs molecular opacities and possible contamination by stars in the Milky Way Halo (Levesque et al., 2007b).

However, it appears that this determination method using the TiO lines underestimates the temperature of those stars, appearing cooler than expected. This is not the case when using the spectral energy distribution (SED) line-free continuum regions in the NIR (Davies et al., 2013b) instead of TiO, where the stars show consistent temperatures. A more in-depth study trying the reconcile both temperature determination methods is discussed in Section 5.2 of Davies et al. (2013b), where they first explore the effects of changing the metallicity and CNO abundances of the model grid. They conclude that these two variables cannot explain the discrepancy between using the TiO band regions and the NIR continuum of
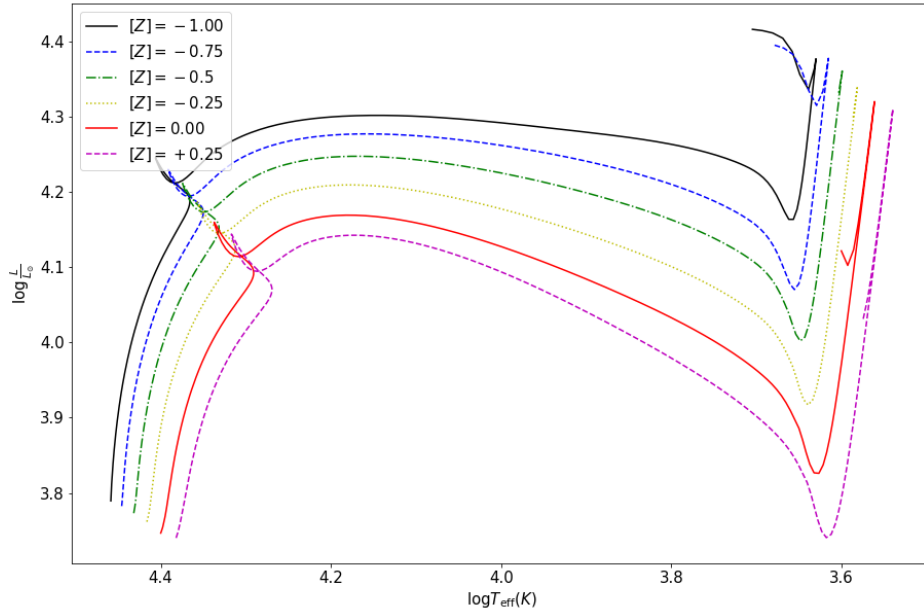
FIGURE 1.4: Evolutionary tracks for a $10\,M_\odot$ star without rotation and different metallicities by Choi et al. 2016 and Dotter 2016.

the spectra. In contrast, they argue that the temperature structure is slightly different when not taking the 3D effects into account. This results in the TiO bands being formed in outer layers of the atmosphere, and therefore shifting towards larger radii and lower temperatures than the SED regions. In the SED regions, the optical depth $\tau \approx 1$ and the continuum is formed, and has no discrepancies between the 1D and 3D temperatures. Finally, they suggest that another reason why the star appears cooler when performing the TiO band fit method could be the effect of the stellar wind. The strength of the molecules may depend on wind density in that case (Davies and Plez, 2021).

In Chapter 2 we explore this $Z - T_{\text{eff}}$ dependence with the Hayashi limit, as well as the different T_{eff} determination methods more in depth.

1.3.3   Stellar winds

Stellar winds impact the lives of massive stars and can also change their evolutionary path along the HRD. RSGs eject part of their material in the form of stellar winds, extending their atmospheres by several stellar radii. At around $R \sim 8\,R_\star$,

the temperature of the ejected material is cold enough ($T < 800$ K) so that the dust grain contribution becomes predominant (Gail et al., 2020). Therefore, when we observe the atmosphere of RSGs there will be several components present: the compact stellar atmosphere up to the photosphere, followed by an atmospheric extension of ejected gas, ending with a dust shell of material surrounding the star at several stellar radii.

There have been several initial attempts to explain the mechanism of stellar winds in RSGs (e.g. Salasnich et al., 1999; Josselin and Plez, 2007), but there is still no consensus. Current modelling attempts to reproduce atmospheric extension include the addition of a thin static molecular shell (or 'MOLsphere', e.g., Perrin et al., 2007; Ohnaka et al., 2009, 2011; Montargès et al., 2014; Kervella et al., 2018) or 3D radiative hydrodynamics studies but that are not sufficiently extended for RSGs (e.g., Chiavassa et al., 2009, 2010, 2011b,a). Recent work by Kee et al. (2021) studied the possibility of turbulent atmospheric pressure in initiating and determining the mass-loss rates ($\dot{M}$) of RSGs, finding promising results. However, there is still no dynamical model available that succeeds to reproduce mass-loss events (Arroyo-Torres et al., 2015; Montargès et al., 2021; Humphreys and Jones, 2022; Dupree et al., 2022). Therefore, further work is needed to unambiguously determine the dynamical processes that trigger massive star wind events in spatially extended atmospheres.

Stellar winds can also occur in the form of localised events, where the RSG ejects material inhomogeneously. Arguably, one of the most famous localised events to date is the great dimming of Betelgeuse during the start of 2019 (Guinan et al., 2019; Dupree et al., 2020; Dharmawardena et al., 2020), where the visual brightness of the RSG decreased by 0.6 magnitudes. Various studies revealed that the most likely cause of its dimming was a mass-loss event in the southern hemisphere of the star (Montargès et al., 2021; Dupree et al., 2022).

1.3.4 Mass loss

Mass-loss events become important as a massive star leaves the main sequence phase (Chiosi and Maeder, 1986). For this reason, one of the key stages for mass loss is the RSG phase. These mass-loss events occur in the extended atmospheres of RSGs. As already mentioned, the observed extensions are not at all reproduced by current dynamic model atmospheres.

The mechanism that triggers mass loss of RSGs is still poorly understood. As a consequence, their $\dot{M}$ can not be derived from first principles. This is not the case for their low- and intermediate-mass counterparts (Miras), whose mass-loss processes can be explained by pulsation and dust-driven winds alone (Wood, 1979; Bowen, 1988; Höfner and Olofsson, 2018).

Hence, there have been few studies that explore the mass-loss effect in cool massive stars, with most of them focusing on their spectra. Most explore the mid- and far-IR region, where the dust component is dominant (e.g. Groenewegen et al., 2009; Beasor and Davies, 2018; Decin et al., 2006; De Beck et al., 2010). Therefore, the models rely on dust modelling, such as DUSTY (Ivezic and Elitzur, 1997; Ivezic et al., 1999) or RADMC3D (Dullemond et al., 2012).

Recently, Davies and Plez (2021) explored the extension of the atmospheres close to the stellar surface at radii smaller than the inner dust shells in the optical and near-IR. Adding the influence of a stellar wind in the MARCS model atmospheres (Gustafsson et al., 2008), Davies and Plez (2021) expanded the atmosphere up to several stellar radii. Their results naturally explained the presence of a mid-IR excess, as well as the mismatch between temperatures derived from the optical and the IR (Levesque et al., 2005; Davies et al., 2013b; González-Torà et al., 2021). They also reproduced many of the features obtained by the addition of a static molecular shell (or 'MOLsphere'). In short, the work by Davies and Plez (2021) opened a new window to explore the $\dot{M}$ of cool massive stars.

In Chapters 3 and 4, we explore the effect of the new modelling approach by Davies and Plez (2021) comparing not only with stellar spectra, but also with interferometric data that spatially resolves the photosphere and extended layers. The principles of these different observational techniques will be introduced in the next section.

1.4   Observation techniques

Bellow there is a brief summary of the main observation techniques for astronomical objects, and more specifically, RSGs.

1.4.1 Photometry

Briefly, photometry measures the intensity of light of astronomical objects. The maximum intensity will correspond to its peak black-body emission (Kirchhoff, 1862), but we can use different photometric filters to observe the wavelengths that we are most interested in.

1.4.1.1 Photometric diagnostics

The bolometric luminosity of a RSG is a fundamental parameter that can be derived by using photometric data in several bands. In Chapter 2, we use synthetic and available photometric data from the SIMBAD database (Wenger et al., 2000) in different filters to estimate the luminosities of our newly observed targets. Briefly, if the extinction is known, we can deredden the magnitudes and convert them to flux. Then, we integrate over the wavelength range for all the photometric filters available to obtain a bolometric flux. Finally, the bolometric luminosity can be obtained when using the distance to the star from Earth. The extinction can be calculated using spectroscopic data: if we know the intrinsic colour of the star, by estimating the surface gravity ($\log g$) and T_{eff} from a spectrum and comparing with the dereddened spectrum of the star. The distance can be found with several methods, such as using the Gaia parallax determinations for the Milky Way stars (Gaia Collaboration et al., 2018), or A and B-type star spectra for extragalactic stars (Urbaneja et al., 2008; González-Torà et al., 2022).

Mass-loss measurements are also derived mainly from mid-IR photometry (e.g., Beasor et al., 2020). The dust emission from the RSG is shown in the mid-IR excess and is compared to dust shell models such as DUSTY (Ivezic et al., 1999), a radiative transfer code that assumes a 1D dust shell obscuring the star. However, $\dot{M}$ determinations using mid-IR photometric excess come with several assumptions such as the dust to gas ratio and composition that lead to big uncertainties. Chapters 3 and 4 explore a new $\dot{M}$ determination method that does not use mid-IR photometry.
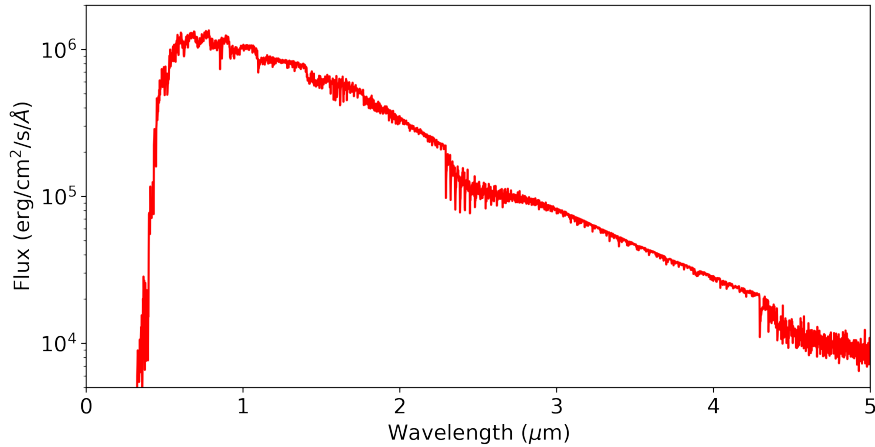
FIGURE 1.5: The spectrum of a RSG using the MARCS models and the stellar parameters $T_{\mathrm{eff}} = 4000$ K, surface gravity $\log g = 0.0$, mass $M = 15\,M_{\odot}$, and microturbulence $\xi = 5$km/s. The spectrum comprises the wavelength range from the optical to the thermal-IR, with a spectral resolution of $R = 1500$.

1.4.2 Spectroscopy

In addition to just observing the color of the star using different filters, we can make its light pass through a dispersing element, e.g., a prism, to obtain the spectrum of the atmosphere of the star. The continuum radiation will have a similar shape as a black-body spectrum. However, due to the presence of electrons, atoms and molecules in the atmosphere of the star, the photons observed will have several interactions with matter. The most important interactions are the bound-bound, bound-free and free-free. There are also other interactions with matter that shape the spectra such as the electron scattering or the presence of H^- and molecules. The reader is referred to stellar atmospheric and radiative transfer books for more details on the opacity sources (e.g., Mihalas, 1978; Rybicki and Lightman, 1979). Accounting for all these interaction processes, we obtain a spectrum like in Figure 1.5.

1.4.2.1 Spectral diagnostics

The first fundamental parameter that can be derived from the spectra is the T_{eff}. As previously mentioned, Levesque et al. (2005, 2006) obtained spectrophotometric data of a sample of RSGs in the Milky Way and the Magellanic Clouds (MCs) in the optical to near-IR region of the spectrum, where the TiO molecular bands are present ($4000\mathring{A} < \lambda < 9500\mathring{A}$). Levesque et al. also define the spectral

classification of the RSG using the TiO molecular bands. They compared the SED of the observations with MARCS atmospheric models fitting for the best $T_{\rm eff}$ to the TiO lines, and then adjusting the reddening values $E(B-V)$ to produce the best fit to the continuum. However, we already mentioned that the temperatures found underestimated the $T_{\rm eff}$ by $50-150$ K (i.e. Section 1.3.2). A new determination method for $T_{\rm eff}$ was explored by Davies et al. (2013b) focused on fitting the line-free continuum regions of the SED to MARCS model atmospheres (see Table 2.2 in Chapter 2 for the specific regions used). Davies et al. (2013b) found warmer temperatures and also higher extinctions, $A_{\rm V}$. In Chapter 2 we use the method of Davies et al. (2013b) to find $T_{\rm eff}$ and $A_{\rm v}$ for a sample of RSGs in the MCs and in the galaxy Wolf-Lundmark-Mellote (WLM).

The metallicity of the star can be also found by studying the absorption lines in the J band. Davies et al. (2010) introduced a technique to derive chemical abundances from RSG spectra in the J band for low resolutions ($R \sim 2000-3000$). Using the spectral metallic lines of Fe I, Mg I, Si I and Ti I to compare with MARCS models, they derive chemical abundances as well as $T_{\rm eff}$, $\log g$ and microturbulences (ξ). With this technique, not only the metallicity of the star is derived, but also the abundance probes of their host galaxies, such as the Sculptor Galaxy NGC 300 (Gazak et al., 2015), the MCs (Davies et al., 2015), NGC 4038 (Lardo et al., 2015) or massive star clusters in M83 (Davies et al., 2017).

Mass-loss rates can also be determined by molecular emission lines such as CO (De Beck et al., 2010) or atomic lines (Sanner, 1976). However, these methods have high degrees of uncertainties due to the relatively low CO presence in stellar winds and the numerous assumptions about the physical properties of the stellar wind. In Chapter 4, we use both spectra and interferometry on a new method to estimate $\dot{M}$ not only using CO, but also several other molecules such as SiO and water.

1.4.3   Interferometry

The angular resolution of a telescope, θ, is defined by:

$$\theta = \frac{\lambda}{D} \qquad\qquad (1.2)$$

where λ is the observing wavelength and D the diameter of the telescope. Arguably, as we increase the λ the D of the telescope should also increase to preserve the same θ. Equation 1.2 will gain importance as we move to the IR or longer λ, or simply if we want a resolution high enough to resolve finer details of our source. Since increasing the D of the telescope comes with technical difficulties, a feasible solution is to use an array of telescopes instead.

Interferometry uses an array of telescopes to increase the angular resolution of the observations. The array of telescopes will synthesise a larger aperture telescope. The resolution of the interferometer will be given by the distance between its individual array components. This distance between array elements is called *baseline*, B.

Instead of directly measuring the intensity of a star, the interference pattern created by combining the light of the array telescopes is measured. This interference of light creates fringes with a resulting pattern of alternating dark and light bands. The fringes will contain the information about the observed source (e.g., size, shape, brightness) as seen in more detail in the next section. The observables derived from the fringe pattern are the *complex visibilities*. The relation with the *complex visibility* of an object and its brightness distribution is described by the *van Cittert-Zernike theorem*. Briefly, the theorem relates the complex visibility of a source with the normalised Fourier transform of the brightness distribution of that source. The expression resulting from the theorem is written as:

$$I(\alpha, \beta) = \int \int V(u, v) \exp^{i2\pi(\alpha u + \beta u)} \mathrm{d}u \mathrm{d}v, \tag{1.3}$$

where $V(u, v)$ is the complex visibility, u and v are the components of the vector baseline between the two sampling points projected onto a plane perpendicular to the source direction and measured in wavelengths. Quantities u and v are called *spatial frequencies* and can be defined in terms of the baseline components $u = B_x/\lambda$ and $v = B_y/\lambda$. $I(\alpha, \beta)$ is the brightness distribution of the object, while α and β are the angular coordinates in radians.

The complex visibility obtained from the fringes is composed of an *amplitude* and *phase*. The amplitude is a measure of the fringe contrast, related to the maximum and minimum intensities of the fringe pattern,

$$V = \frac{I_{\max} - I_{\min}}{I_{\max} + I_{\min}}. \tag{1.4}$$
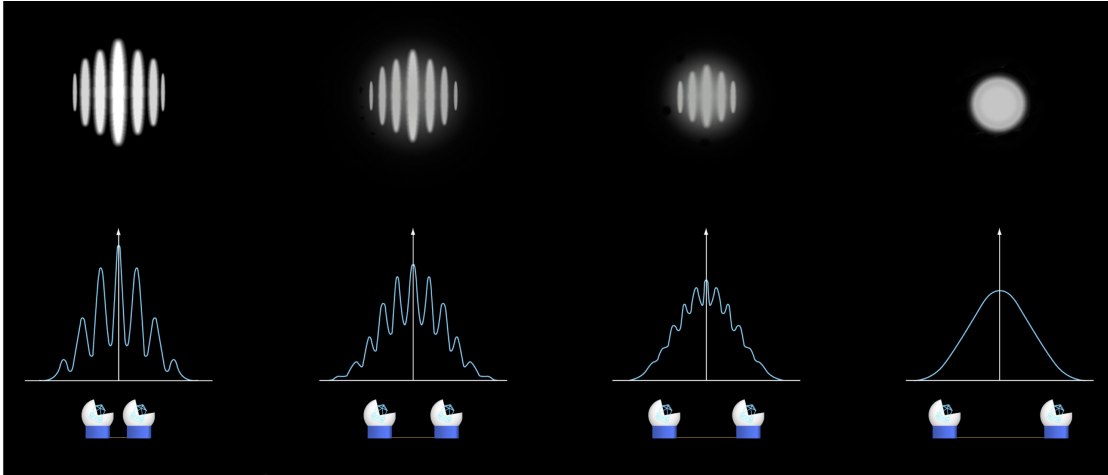
FIGURE 1.6: Interferometric observations of a single star. As we increase the distance between the telescopes, the fringe pattern changes. Credit by ESO.

This expression means that when $V = 1$, $I_{\min} \sim 0$, so the dark bands in the fringe pattern would go to zero and the object is unresolved. When $V < 1$ means that the fringe contrast decreases, and the object becomes resolved.

Figure 1.6 shows the interferometry pattern for an observed single star as we increase the distance between the two telescopes, or baseline. The fringe pattern changes as we increase the baseline.

Depending on the length of the baseline, we will obtain different information on the scale structure of the object. As an example, Figure 1.7 shows a visibility curve with respect to the baseline and the reconstructed image for the case of a star surrounded by a dust shell. The main point is that the small baselines resolve the large scale structure of the object (so the dust shell), while the longer baselines resolve the smaller structure, so the inner star.

The second observables are the fringe phases, which are related to the position of the fringe pattern. However, due to atmospheric events such as turbulence, the phases become corrupted. To solve this problem, we define the *closure phase* by combining the phases measured in a triangle of three telescopes. In this way, the phase errors introduced in the telescopes produce an equal but opposite phase shift so that the effect of the atmospheric turbulence is cancelled. The closure phase is measured from 0 to 2π. A 2π phase corresponds to an offset of a whole fringe period. The closure phase will be sensitive to possible asymmetries in the source distribution (Monnier, 2007). More examples are shown in the next section. The
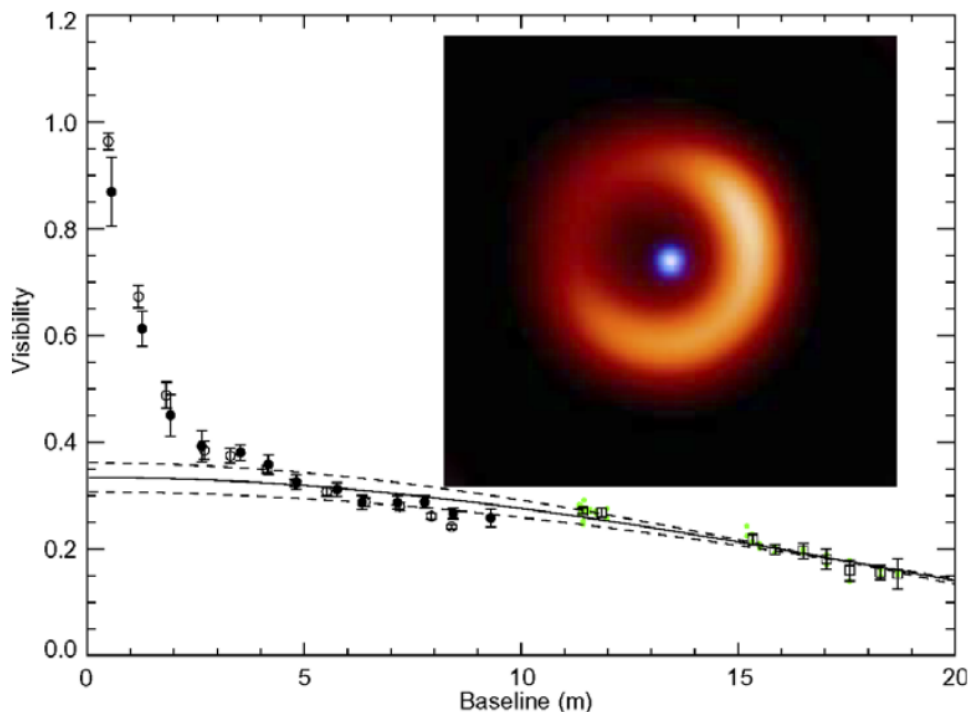
FIGURE 1.7:   Visibility curve and the corresponding image of the star with
a dust shell.   The black and white dots represent the visibilities taken with
different baselines for the observation. The solid black line is a simple model to
fit the large baseline observations, while the dashed lines represent the errors
of the model. The main takeaway is that the small baselines resolve the larger
structures so the dust shell, while the long baseline resolves the smaller star.
Figure taken from Monnier (2007).

combination of closure phases and amplitudes from a well sampled visibility plane
allows to reconstruct the image of an object.

1.4.3.1   Diagnostics with interferometry

The first fundamental parameter derived from interferometry is the brightness
distribution, as it can be found directly by definition from the *van Cittert-Zernike*
theorem and Equation 1.3. As mentioned, the shape of the source is shown by the
closure phases. More specifically, the closure phases will indicate asymmetries of
the source. For example, a source that is not point symmetric will have a closure
phase different from zero or π. For clarity, we introduce examples of reconstructed
images of resolved stellar objects with interferometry data.

Figure 1.8 shows the interferometric data and reconstructed image for the young
stellar object MWC 349 by Danchi et al. (2001). The top left panel shows the
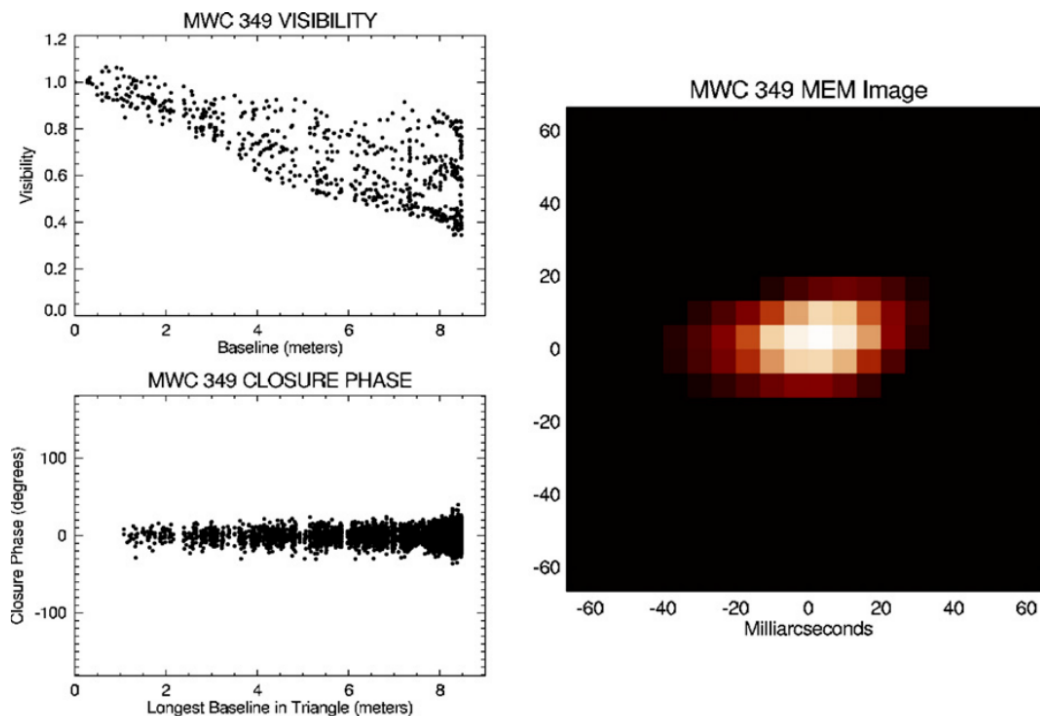
FIGURE 1.8: Visibilities, closure phases and reconstructed image of the young stellar object MWC 349. Figure taken from Monnier (2007).

visibilities, while the lower left panel shows the closure phases. We can see that the visibilities show different values for a single baseline depending on the position angle. This means that we do not have a point source and that the object is elongated. The closure phases are close to zero, so the source is axi-symmetric. Indeed, once we reconstruct the image, the right panel in Figure 1.8 shows that we are observing an edge-on disk.

Figure 1.9 shows another example of a reconstructed image by obtaining the visibilities and closure phases of an interferometric observation. The object observed is LkHα 101 by Tuthill et al. (2001). In this case, while we still have different visibilities for a single baseline, there is no difference in the spread of the values for long or short baselines. This indicates that the object is spherical. When we look at the closure phases, the values vary from the zero vicinity at long baselines, so the source is asymmetrical in small scales. The reconstructed image on the right of Figure 1.9 is consistent with the interferometric data: an emission ring which is brighter on one side.

Interferometry also allows for the determination of other fundamental stellar parameters such as the angular diameter, linear size and T_{eff}. The angular diameter
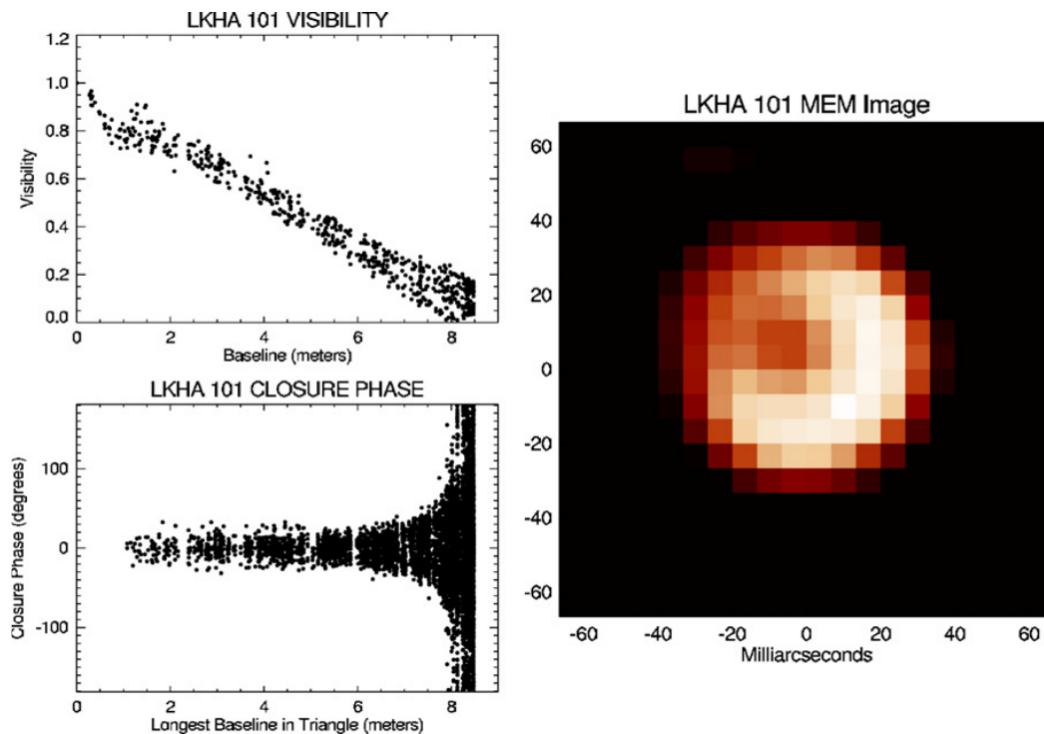
FIGURE 1.9: Visibilities, closure phases and reconstructed image of the young stellar object LkHα 101. Figure taken from Monnier (2007).

of a star can be derived with:

$$V = \frac{2J_1(x)}{x}, \text{ with } x = \frac{\theta_{\mathrm{UD}}\pi B}{\lambda}, \tag{1.5}$$

where V is the visibility, J_1 is the first-order Bessel function, θ_{UD} the angular diameter of an equivalent uniform stellar disk, B the baseline, the constant π and wavelength λ (van Belle, 2015). As we have seen, for some objects a uniform disk approximation is not accurate, but for single stellar objects it is a good initial approximation. In Chapters 3 and 4 we estimate the angular diameter of our observations.

From the angular diameter θ, the linear size of the star can be found by simply knowing the parallax π and the relation $R = \pi\theta$, where R is the linear radius. From this radius definition and by applying the definition of luminosity or bolometric flux F_{bol}, we can obtain the T_{eff} (van Belle, 2015),

$$T_{\mathrm{eff}} \propto \left(\frac{F_{\mathrm{bol}}}{\theta^2}\right)^{1/4}. \tag{1.6}$$
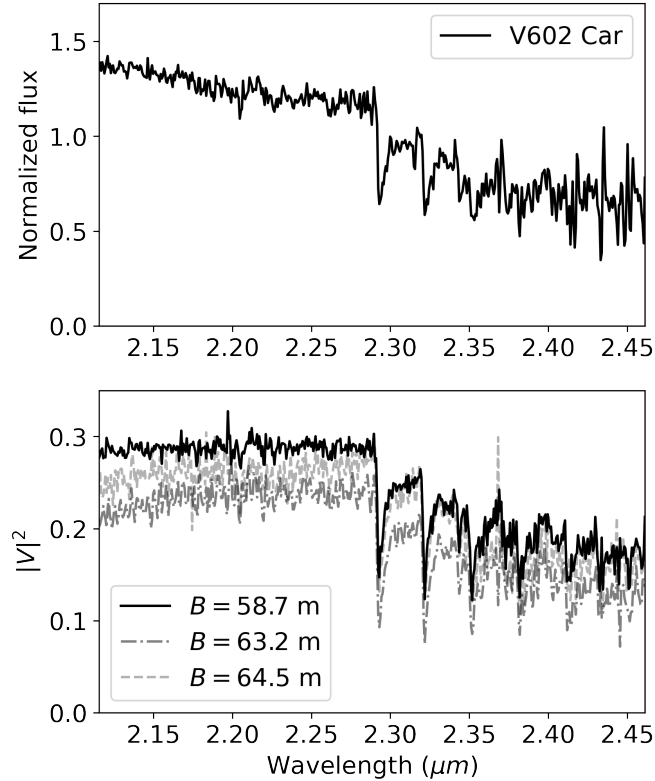
FIGURE 1.10: Spectra (*top panel*) and $|V|^2$ (*lower panel*) as a function of wavelength for the RSG V602 Car, taken with VLTI/AMBER. The three different $|V|^2$ curves where taken each with a different baseline. Adapted from Arroyo-Torres et al. (2015).

This measurement would be independent from the other spectroscopic measurements of T_{eff} such as Levesque et al. (2005); Davies et al. (2013b).

Finally, in this thesis we use both spectra and interferometry to derive $\dot{M}$, by modelling the effect of a stellar wind in the extended atmosphere of a RSG. Spectro-interferometry allows to simultaneously obtain the spectra, visibilities and closure phases as a function of wavelength. An example is seen in Figure 1.10, adapted from Arroyo-Torres et al. (2015): the spectra and squared visibility amplitudes as a function of wavelength are shown for VLTI/AMBER data of the RSG V602 Car, comprising the wavelength range of $2.1 < \lambda < 2.5\,\mu\text{m}$.

In this thesis, we have focused in spectro-interferometric observations. For the case of spectro-interferometry, we do not reconstruct the image. The reason is that the data taken is a *snapshot*: the concatenations are standalone without aiming to fill the *uv* plane. The *uv* plane is where the spatial frequencies are defined. For the examples in Figures 1.8 and 1.9, the type of data was taken as *imaging*: a set of concatenations with different baseline configurations to uniformly fill the *uv*

plane. Since we do not have enough information in the uv plane (i.e. we did not fill the plane with enough observations in different baselines), we cannot reconstruct the image. We also do not use the closure phases in this thesis, firstly because of the low uv plane coverage, but also because we are interested in 1D modelling the extension of the atmosphere for different wavelengths, without studying the asymmetries.

Despite not allowing for image reconstruction, snapshots present several advantages. The most important is that the exposure time of the observations is faster than imaging. The second is that snapshots can probe already the structure of the atmosphere for different wavelengths. That is, different spectral features form at different depths in the atmosphere. This difference in depths is shown in the shape of the $|V|^2$. Indeed, in Figure 1.10 we already see a correlation between the CO absorption lines in the flux at the $2.25 < \lambda < 2.45\,\mu$m region (upper panel) and the $|V|^2$ in the same region. The correlation is even more evident in Chapters 3 and 4. Our modelling, analysis and results of using spectro-interferometry to probe the structure of the atmosphere of RSGs are shown in Chapters 3 and 4.

We have introduced the basics behind the theory of interferometry and its diagnostics. In the next section, we will briefly comment on the characteristics of the instruments used to preform interferometric observations in this thesis.

1.4.3.2   VLTI

The Very Large Telescope Interferometer (VLTI) comprises the four Unit telescopes (UTs) and the four Auxiliary Telescopes (ATs) of the VLT as the light collecting elements of the interferometric array. The VLTI instruments recombine the light from the four ATs or UTs simultaneously. Currently, the VLTI has three operational instruments: PIONIER (Le Bouquin et al., 2011), GRAVITY (Gravity Collaboration et al., 2017) and MATISSE (Petrov et al., 2007). For this thesis, we have used data of both GRAVITY and MATISSE. The GRAVITY and MATISSE data has been obtained, reduced and analysed by the author and comprises the observing proposals with IDs 109.231U, 11023NZ (co-I) and 110.23P1 (PI). We have also used published data of AMBER (Petrov et al., 2007), which was decommissioned in 2018.

FIGURE 1.11: The VLT in ESO Paranal, the Unit telescopes and Auxiliary telescopes get arranged to create the VLTI. In the middle lies the VLTI laboratory. Credit by ESO/G.Hüdepohl.

- **GRAVITY:** GRAVITY is an interferometer of the VLTI (Gravity Collaboration et al., 2017) optimised for the K band, comprising the wavelength range of $1.8 < \lambda < 2.4 \, \mu$m. By combining the four telescope beams of the VLTI, it can perform both interferometric imaging and astrometry by phase referencing. The VLTI UTs form an equivalent diameter of 130 m and a collecting area of 200 m². The GRAVITY instrument has two different modes: the split polarisation mode splits the light into two polarisation angles and increases the internal fringe contrast, the combined polarisation mode increases the sensitivity of the instrument instead. Our observations are bright enough allowing for no sensitivity constraints, so we chose the split polarisation mode. We average the two polarisation modes so we do not use polarimetry data in this thesis, we only use the split polarisation mode to increase the internal fringe contrast.

- **MATISSE:** The Multi AperTure mid-Infrared SpectroScopic Experiment (MATISSE, Lopez et al., 2014) is a mid-IR spectro-interferometer combining four beams of the VLTI. The instrument is optimised for the L, M and N bands, comprising a wavelength range of $3.2 < \lambda < 13 \, \mu$m. For each spectral band, MATISSE uses a beam combiner, where the four separated telescope beams are focused in a detector, producing six dispersed fringe patterns mixed into a single focal spot. For the L and M bands, MATISSE

uses the SiPhot photometric mode, where the photometry is measured simultaneously with the dispersed interference fringes. This mode allows to properly calibrate the visibilities. For the N band, the photometric measurement mode is obtained separately after the interferometric observations, allowing to improve the sensitivity by sending the total flux in the different channels (high sens mode). Recently, a new mode designated for faint targets uses the GRAVITY instrument as a fringe-tracker, called GRAVITY for MATISSE (or GRA4MAT, Lopez et al., 2022). This new mode provides improved sensitivities for the ATs and increases the spectral coverage.

- **AMBER:** The Astronomical Multi-BEam combineR (AMBER, Petrov et al., 2007) was a spectro-interferometer that operated in the J, H and K bands, comprising the wavelength range of $1.1 < \lambda < 2.4\,\mu$m. The instrument combined coherently the light of three telescope beams instead of the four of GRAVITY and MATISSE. This instrument was decommissioned in 2018, but we have used published data of RSGs obtained with AMBER in Chapter 3.

1.5   This thesis

This thesis can be organised in three main topics: studying the temperatures of RSGs and their metallicity dependence, modelling the extended atmospheric layers using already available spectro-interferometric data, and further modelling using newly obtained spectro-interferometric data. The main goals for each of the topics are discussed in this section.

- **Temperature dependence of RSGs on metallicity:** Despite numerous efforts, understanding the properties of massive stars and their evolution has been a challenge due to their extended atmospheres, demanding NLTE (non-local thermodynamic equilibrium) models, unstable structures, stellar winds, and atmospheric molecular compositions. One of the hot topics for cool massive stars (a.k.a. RSGs) is how to correctly determinate their effective temperature, particularly since there has been disagreement in the recent literature on this topic (e.g., Levesque et al., 2005, 2006; Davies et al., 2013b), where some authors have argued that RSGs are cooler than stellar theory allows (see Section 1.3.2).

The correct determination of the temperatures of RSGs is crucial to obtain RSGs luminosities, since the bolometric correction (BC) can vary up to 2 mag in the optical (Levesque et al., 2005) at that typical temperature range ($T_{\mathrm{eff}} \sim 3400 - 4500\,\mathrm{K}$). To obtain effective temperatures of RSGs, spectroscopic analysis has been generally performed by fitting the TiO lines (Levesque et al., 2005, 2006) since for cold stars it is the most prominent feature in their spectra. However, it appears that this method underestimates the temperature of those stars (Davies et al., 2013b), appearing cooler than expected, and it is not in accordance with the theoretical predictions.

In Chapter 2 of this thesis, we explore a T_{eff} determination method independent of the TiO bands, by fitting the whole SED except the regions dominated by molecular absorption (see Davies et al. 2013b). We analyse three samples of RSGs from the Local Group neighbouring galaxies Wold-Lundmark-Mellote (WLM), SMC and LMC. This allows us to explore the metallicity effects in the determination of the stellar parameters, as all galaxies have a lower metallicity than the Milky Way. The T_{eff} and extinctions (A_{V}) have been obtained, as well as their bolometric luminosities (L_{bol}) using synthetic and observed photometry available at the SIMBAD database (Wenger et al., 2000). We also perform a population synthesis using the theoretical evolutionary tracks by Ekström et al. 2012; Georgy et al. 2013; Groh et al. 2019, and compare the observations with the predictions from the simulations to assess the statistical significance of the discrepancy.

- **Modelling the atmospheric extension of RSGs:** So far, stellar atmosphere models have been constrained mostly by comparison to stellar spectra. The spectral computation shows the flux integrated over the stellar disk and misses the spatially resolved information. Therefore, if we want a detailed way to study spatially extended stellar atmospheres, we need to use interferometric data. Interferometry is a very powerful tool to study the topography of extended atmospheres in detail, and it has been used widely both for RSGs (e.g. Arroyo-Torres et al., 2013; Wittkowski et al., 2012; Climent et al., 2020; Chiavassa et al., 2022) and Miras (e.g. Wittkowski et al., 2018; Kravchenko et al., 2020). As a consequence, interferometry represents a stronger test for models.

Recently, Davies and Plez (2021) developed a semi-empirical model based on a hydrostatic MARCS model atmosphere (Gustafsson et al., 2008) and the

addition of a wind profile. Using this model to extend the stellar atmosphere, Davies and Plez (2021) found that they could reproduce most of the spectral features obtained by addition of a MOLsphere, without the need of dust.

In Chapter 3, we compare the model by Davies and Plez (2021) to published Very Large Telescope Interferometer (VLTI) AMBER data by Arroyo-Torres et al. (2015). Interferometry allows to explore the extension of the atmospheres of RSGs thanks to its unprecedented high angular spatial resolution. We find that our model can reproduce the atmospheric extension for the first time up to $\sim 8R_\star$, where $R_\star$ is the stellar radius at the photosphere, defined as the layer where the Rosseland optical depth is $\tau_{\mathrm{Ross}} = 2/3$. The squared visibility amplitudes ($|V|^2$) could be reproduced as well for the first time in the K band. These important results can open a window to explore mass-loss events of cool massive stars, since they provide atmospheric extensions and there is no need to rely anymore on the external dust component.

- **Further modelling with new data:** In Chapter 4, we use new data from the VLTI/GRAVITY and MATISSE instruments of five new targets to compare with our models. The data has been obtained by submitting successful observing proposals where the author has been the PI and co-I. The observations have been prepared, calibrated, reduced and analysed by the author. We will also study the formation of SiO in the atmospheres of RSGs.

  We are using the MATISSE wavelength range in new observed RSGs that includes the SiO feature at $4.0\,\mu$m. This is one of the first studies of RSGs using the MATISSE instrument after Chiavassa et al. (2022). Moreover, Chiavassa et al. (2022) used low spectral resolution, while we obtain the data with medium spectral resolution. Complementing with GRAVITY observations in the K band, we have obtained some of the most complete spectro-interferometric data up to date of RSGs, covering the wavelength range of $1.8 < \lambda < 13\,\mu$m.

Finally, Chapter 5 will summarise the different findings of this thesis and discuss future work, such as developing a new mass-loss prescription by using our modelling approach and both spectra and interferometric data.

Chapter 2

Red supergiants in low metallicity environments

2.1 Abstract

The temperatures of red supergiants (RSGs) are expected to depend on metallicity (Z) in such a way that lower-Z RSGs are warmer. In this chapter, we investigate the Z-dependence of the Hayashi limit by analysing RSGs in the low-Z galaxy Wolf-Lundmark-Mellote (WLM), and compare with the RSGs in the higher-Z environments of the Small Magellanic Cloud (SMC) and Large Magellanic Cloud (LMC). We determine the effective temperature (T_{eff}) of each star by fitting their spectral energy distributions, as observed by VLT+SHOOTER, with MARCS model atmospheres. We find average temperatures of $T_{\mathrm{eff_{WLM}}} = 4400 \pm 202$ K, $T_{\mathrm{eff_{SMC}}} = 4130 \pm 103$ K, and $T_{\mathrm{eff_{LMC}}} = 4140 \pm 148$ K. From population synthesis analysis, we find that although the Geneva evolutionary models reproduce this trend qualitatively, the RSGs in these models are systematically too cool. We speculate that our results can be explained by the inapplicability of the standard solar mixing length to RSGs.

2.2   Observations and Data reduction

2.2.1   New data

We have observed several RSGs in WLM, selecting our targets from Levesque and
Massey (2012). We chose the 9 brightest objects in the near-IR, which represents
all RSGs in this galaxy with luminosities $\log(L_{\rm bol}/L_\odot) > 4.4$ (see Fig. 2.3). Our
targets are listed in Table 2.3. We observed each star with VLT+XSHOOTER
(D'Odorico et al., 2006) in order to obtain contemporaneous spectrophotometry
from the optical to the near-IR, under the ESO program number (093.D-0021(A),
PI: B Davies). All stars were observed with the $5''$ slit to minimise slit losses, in
an ABBA nodding pattern. Slit positions were defined specifically to avoid any
nearby stars clashing in the dispersion direction. The total integration times were
the same for each star; 2248sec, 2760sec, and 3040sec in the UVB, VIS, and NIR
arms respectively. The NIR integrations were broken up into discrete integration
times of 190sec to avoid saturation in the airglow emission lines. In addition to
the science targets, telluric standard stars of spectral type B were observed within
1.5hrs of any science exposure. Data were reduced following the same procedure
described in Davies et al. (2013b).

When observing the stars from a very distant galaxy such as WLM, we cannot
rule out the possibility that the RSGs observed are part of multiple systems,
and other stars can contribute to the flux measured. However, at the resolution
of ground-based survey imaging, we see no evidence of source confusion from
abnormal colors or point spread functions. In addition, we see no evidence of
hybrid spectral features (e.g. Balmer lines) in the blue, which would be indicative
of an unresolved multiple system. Even with other targets being in the slit, RSGs
are much brighter than anything else so the likelihood of significant contamination
is small.

While performing the analysis, we found that the WLM star number 7 (WLM
07) in Table 2.3 has a radial velocity $v = 30\,\mathrm{km/s}$, while all the others are $v \sim$
$120\,\mathrm{km/s}$. Checking their parallaxes at SIMBAD (Wenger et al., 2000), WLM 07
has 1.4307 ± 0.6966 mas (Gaia Collaboration et al., 2018), while the other targets
have parallaxes consistent with 0 mas (Gaia Collaboration et al., 2018). Both
velocities and parallaxes of WLM 07 are not coincident with the rest of the WLM
targets in within the errors. Furthermore, this star has a spectral type (M3) which

Galaxy	Sub-sample $\overline{T}_{\text{eff}}$ (K)	Full sample $\overline{T}_{\text{eff}}$ (K)
LMC	3800 ± 50	3810 ± 100
SMC	3940 ± 30	3970 ± 70

TABLE 2.1: Results of the statistical significance test. The left column indicates the galaxy studied, the middle column shows the average T_{eff} retrieved given our sub-sample from Tabernero et al. (2018), the right column shows the average T_{eff} for the full sample in Tabernero et al. (2018). The errors from the middle column are taken from the standard deviation of the histogram of the simulations (see Appendix A).

is much later than the others (K0-3, see Table 2.3). We have assumed that the target is a foreground star and not part of WLM. For these reasons, WLM 07 has been excluded from further analysis.

2.2.2   Archival data

For the LMC and SMC, we used the previous data from the VLT+XSHOOTER observations, under the ESO programme number 088.B-0014(A) (PI B. Davies). The observations, selection criteria and reduction steps are described in Davies et al. (2013b, 2015). The stars from LMC and SMC were selected from Levesque et al. (2006) to sample the full distribution of spectral types in each galaxy (as explained in Davies et al. 2013b). As a further test that our sub-sample of stars in each galaxy has a distribution of T_{eff} representative of the entire RSG population of that galaxy, we perform the following tests: we randomly select 10 RSGs from Tabernero et al. (2018) that have the same spectral type distribution as our sample stars. For each of these 10 stars, we randomly assign a T_{eff} based on that star T_{eff} measurement and associated error in Tabernero et al. (2018). Next, we obtain the average T_{eff} of these 10 randomly selected temperatures. We repeat this process 100 times for both LMC and SMC targets. Finally, we compare the results with the average T_{eff} of the whole sample in Tabernero et al. (2018). The error in the average temperatures is calculated with the mean error of the individual stars and the standard deviation. In Figure A.1 of Appendix A we show the results of the histogram with the results of the simulations compared with the average T_{eff} of the full sample.

Checking the results in Table 2.1, we see that the mean value for the sub-sample distribution is within the error limits of the average temperature of the whole RSGs sample in Tabernero et al. (2018). Both results are coincident within the

error limits. Therefore, we conclude that our two sub-samples of stars have T_{eff} distributions consistent with those of the entire population in each galaxy.

2.3   Determination of effective temperatures

We begin with a grid of model atmospheres generated with the MARCS code (Gustafsson et al., 2008). The 1D code assumes local thermodynamic equilibrium (LTE), hydrostatic equilibrium, and spherical symmetry. We fixed the metallicities to be $[Z]_{\text{WLM}} = -1.0$ (Urbaneja et al., 2008), $[Z]_{\text{LMC}} = -0.35$, and $[Z]_{\text{SMC}} = -0.55$ (Davies et al., 2015). As for the metallicity adopted in WLM, in Urbaneja et al. (2008) it is stated that previous photometric studies show WLM as having a young population in the disk, and an old metal-poor halo. By observing the red giant branch color, McConnachie et al. (2005) found a metallicity of $[Z] = -1.45$ with respect to solar. This result however did not take into account the contribution of the younger population. When inspecting rich-metal line spectra of A supergiants, Urbaneja et al. (2008) found an average metallicity of $[Z] = -0.87 \pm 0.06$. The $[Z]_{\text{WLM}} = -1.0$ adopted in this work is consistent with that found from analysis of WLM blue supergiants by Urbaneja et al. (2008) once the differences in the Solar abundances used in that study and ours are taken into account (see Appendix of Davies et al. 2017).

We assumed the fiducial values for the microturbulence of $\xi = 3\,\text{kms}^{-1}$ (see Davies et al. 2015). Surface gravities used are log g $= -0.2$ for the Magellanic Clouds (MCs), as in Davies et al. (2015), while for WLM log g $= 0$. The log g of the WLM stars was found iteratively, by comparing their luminosities and temperatures determined from our analysis with the evolutionary tracks of Georgy et al. (2013). We have found gravities ranging from -0.2 to $+0.4$, with the majority around ~ 0.0. The robustness of our results to these fiducial values for gravity, metallicity and microturbulence are discussed in Section 2.4.1. The model grid is computed between $3400\,\text{K} < T_{\text{eff}} < 5000\,\text{K}$ in steps of 100 K, which we then interpolate into a finer grid of 20 K steps.

In addition to fitting for the best T_{eff}, we also allow the extinction A_{V} to vary, since this parameter can make the star appear cooler and create a large degree of degeneracy with T_{eff}. For the MCs we use the extinction law of Gordon et al. (2003), which is specifically tuned to the interstellar medium in the direction of

λ_{min} (nm)	λ_{max} (nm)
821.6	831.9
871.7	880.0
1036	1080
1212	1278
1610	1614
1649	1659
1716	1723
2120	2250

TABLE 2.2: Regions used of the SED for the analysis.

these galaxies. For WLM we use instead the law derived by Cardelli et al. (1989), and assume a $R_V = 3.1$ as of the Milky Way. The robustness of this assumption is explored in Section 2.4.1. For the baseline (i.e. Galactic) extinction towards WLM, Schlafly et al. (2014) shows that it is very low, and consistent with zero ($0 \leq E(B-V) \leq 0.1$). Therefore, it will not influence our results. The grid of extinction parameters used is $0 < A_V < 2$ with a step of 0.01.

For the analysis, we fit the SED windows unaffected by line and molecular absorption as seen in Table 2.2, which are the same used in Davies et al. (2013b). We avoid the BVR spectral region, the molecular absorption bands of TiO, VO, CO (at $\sim 1.5\,\mu$m and $> 2.3\,\mu$m), and the CN band at $1.1\,\mu$ m. While Davies et al. (2013b) performed a pixel-by-pixel matching of these spectral regions, we fit the mean flux of each SED window. The reason is that the SNR in the near-IR region of the WLM spectra are not high enough to do pixel-by-pixel analysis.

At each point in the model grid (i.e. for each value of T_{eff} and A_V) we adjusted the SED to the same data flux by minimising the $\sum(\log(SED_{\text{model}}) - \log(SED_{\text{data}}))$ at the line-free continuum, where $\log(SED)$ represents the base-10 logarithm of the SED flux regions, in order to compare both fluxes.. We then performed a 2-parameter fit by means of a χ^2 minimisation, assuming Gaussian correlation as shown in eq. 2.1:

$$\chi_i^2 = \sum_{i=1}^{n} \frac{(SED_{\text{data}} - SED_{\text{model}})_i^2}{\sigma_i^2},\qquad(2.1)$$

where n is the number of spectral regions in Table 2.2, SED_{data} represents the mean flux of the data for each one of the regions, SED_{model} the mean flux of the model, and σ_i^2 the standard deviation of the data in each SED region.

The result of the analysis is a 2D-array of χ^2, one value for each A_V and T_{eff}. The best fit parameters correspond to those at the minimum value of the χ^2 2D-array.

For the errors on T_{eff} and A_V, we first determine the 68% dispersion contours of the χ^2 fit, that for two degrees of freedom like the present case (T_{eff} and A_V), corresponds to all the grid models with values $\chi^2 < \chi^2_{min} + 2.3$ (Avni, 1976), where χ^2_{min} is the best-fitted model. The errors on each parameter are then defined as being the minimum values within this range.

The L_{bol} were calculated for WLM targets using synthetic photometry and available photometry at the SIMBAD database (Wenger et al., 2000), with 2MASS (Pickles and Depagne, 2010), Gaia DR2 (Gaia Collaboration et al., 2018), PAN-STARSS (Chambers et al., 2016), VISTA (McMahon et al., 2013), SkyMapper (Wolf et al., 2018) and Spitzer/IRAC (Boyer et al., 2015) photometry. The magnitudes for the different filters were converted to flux, dereddened using the previously determined extinction A_V, and integrated over the wavelength range for all the photometric filters available (from $0.36\,\mu$m to $7.5\,\mu$m). We transformed to bolometric luminosities using the most recent distance determination $d_{\mathrm{WLM}} = 995 \pm 46$ kpc (Urbaneja et al., 2008). Dorda et al. (2016) showed that SMC RSGs display a high degree of spectral variability, finding evidence that variability increases with decreasing metallicity. Furthermore, Beasor et al. (2021b) studied the effect of the variability between the minimum and maximum states of the RSGs in the stellar cluster Westerlund 1. Even when the most extreme assumptions were made, the resulting impact on the L_{bol} was at most ± 0.2 dex. Therefore, any systematic uncertainty due to spectral variability in the stars in this work must be less than this.

To determine the error on L_{bol}, we propagated the errors through those on the individual flux measurements, the error on A_V, as well as the distance of the galaxy. Of these, the dominant source of uncertainty is the A_V.

2.4   Results

The best T_{eff}, A_V and $\log(L_{\mathrm{bol}}/L_\odot)$ obtained after the analysis, for each object in WLM is listed in Table 2.3 (with the errors from the 68% $\Delta\chi^2$ isocontours), as well as their stellar coordinates, apparent magnitudes, spectral types from Levesque
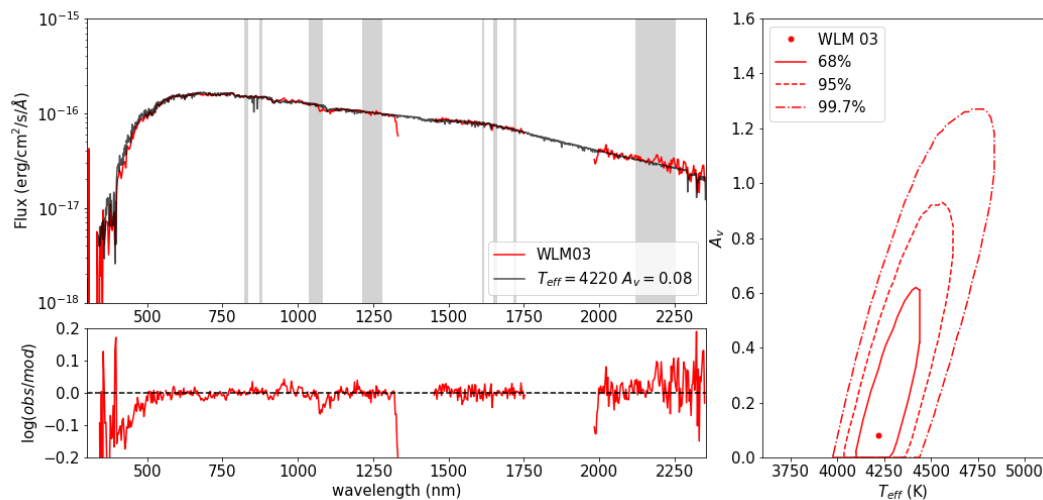
FIGURE 2.1: Three panels showing the results of the analysis. *Upper left:* Shows the smoothed data (red) and best fitted MARCS model (black), while the SED regions for the analysis are shown in gray. *Lower left:* The residuals of the fit. *Right:* shows the 68%, 95% and 99.7% confidence limits for the best fitted T_{eff} and A_{V}.

and Massey (2012), and identification names as in the SIMBAD database (Wenger et al., 2000). Figure 2.1 shows the results of the analysis for one case, where we see the best fit MARCS model (upper left panel) in black with respect to the data in red, the residuals of the fit in the lower left panel. The right panel of Figure 2.1 shows the best fitted parameters along with the ellipse dispersion contours for the 68% confidence limit, 95% and 99.7%. The best fits for the rest of the targets can be seen in Appendix B.

In Appendix B, we see that for WLM 01, 05 and 09 there is a continuum shift for the long-wavelength edge in the observations. This is because in the last order of the NIR arm there was a variable thermal background which affected the flux calibration. To investigate the impact of this effect, we repeated the analysis shifting the fitted region at this order for these particular cases. The results did not change for the first 2 cases, and changed by -20 K in WLM 09. This does not increase the errors for these stars. Moreover, WLM 01 has an extinction close to zero of $A_{\text{v}} = 0.00 \pm 1.02$, but one of the biggest error budgets of all WLM stars.

Table 2.4 shows the calculated values with the SED method for the SMC and LMC stars, with the errors in T_{eff} and A_{V} from the 68% $\Delta\chi^2$ isocontours. We have compared the stars with the previous results from Davies et al. (2013b, 2015); Tabernero et al. (2018) in Figure 2.2. The results are consistent between $1 - 2\sigma$

Star	ID	RA	DEC	m_R	T_{eff} (K)	A_V	$\log(L_{bol}/L_\odot)$	SpT
WLM 01	LGGS J000153.17-152813.4	00 01 53.181	-15 28 13.92	18.51	4580^{+420}_{-180}	$0.00^{+1.02}$	$4.47^{+0.08}_{-0.12}$	K0-1I
WLM 02	LGGS J000156.77-152839.6	00 01 56.785	-15 28 40.18	16.62	4660^{+340}_{-440}	$0.95^{+0.54}_{-0.95}$	$5.52^{+0.07}_{-0.06}$	K2-3I
WLM 03	LGGS J000156.87-153122.3	00 01 56.887	-15 31 22.84	17.91	4220^{+220}_{-120}	$0.08^{+0.54}_{-0.08}$	$4.80^{+0.11}_{-0.05}$	K0-1I
WLM 04	LGGS J000157.01-152954.0	00 01 57.023	-15 29 54.59	17.85	4560^{+440}_{-360}	$0.65^{+0.84}_{-0.65}$	$4.89^{+0.09}_{-0.07}$	K0-1I
WLM 05	LGGS J000157.55-152915.8	00 01 57.545	-15 29 16.05	18.41	4160^{+780}_{-140}	$0.11^{+1.38}_{-0.11}$	$4.66^{+0.13}_{-0.06}$	K0-1I
WLM 07	LGGS J000158.14-152332.2	00 01 58.146	-15 23 32.58	18.62	4460^{+540}_{-140}	$0.00^{+1.15}_{-0.01}$	$4.48^{+0.09}_{-0.04}$	M3I
WLM 08	LGGS J000158.74-152245.5	00 01 58.746	-15 22 46.03	17.56	4420^{+560}_{-220}	$0.40^{+1.04}_{-0.40}$	$4.98^{+0.07}_{-0.06}$	K0-1I
WLM 09	LGGS J000200.81-153115.7	00 01 59.610	-15 30 59.90	18.07	4340^{+160}_{-160}	$0.34^{+0.41}_{-0.34}$	$4.80^{+0.08}_{-0.07}$	K2-3I
WLM 10	LGGS J000200.81-153115.7	00 02 00.810	-15 31 15.70	17.78	4380^{+200}_{-220}	$0.60^{+0.51}_{-0.57}$	$4.84^{+0.10}_{-0.06}$	K0-1I

TABLE 2.3: Table shows the ID name, RA, DEC, m_R (in magnitudes), spectral type as indicated at the SIMBAD database, and the best T_{eff}, A_V and $\log(L_{bol}/L_\odot)$ obtained for each studied RSG at the WLM galaxy, within their 68% confidence limits. WLM 07 is suspected to be a foreground star.

Star	T_{eff} (K)	A_{V}
SMC 011709	4100^{+120}_{-80}	$0.49^{+0.35}_{-0.3}$
SMC 013740	4040^{+100}_{-80}	$0.81^{+0.32}_{-0.32}$
SMC 020133	4160^{+120}_{-100}	$1.27^{+0.37}_{-0.39}$
SMC 021362	3940^{+80}_{-100}	$0.37^{+0.33}_{-0.35}$
SMC 030616	4140^{+100}_{-120}	$0.73^{+0.35}_{-0.39}$
SMC 034158	4180^{+80}_{-100}	$0.55^{+0.32}_{-0.37}$
SMC 035445	4120^{+100}_{-80}	$0.46^{+0.29}_{-0.28}$
SMC 049478	4180^{+100}_{-100}	$0.75^{+0.34}_{-0.37}$
SMC 050840	4000^{+100}_{-100}	$0.55^{+0.33}_{-0.36}$
SMC 057386	4160^{+160}_{-120}	$0.39^{+0.44}_{-0.38}$
LMC 064048	3880^{+140}_{-120}	$0.52^{+0.61}_{-0.52}$
LMC 067982	4140^{+140}_{-140}	$1.52^{+0.47}_{-0.60}$
LMC 116895	4140^{+160}_{-140}	$1.10^{+0.65}_{-0.56}$
LMC 131735	4280^{+120}_{-120}	$0.81^{+0.50}_{-0.44}$
LMC 136042	4100^{+100}_{-100}	$1.99^{+0.01}_{-0.30}$
LMC 137818	4040^{+160}_{-140}	$0.85^{+0.53}_{-0.55}$
LMC 142202	4160^{+100}_{-160}	$1.79^{+0.20}_{-0.66}$
LMC 143877	4300^{+100}_{-120}	$1.22^{+0.47}_{-0.45}$
LMC 158317	4140^{+120}_{-120}	$1.55^{+0.44}_{-0.54}$

TABLE 2.4: Best T_{eff} and A_{V} obtained for each studied RSG at the SMC and LMC galaxies, within their 68% confidence limits. The stars names are based on the catalogue available by Davies et al. (2018b).

for the first two panels, the discrepancy with Tabernero et al. (2018) is discussed in Section 2.4.2.

There is one particular case in LMC that needs to be taken with care. Checking Figure B.24, we see that for LMC 136042 the observations (upper left panel, in blue) tend to upper the continuum in the spectral region of <500 nm, meaning that their flux contribution at the green-blue region of the spectra is higher than expected. This indicates that there is a blue star next to this target (González-Fernández et al., 2015). We excluded this target for the rest of the analysis.

The stars are placed in the Hertzprung-Russel diagram (HRD) in Figure 2.3, based on their L_{bol} and T_{eff}. We have also plotted for comparison the $9-20\,M_{\odot}$ rotating evolutionary tracks for RSGs taken from Georgy et al. (2013), in black solid-line showing the tracks corresponding to a $Z = 0.002$, comparable to the studied
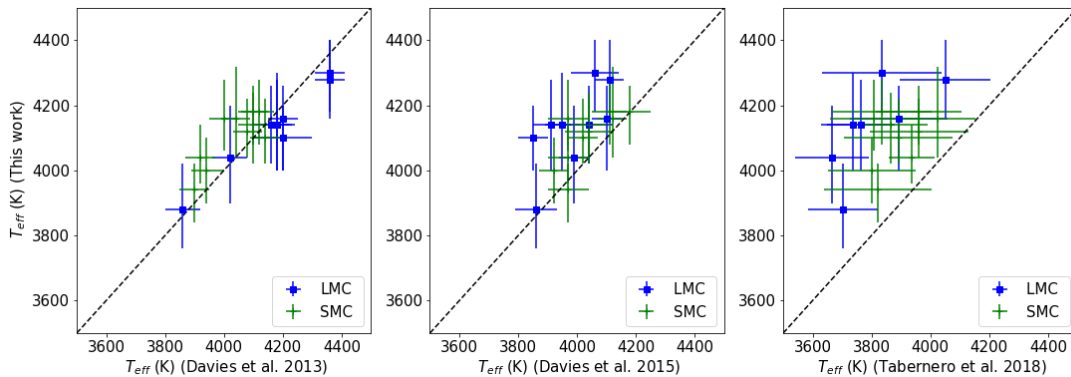
FIGURE 2.2: Comparison between the results from this work (y-axis) and the previous results found by Davies et al. (2013b) (*left panel*), Davies et al. (2015) (*center panel*) and Tabernero et al. (2018) (*right panel*). The SMC targets are represented in green, while the LMC in blue squares. The black-dashed line shows the 1:1 ratio.

galaxies. The average values for the three galaxies (excluding WLM 07 and LMC 136042, for the reasons already mentioned), are:

$$\text{WLM: } T_{\text{eff}} = 4400 \pm 202 \text{ K},$$

$$\text{SMC: } T_{\text{eff}} = 4130 \pm 103 \text{ K},$$

$$\text{LMC: } T_{\text{eff}} = 4140 \pm 148 \text{ K},$$

where the errors correspond to the quadratic sum of the formal errors from the model fitting and the systematic errors arising from our assumptions when fitting the data (see Section 2.4.1).

With the results above we see that, as theory predicts (e. g. Maeder and Meynet 2001) there is a dependence with average T_{eff} of RSGs on Z for WLM and the MCs. Indeed the lowest-Z galaxy shows an average temperature ~ 250 K higher than the MCs. In the case of the MCs, we are not able to resolve a temperature difference between these two galaxies. This result agrees with previous work from Davies et al. (2015), which claimed that there is no measurable dependence of T_{eff} on Z between the metallicities of LMC and SMC. In this current work we extend the metallicity baseline down to $[Z] = -1$, after which a trend on T_{eff} with Z becomes clear (see Figure 2.6).
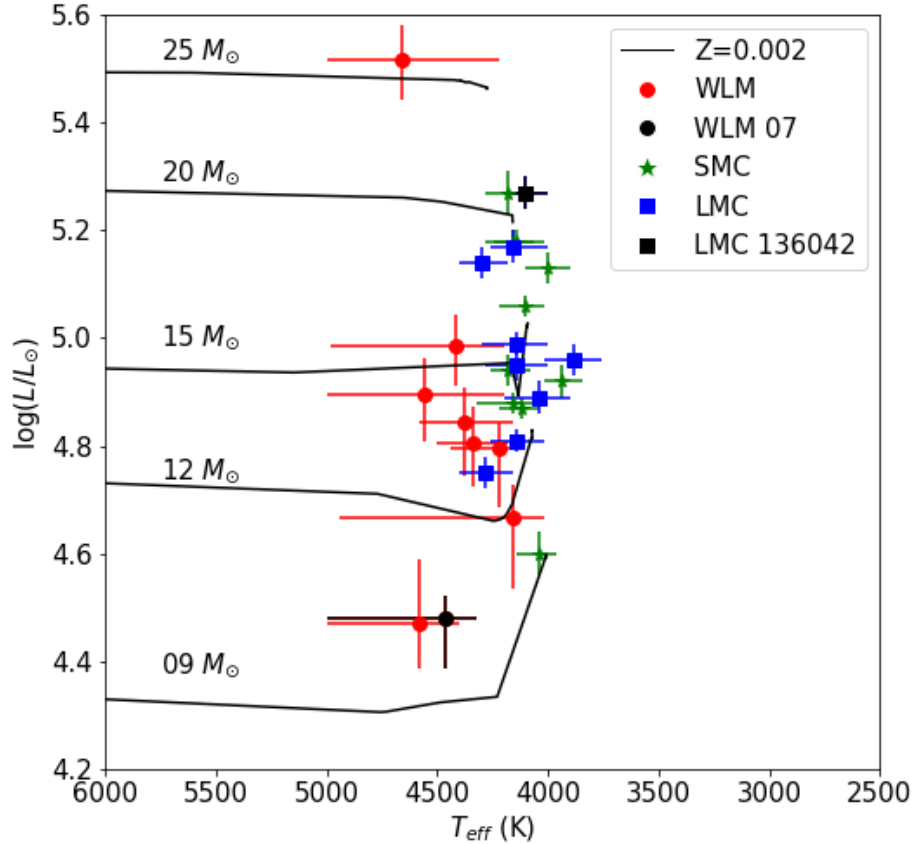
FIGURE 2.3: HRD showing the RSGs of WLM (red), LMC (blue), SMC (green), with the evolutionary tracks from Georgy et al. (2013), with a $Z = 0.002$, and rotation $v/v_c = 0.4$ comparable to the galaxies studied. The black dots correspond to the problematic targets. The luminosities for the MCs are taken from Davies et al. (2018b).

2.4.1   Robustness of the analysis

As described in Section 2.3, we made several assumptions in our fitting methodology. In this section, we now investigate the sensitivity of our results to these assumptions.

2.4.1.1   Microturbulence

To investigate the effect of varying our choice of ξ for the models employed, we repeated the analysis for each target with $\xi = 2$ and 4 km/s, since Davies et al. (2015) found a range of ξ between $2 - 4$ km/s for all MCs stars. The median T_{eff}

does not change for WLM when assuming these ξ values, while for the MCs it changes in both by -10 K with $\xi = 2$, and $+20$ K for $\xi = 4$. We see that the effect of varying ξ is a factor of 10 smaller than the fitting errors. Therefore, a systematically different ξ in WLM cannot explain the T_{eff} differences between this galaxy and the MCs.

In short, the choice of ξ makes little to no difference to our results. The reason is that ξ will affect the strong absorption lines of the spectra, but in this work we are studying the line-free continuum.

2.4.1.2   Surface gravity

We also perform the analysis with log g $= -0.5$ and log g $= +0.5$ based on the gravity range found in Davies et al. (2015). We find that for log g $= -0.5$ in WLM the average temperature varies by -100 K while for the MCs it varies by -40 K for both. With log g $= +0.5$ the variation is $+80$ K for WLM, $+30$ K for SMC, and $+40$ K for LMC. As a consequence, we see that the choice of surface gravity seems to make an impact on the final results in WLM, while for the MCs the variation is again smaller. As commented in Section 2.3, we expect the range on surface gravities to be $-0.2 < $ log g $ < +0.4$, with the majority around 0. This is comparable with the results from Davies et al. (2015).

To sum up, there is a stronger degeneracy when studying the effect of log g. This offset seems to be of ± 80 K, but cannot explain why the T_{eff} in WLM is ~ 250 K higher than the MCs.

2.4.1.3   Extinction law

To check the robustness of the extinction law for WLM, we have performed the analysis using various values of R_{V} from 2 to 6. The results changed by less than 30 K for $R_{\text{V}} = 2$, 4 and 5, while for a extreme assumption such as $R_{\text{V}} = 6$ the difference was of only $+50$ K. Since WLM is a metal poor environment, we also studied the effect of using a SMC-like extinction law, and found a difference on the average temperature of -20 K, all between the error limits. The best fit for A_{V} changes a maximum of $+0.09$ for the extreme assumption of $R_{\text{V}} = 6$, and it is within the error limits for A_{V}.

In conclusion, the choice of R_v and extinction law makes barely any difference when determining the $T_{\rm eff}$.

2.4.1.4   SED continuum regions

The last assumption that needs to be checked is the choice of the SED continuum regions. We have recalculated our results with slightly different SED regions (e. g. including a continuum region at ~ 400 nm, or varying the *JHK* band regions in Table 2.2 by ~ 50 nm). We find that the choice of continuum windows can shift the median $T_{\rm eff}$ in each galaxy by ± 60 K. We interpret this error to represent the absolute level of accuracy on our results. In other words, a median $T_{\rm eff}$ difference between two galaxies within 60 K would be consistent with zero.

Lastly, the choice of the SED continuum regions give a systematics of ~ 60 K, this is smaller than the limitations obtained by the 68% dispersion contours, and can be related with the accuracy of the method.

2.4.2   Comparison with previous studies

Davies et al. (2013b) used two different methods to calculate the $T_{\rm eff}$ of the same targets: the first one has been conventionally used to analyse M-K type stars, and is based on fitting the TiO spectral bands (between 500 and 800 nm). The second method is the same SED continuum fit as used for this work, but with a $\xi = 2$ km/s[1]. In the left panel of Figure 2.2 we compare our results to those of Davies et al. (2013b). We notice that the star-to-star differences with Davies et al. (2013b) are always in between 1σ for both MCs, and there is no systematic offset. The very slight discrepancies between the results from this work (y-axis) and Davies et al. (2013b) (x-axis) can be justified by the change in log g and ξ, as seen in Sect 2.4.1.

In Davies et al. (2015) the method consists of comparing the strengths of different spectral lines on the J-band with non-LTE model grids. We have used the same log g and ξ as in Davies et al. (2015). In the center panel of Figure 2.2, we can see that the results are consistent between 2σ, and obtain a median offset of ~ 60

---

[1]As the Davies et al. (2013b) study pre-dated the detailed spectral fitting in Davies et al. (2015) in which the microturbulent velocities were measured.

K, which is within the level of precision obtained by the choice of SED regions in Section 2.4.1. Despite the two completely different methodologies employed, the agreement is excellent.

The work of Tabernero et al. (2018) differs the most from this work (right panel in Figure 2.2). We have calculated a median offset of ~ 150 K between both results, ours being warmer. In Tabernero et al. (2018), temperatures are estimated by fitting spectral lines in the I-band with predictions from MARCS model atmospheres and LTE line formation.

The differences between our results and those of Tabernero et al. (2018) are twofold. Firstly, these LTE models do not include the non-LTE correction employed in Davies et al. (2015). This can account for ~ 50 K (see Bergemann et al. 2013b), assuming that the corrections in the I-band are similar to those in the J-band.

Secondly, the region studied in Tabernero et al. (2018) of the I-band overlaps with a TiO absorption band. Davies et al. (2013b) showed that the MARCS models cannot simultaneously reproduce the TiO bands and the continuum (see Figure set 1 in Levesque et al. 2005 and Figure set 2 in Levesque et al. 2006). This makes continuum placement in the I-band gradually more problematic at spectral types M0 and later, as the contamination by TiO grows. Therefore, we would expect to see a trend of increasing disparity between the T_{eff} of Tabernero et al. (2018) and those of our study with increasing spectral type. Indeed, this is what we see in Figure 2.4, a trend for the increasing difference between the T_{eff} of Tabernero et al. (2018) and those of our work (ΔT_{eff}) as we go to later spectral types, for both LMC and SMC. Therefore, we conclude that the systematic offset in Figure 2.2 can at least be partially explained by this trend.
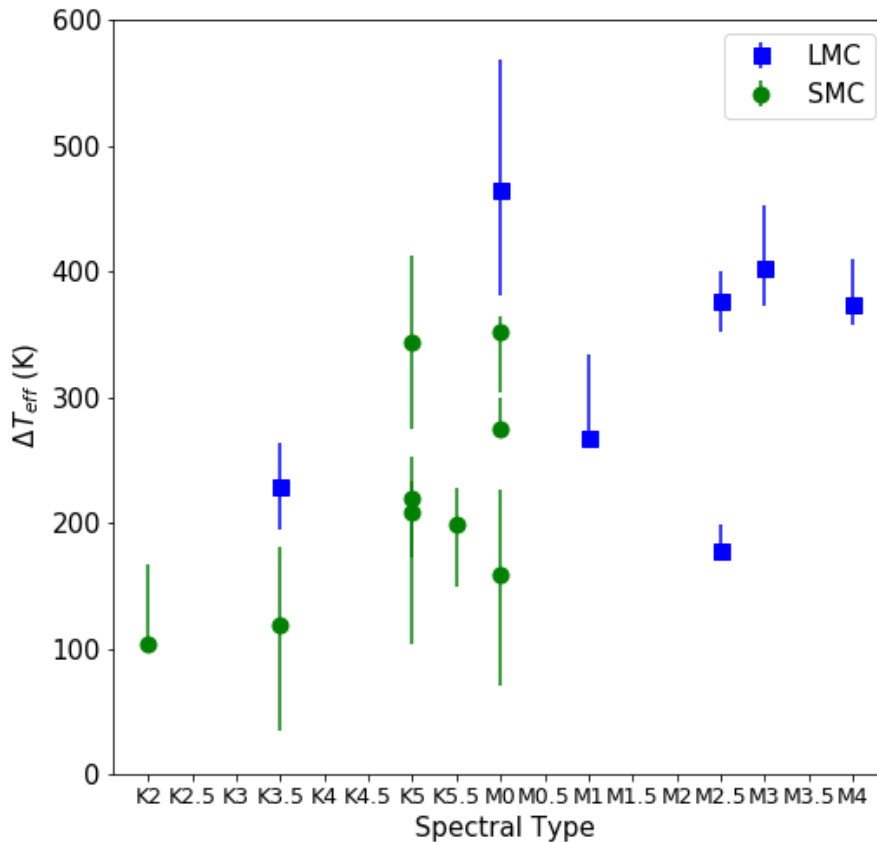
FIGURE 2.4: Panel showing the difference between the T_{eff} results from this work and Tabernero et al. (2018), with respect to the spectral type of each RSG studied in the LMC (green dots) and the SMC (blue squares), as in the SIMBAD database.

2.5   Discussion

In Section 2.4, we have found an average T_{eff} of RSGs in WLM warmer than for the higher Z environments of the MCs. As seen in Section 2.4.1, these differences cannot be explained by systematics in the fitting method. In this section, we investigate how our results compare to the expectations from stellar evolution models.

To better understand how our results compare to model predictions, we performed a population synthesis analysis. We generated a number of simulated stars ($\sim 10^5$) with masses of $5 - 100\,M_\odot$ according to a Salpeter initial mass function. Then we assigned random ages, and used the evolutionary tracks of Ekström et al. (2012);
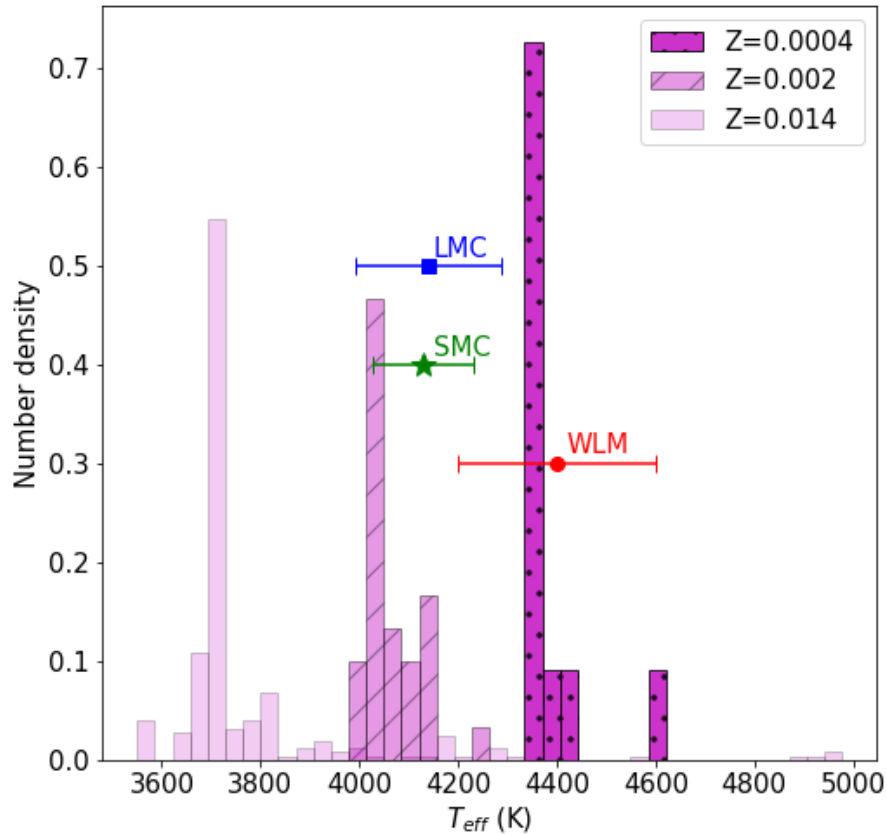
FIGURE 2.5: Histograms showing the number density of simulated stars, in solid magenta bins for Z=0.014, dashed bins for Z=0.002 and spotted bins for Z=0.0004. The median temperature and error bars calculated with the observations for the three galaxies is also shown in green (SMC), blue (LMC) and red (WLM). The simulations shown are obtained for non-rotating stars.

Georgy et al. (2013); Groh et al. (2019) to interpolate their luminosities and T_{eff} at that age. We disregarded stars that are not in the RSG phase or are older than their expected lifetime. We have then selected the stars with $4.4 < \log(L_{\mathrm{bol}}/L_{\odot}) < 5.6$ (following Davies and Beasor 2020) and $3000 < T_{\mathrm{eff}} < 5000$ K, corresponding to a RSG phase and the stars in our sample. We determine the T_{eff} distribution of the stars in the RSG phase. Figure 2.5 shows the histograms of the T_{eff} from the RSGs after the population synthesis, for the case of non-rotating simulated stars with Z=0.014, 0.002 and 0.0004. As expected, we see that for higher metallicities there is a trend to lower temperatures. This trend does not change if we use a $\log(L_{\mathrm{bol}}/L_{\odot}) = 4.5$ or 5 cut instead.

A clearer visualisation of this Z dependence with T_{eff} can be seen in Figure 2.6: the

median T_{eff} of the simulated stars is shown with respect to their $[Z]$, in magenta for non-rotating and in yellow for rotating simulated stars. The shaded regions show the 68% confidence limits (analogous to a 1σ standard deviation). The median T_{eff} are also shown in Figure 2.6 for the observations of each galaxy. Comparing the model predictions with the data, we point out the following:

- For all three galaxies, the RSGs appear to be warmer than the model predictions.

- The results show a similar qualitative slope in comparison with the simulations, but the models seem to be too cool, especially for the non-rotating models. This systematic offset is $\Delta T_{\text{eff}_{\text{WLM}}} = 220\,\text{K}$, $\Delta T_{\text{eff}_{\text{SMC}}} = 140\,\text{K}$, and $\Delta T_{\text{eff}_{\text{LMC}}} = 250\,\text{K}$ for rotating models, while $\Delta T_{\text{eff}_{\text{WLM}}} = 300\,\text{K}$, $\Delta T_{\text{eff}_{\text{SMC}}} = 220\,\text{K}$, and $\Delta T_{\text{eff}_{\text{LMC}}} = 300\,\text{K}$ for non-rotating. The offset is also out of the error dispersion for the LMC. The significance of this offset is discussed below.

To determine the statistical significance of the offset of the observed T_{eff} with respect to the model predictions, we perform a Monte-Carlo (MC) test. Each MC trial is constructed as follows: firstly, for each galaxy, we randomly select N stars, where N is the number of stars observed in that galaxy (e.g. $N = 10$ in SMC). We note an individual star may be selected more than once per trial. Then, for each randomly selected star, we randomly assign a T_{eff} from that star's observed probability distribution (illustrated by e. g. the right panel in Figure 2.1). Finally, we determine the median T_{eff}, $\overline{T}_{\text{eff}}$, of the N stars. We then repeat this process 1000 times to determine the probability distribution on $\overline{T}_{\text{eff}}$ for each galaxy.

Using Figure 2.6, we interpolate the simulated T_{eff} and its uncertainty at the metallicity of the galaxy, and its corresponding error limits. Next, we calculate the probability that the model fits the data by integrating the product of the observed and simulated T_{eff} distributions. We repeat this process for every galaxy.

For rotating models, we find a probability that the model and data agree of $p_{\text{WLM}} = 0.07$, $p_{\text{SMC}} = 0.03$, and $p_{\text{LMC}} = 0.01$. The probability that all three galaxies are consistent with the rotating model predictions is $p_{\text{total}} = 10^{-5}$. For non-rotating models we find $p_{\text{WLM}} = 0.003$, $p_{\text{SMC}} = 0.003$, $p_{\text{LMC}} = 0.0004$, and $p_{\text{total}} = 10^{-7}$. We conclude that the systematic offset between observed and predicted T_{eff} in

all galaxies in this study cannot be explained by random scattering within the experimental errors.

A possible explanation to this mismatch between observations and simulations could be a breakdown in the assumptions used to simulate convection in RSGs. In 1D models, the mixing length theory (MLT) (Böhm-Vitense, 1958) is the analytic approximation used to describe the 3D phenomenon of convection. It assumes that a fluid parcel can travel a distance fixed by the so-called mixing length, l, before dispersing into the surrounding material. This mixing length is usually expressed in terms of the pressure scale height, $\alpha_{\mathrm{MLT}} = l/H_P$, where α_{MLT} is the mixing length parameter. This free parameter is usually calibrated using the standard solar model with a single depth-independent $\alpha_{\mathrm{MLT}}^{\odot}$. This solar calibrated value is used for stars of all masses, metallicities, and evolutionary phases. Indeed, the evolutionary tracks in this work by Ekström et al. (2012); Georgy et al. (2013); Groh et al. (2019) use $\alpha_{\mathrm{MLT}} = \alpha_{\mathrm{MLT}}^{\odot} = 1.6467$ for massive star models, arguing that α_{MLT} only changes to 1.6 for very high mass stars, $M = 150 M_{\odot}$ (Georgy et al., 2013). This variation was found by accounting for the differences in the massive stars equation of state.

However, 3D simulations of convection in low mass stars have shown that there is a strong α_{MLT} dependency on T_{eff} and log g (e.g. Trampedach et al. (2014), where for $T_{\mathrm{eff}} < 5000$ K a $\alpha_{\mathrm{MLT}} > 1.8$ is found). Work by Magic et al. (2015) also finds a difference of $\sim 20\%$ in the α_{MLT} depending on the mass of the star. Although these studies do not extend to the parameter ranges relevant for RSGs, they point out that the value of α_{MLT} is not independent of the mass.

Specifically studying RSGs, Chun et al. (2018) adopts the approach of tuning α_{MLT} to match the locations of RSGs in a range of metallicity environments. Regardless of which RSG temperature scales are used, they argue for a metallicity dependent α_{MLT}. Moreover, Dessart et al. (2013) studies the supernova type II-P (SN IIP) progenitors, varying the parameters (e.g. mixing length, overshoot, rotation, metallicity) in the stellar evolution code MESA STAR. They find that the RSG radii should be reduced in comparison with Levesque et al. (2005), implying that the T_{eff} of RSGs should be higher than the Levesque et al. (2005) temperature scale.

The previously described work, in combination with our results presented in this study, are part of a growing body of evidence that the assumption of a solar mixing
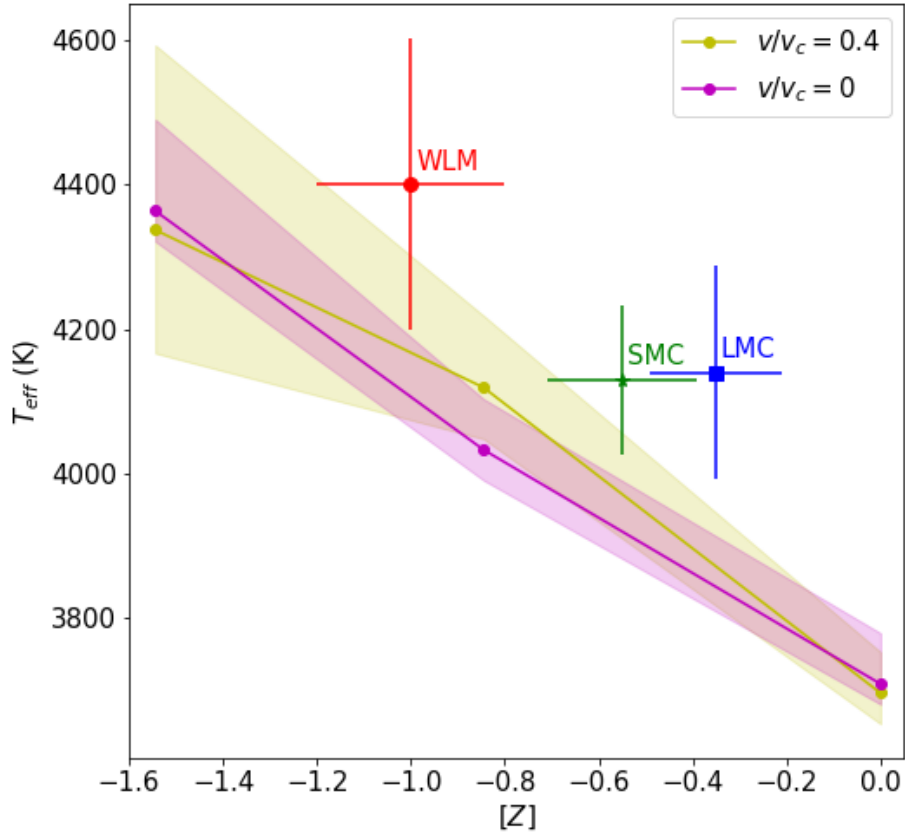
FIGURE 2.6: Plot showing the temperature trend with respect to the metallicity ([Z]), in yellow for rotating simulated stars, and magenta for non-rotating. The error limits in the trend are calculated using the 68% dispersion of the cumulative distribution for the skewed histograms. The median temperatures and error bars calculated with the observations for the three galaxies are also shown in green (SMC), blue (LMC) and red (WLM).

length parameter is not adequate to explain the locations of RSGs in the HRD as a function of metallicity.

2.6   Conclusions

We have analysed a total of 28 RSGs observed with VLT-XSHOOTER from the neighbouring galaxies LMC, SMC and WLM, by fitting the flux of the SED regions free from molecular features. Our main conclusions are as follows:

- We find an average RSG T_{eff} for WLM which is ~ 300 K warmer than that in either of the MCs. This trend of increasing average T_{eff} with decreasing Z is in qualitative agreement with theoretical predictions.

- From population synthesis analysis, we find that there is a systematic offset between expected and observed temperatures of RSGs at all metallicities. Specifically, RSGs in evolutionary models are too cool by ~ 200 K. This could be due to a wrong estimation of the mixing length parameter for 1D models of massive stars.

Chapter 3

Modelling the atmospheric extension of RSGs

The following chapter contains the publication González-Torà et al. (2023), published in Astronomy & Astrophysics (A&A), volume 669, pages A76, DOI:10.1051/0004-6361/202244503. The author performed the full analysis, discussion, writing and development of all the figures. The work has been carried out at the European Southern Observatory (ESO) headquarters in Garching, Germany since the author was awarded an ESO studentship.

3.1   Abstract

Red supergiants (RSGs) are evolved massive stars in a stage preceding core-collapse supernova. The physical processes that trigger mass loss in their atmospheres are still not fully understood, and they remain one of the key questions in stellar astrophysics. Based on observations of α Ori (Harper et al., 2001), a new semi-empirical method to add a wind to hydrostatic model atmospheres of RSGs was recently developed by Davies and Plez (2021). This method can reproduce many of the static molecular shell (or 'MOLsphere', e.g., Perrin et al., 2007; Ohnaka et al., 2009, 2011; Montargès et al., 2014; Kervella et al., 2018).

We used the method of adding a semi-empirical wind to a MARCS model atmosphere to compute synthetic observables as seen in Davies and Plez (2021) and Chapter 3, comparing the model to spatially resolved interferometric observations.

We present a case study to model published interferometric data of HD 95687 and V602 Car obtained with the AMBER instrument at the Very Large Telescope Interferometer (VLTI).

We computed model intensities with respect to the line-of-sight angle (μ) for different mass-loss rates, spectra, and visibilities using the radiative transfer code Turbospectrum (Plez, 2012). We were able to convolve the models to match the different spectral resolutions of the VLTI instruments, studying a wavelength range of $1.8 - 5\,\mu$m corresponding to the K, L, and M bands for GRAVITY and MATISSE data. The model spectra and squared visibility amplitudes were compared with the published VLTI/AMBER data.

The synthetic visibilities reproduce observed drops in the CO, SiO, and water layers that are not shown in visibilities based on MARCS models alone. For the case studies, we find that adding a wind onto the MARCS model with simple radiative equilibrium dramatically improves the agreement with the squared visibility amplitudes as well as the spectra, with the fit being even better when applying a steeper density profile than predicted from previous studies. Our results reproduce observed extended atmospheres up to several stellar radii.

This chapter shows the potential of our model to describe extended atmospheres in RSGs. It can reproduce the shapes of the spectra and visibilities with a better accuracy in the CO and water lines than previous models. The method can be extended to other wavelength bands for both spectroscopic and interferometric observations. We provide temperature and density stratifications that succeed, for the first time, in reproducing observed interferometric properties of RSG atmospheres.

3.2   Methods

In the absence of models that self-consistently explain winds of RSGs, we added a stellar wind with a constant $\dot{M}$ to an initial MARCS model (Gustafsson et al., 2008), following the method by Davies and Plez (2021). These models were then used to calculate both the synthetic spectra and the squared visibility amplitudes ($|V|^2$). This is described in detail in the following sections.

3.2.1   Models

We started with a MARCS model atmosphere. This code assumes local thermo-dynamic equilibrium (LTE), hydrostatic equilibrium, and spherical symmetry. We defined a radius grid for the model, allowing us to contain a more extended strat-ification up to $\sim 8.5\,R_\star$, where $R_\star$ is defined as the radius where the Rosseland opacity $\tau_{\rm Ross} = 2/3$. Moreover, for simplicity, we assumed that:

- The wind is in LTE. A discussion pertaining to this assumption can be found in Davies and Plez (2021).

- The model is 1D, so we assumed spherical symmetry.

To determine the outermost density, we used the mass continuity expression

$$\dot{M} = 4\pi r^2 \rho(r) v(r), \tag{3.1}$$

where ρ and v are the density and velocity as a function of the stellar radial coordinate r, respectively. The wind density $\rho_{\rm wind}(r)$ has the following shape proposed by Harper et al. (2001):

$$\rho_{\rm wind} = \frac{\rho_{\rm phot.}}{(R_{\rm max}/R\star)^2} \left(1 - \left(\frac{0.998}{(R_{\rm max}/R_\star)} \right)^\gamma \right)^\beta, \tag{3.2}$$

where $R_{\rm max}$ is the arbitrary outer-most radius of the model, in our case $8.5\,R_\star$. The β and γ parameters define the smoothness of the extended wind region and were initially set in the semi-empirical 1D model of α Ori by Harper et al. (2001): $\beta_{\rm Harp} = -1.10$ and $\gamma_{\rm Harp} = 0.45$. In Figure 3.1 we show what happens when changing the γ and β parameters that define the density profile. The variations of β mostly influence the smoothness of the density profile close to the stellar surface, while the variations of γ influence the full density profile to upper or lower values. We discuss the implications on spectra and interferometric visibility values in Section 3.3.2.1.

The velocity profile was found assuming a fiducial wind limit of $v_\infty = 25 \pm 5$ km/s, that is the value matched to Richards and Yates (1998); van Loon et al. (2005) and Beasor and Davies (2017), and Equation 4.1. We assumed no velocity gradient since the acceleration region is shallow and v_∞ is due to turbulent motions (see
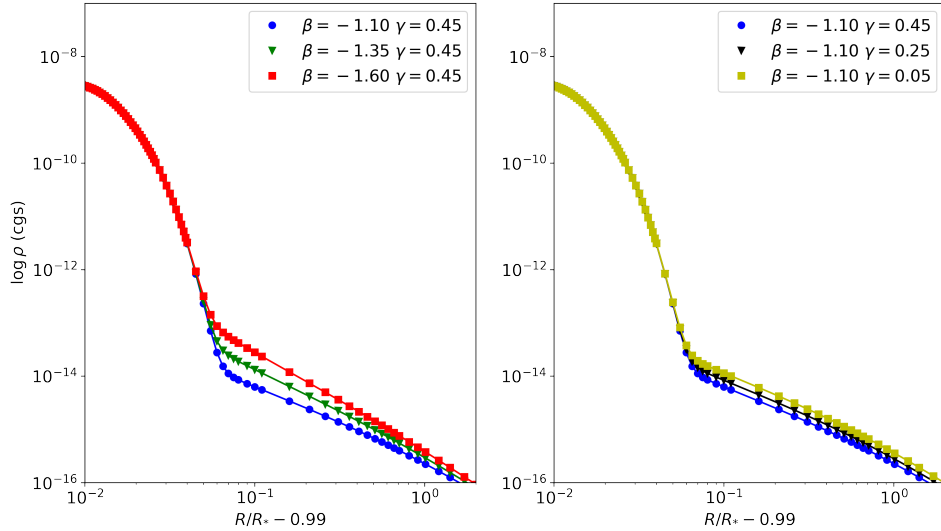
FIGURE 3.1: *Left:* Different density profiles for $\gamma = 0.45$ and variations of β with $\beta = -1.10$ (blue dots), -1.35 (green triangles), and -1.60 (red squares); we noticed that as we decreased β, the wind density near $R/R_\star - 0.99 = 10^{-1}$ increased and got steeper. *Right:* Different density profiles for $\beta = -1.10$ and the variations of γ with $\gamma = 0.45$ (blue dots), 0.25 (black triangles), and 0.05 (yellow squares). In this case, as we increased γ, the slope of the profile remained the same, but the values of the wind density gradually increased. The model used with $\log L/L_\odot = 4.8$, $T_{\rm eff} = 3500$ K, $\log g = 0.0$, $M = 15\,M_\odot$, and $\dot{M} = 10^{-5.0}\,M_\odot/\mathrm{yr}$ corresponds to the stellar parameters of HD 95687.

Davies and Plez, 2021). The model is sensitive to the density ρ, meaning that $\dot{M}$ and v are degenerate with one another.

For the temperature profile, we first used simple radiative transfer equilibrium (R.E.), defined as follows:

$$T(r_{\rm wind}) = T(\tau_{\rm Ross} = 2/3)\sqrt{R_\star/r_{\rm wind}}, \qquad (3.3)$$

where $\mathrm{T}(\tau_{\rm Ross}{=}2/3)$ and $R_\star$ are the temperature and radius at the bottom of the photosphere, and $T(r_{\rm wind})$ and $r_{\rm wind}$ are the temperature and radius of the wind extension, respectively. This results in a smoothly decreasing temperature profile for the extended atmosphere.

In addition, Davies and Plez (2021) defined a different temperature profile in their semi-empirical 1D model of α Ori by Harper et al. (2001), based on spatially resolved radio continuum data. The main characteristic of this profile is a temperature inversion in the chromosphere of the star that peaks at $\sim 1.4\,R_\star$ and

decreases again. ALMA and VLA observations of the RSGs Antares and Betelgeuse by Lim et al. (1998); O'Gorman et al. (2017) and O'Gorman et al. (2020) confirm the presence of such a lukewarm chromospheric temperature inversion, peaking at a radius of $1.3 - 1.5\,R_\star$ with a peak temperature of $\sim$3800 K. However, Lim et al. (1998) pointed out that optical and ultraviolet chromospheric signatures required higher temperatures of $\sim$5000 K at similar radii (Uitenbroek et al., 1996). Conversely, modelling spectroscopic and interferometric data of the CO MOLsphere derived gas temperatures of only 2000 K at $1.2 - 1.4\,R_\star$ (Ohnaka et al., 2013). O'Gorman et al. (2020) suggest that these components co-exist in different structures at similar radii in an inhomogeneous atmosphere, and that they are spatially unresolved by current measurements. Observations at different wavelengths may then be sensitive to different structures of this type.

Following Davies and Plez (2021), in our model setup, we included either a temperature profile in R.E., which may be more relevant for observations of the near-IR MOLsphere, or a temperature profile with a chromospheric temperature inversion which may be more relevant for chromospheric signatures in the optical or ultraviolet or for radio continuum observations.

Once the density, temperature, and velocity profiles were defined, we re-sampled the model to a constant logarithmic optical depth sampling $\Delta\log(\tau)$, and we used $0.01 < \Delta\log(\tau) < 0.05$. The reasons for this re-sampling are explained in Davies and Plez (2021): if the grid is too finely sampled, rounding errors can occur, leading to numerical difficulties. On the other hand, if the sampling is too coarse, the $\tau_\lambda = 2/3$ surface is poorly resolved for strong absorption lines.

Finally, we defined the outer boundary of the model where the local temperature is < 800 K, which is reached at $\sim 8.5\,R_\star$. Below this temperature, our code is unable to reliably converge the molecular equilibrium. In addition, some species would be depleted to dust grains. Figure 3.2 shows the density, temperature, velocity, and Rosseland opacity profiles for the example of an extended model with $\log L/L_\odot = 4.8$, $T_{\mathrm{eff}} = 3500$ K, $\log g = 0.0$, $M = 15\,M_\odot$, and $\dot{M} = 10^{-5.5}$ $M_\odot/\mathrm{yr}$.
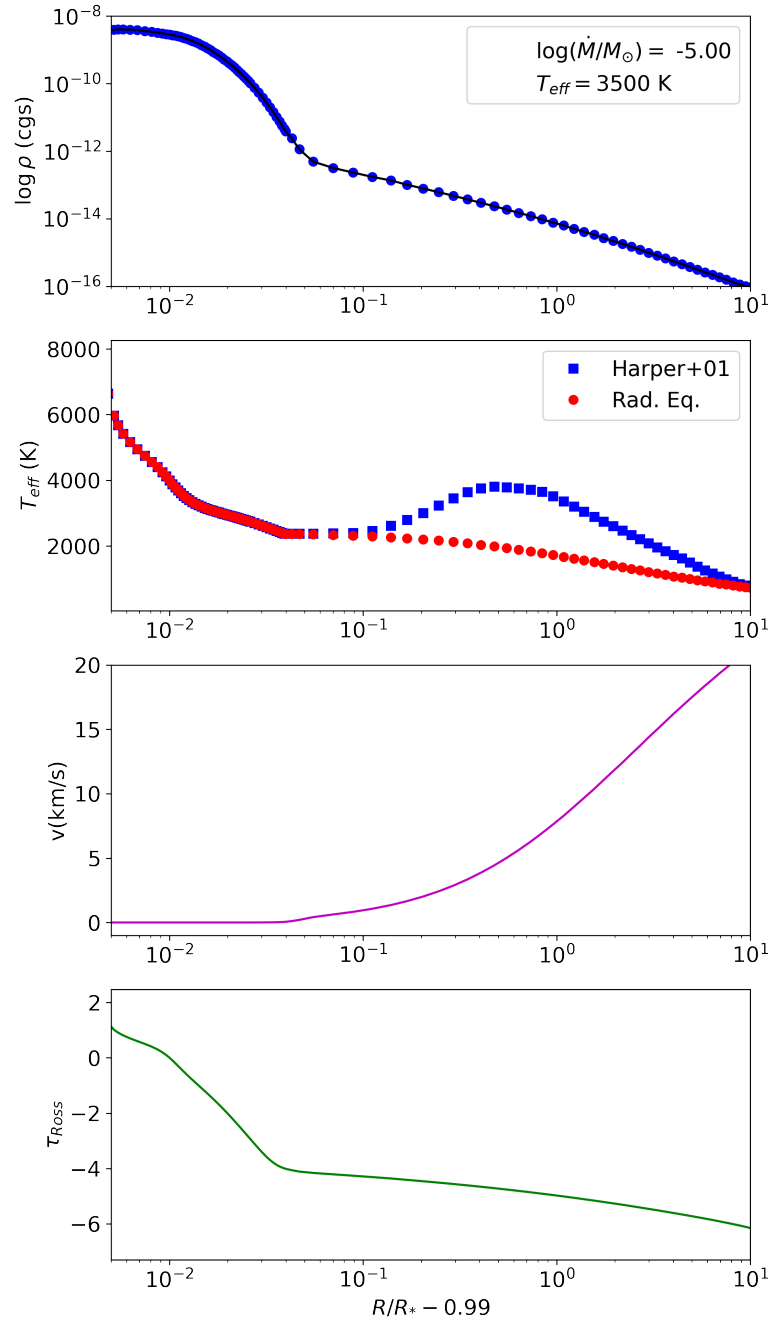
FIGURE 3.2: *From top to bottom:* Extended profiles for the density (blue dots), temperature (blue squares for temperature inversion by Harper et al. (2001) also known as 'Harper', and red circles for simple radiative equilibrium), wind velocity (purple), and Rosseland optical depth (green). The extended model with $\log \mathrm{L/L_\odot} = 4.8$, $T_{\mathrm{eff}} = 3500$ K, $\log g = 0.0$, $M = 15\,M_\odot$, $\dot{M} = 10^{-5.0}$ $M_\odot/\mathrm{yr}$, and $R_{\mathrm{max}} = 8.5\,R_\star$ corresponds to the stellar parameters of HD 95687.

3.2.2   Computation of model intensies

We computed both the spectra and the intensity profiles with respect to μ, where $\mu = \cos\theta$, with θ being the angle between the radial direction and the emergent ray, and $\cos\theta = 1$ corresponding to the intensity at the centre of the disk. For this we used the radiative transfer code TURBOSPECTRUM v19.1 (Plez, 2012). Setting a wavelength range from $1.8\,\mu$m to $5.0\,\mu$m with a step of $0.1\mathring{A}$, we explored the spectral range of the following instruments at the VLTI:

- GRAVITY (Gravity Collaboration et al., 2017) for the K band $1.8 - 2.5\,\mu$m.

- MATISSE (Lopez et al., 2022) for the L ($3.2 < \lambda < 3.9\,\mu$m) and M bands ($4.5 < \lambda < 5\,\mu$m). We did not use the N band ($8 < \lambda < 13\,\mu$m) because it is dominated by dust emission.

For the spectral synthesis, we included a list of atomic and molecular data. Chemical equilibrium was solved for 92 atoms and their first two ions, including Fe, Ca, Si, and Ti, and molecular data for CO, TiO, H_2O, OH, CN, and SiO was included, among about 600 species.

The spectra and visibilities can be convolved to any spectral resolution used by GRAVITY and MATISSE, or instruments at other interferometers. In this work, we show as an example the results convolved to match the HIGH spectral resolution of MATISSE: $R = 1000$[1].

3.2.3   Computation of model interferometric visibilities

To compute the visibility from the intensity profile, we used the following Hankel transform as in Davis et al. (2000):

$$V_{\text{Model}}(\lambda) = \int_0^1 S_\lambda I_\lambda^\mu J_0[\pi\theta_{\text{Model}}(B/\lambda)(1 - \mu^2)^{1/2}]\mu d\mu, \qquad (3.4)$$

where V_{Model} is the visibility of our model, S_λ is the instrument sensitivity curve, I_λ^μ is the computed intensities with respect to μ from TURBOSPECTRUM, J_0 is the zeroth order Bessel function, θ_{Model} is the angular diameter of the outermost

---

[1]The full spectral resolution models are available at CDS via https://cdsarc.cds.unistra.fr/cgi-bin/qcat?J/A+A/.

layer of the model, and B is the baseline of the observation. The V_{Model} was then normalised with respect to the total flux.

To estimate θ_{model}, we used the relation with the Rosseland angular diameter θ_{Ross},

$$\theta_{\text{Ross}} = \frac{R(\tau_{\text{Ross}} = 2/3)}{R_{\text{max}}} \theta_{\text{Model}}, \qquad (3.5)$$

found in Davis et al. (2000) and Wittkowski et al. (2004), where $R(\tau_{\text{Ross}} = 2/3)$ is the radius of the star at $\tau_{\text{Ross}} = 2/3$, defined as the photospheric layer, and R_{max} is the outer most radius of our model.

We used the definition in Wittkowski et al. (2017) to scale the final visibility of the model as

$$V(A, \theta_{\text{Ross}}) = A * V_{\text{Model}}(\theta_{\text{Ross}}), \qquad (3.6)$$

where A allows for the attribution of a fraction of the flux to an over-resolved circumstellar component (Arroyo-Torres et al., 2013), and $V_{\text{Model}}(\theta_{\text{Ross}})$ is the model visibility computed using Equation 3.4 with an associated Rosseland angular diameter θ_{Ross} from Equation 3.5.

3.3   Results

3.3.1   Base model

We computed the spectra, intensities, and $|V|^2$ for a base model of $T_{\text{eff}} = 3500$ K, $\log g = 0.0$, $[Z] = 0$, $\xi = 5$ km/s, $M = 15\,M_\odot$, $R_\star = 690\,R_\odot$, and $R_{\text{max}} = 8.5\,R_\star$, corresponding to a RSG similar to HD 95687 (Arroyo-Torres et al., 2015). The density parameters in Equation 4.2 are $\beta_{\text{Harp}} = -1.10$ and $\gamma_{\text{Harp}} = 0.45$ as in Harper et al. (2001) and the wind limit $v_\infty = 25$ km/s. The temperature profile was initially set to simple R.E., as we are interested in the near-IR K band MOLsphere (cf. Section 3.2.1). However, we also look at the effect of a chromospheric temperature inversion in Section 3.3.2.2. We used mass-loss rates of $\dot{M} = 10^{-4}$, 10^{-5}, 10^{-6}, and 10^{-7} $M_\odot$/yr, and a simple MARCS model without any wind. As an example, we simulated a star with $\theta_{\text{Ross}} = 3$ mas, a baseline of $B = 60$ m, and without any additional over-resolved component, that is $A = 1$. Figure 3.3 shows the intensities with respect to the extended stellar radius R_{max} for a cut in the continuum ($2.26\,\mu\text{m} < \lambda < 2.28\,\mu\text{m}$), the transition CO (2-0)
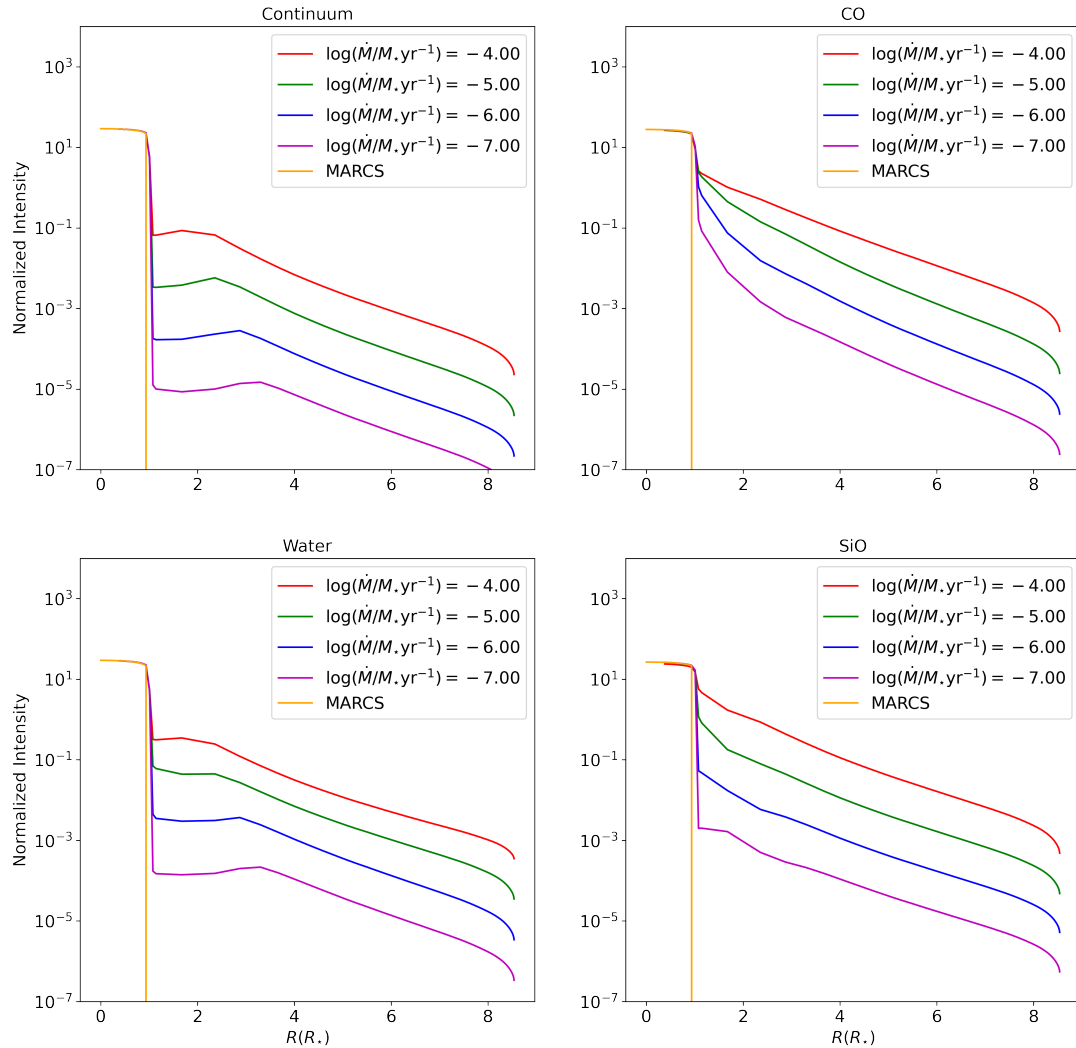
FIGURE 3.3: Intensity with respect to the $R_{\max}$ of our model for simple MARCS (orange), $\dot{M} = 10^{-4}$ (red), 10^{-5} (green), 10^{-6} (blue), and 10^{-7} $M_\odot$/yr (purple) and the different wavelength cuts corresponding to the following: the continuum ($2.26\,\mu m < \lambda < 2.28\,\mu m$, *upper left*), the transition CO (2-0) ($\lambda = 2.29\,\mu m$, *upper right*), water ($1.9\,\mu m < \lambda < 2.1\,\mu m$, *lower left*), and SiO ($\lambda = 4.0\,\mu m$, *lower right*). We observe an extension in all cases except for the MARCS model without the addition of a wind.

($\lambda = 2.29\,\mu m$), water ($1.9\,\mu m < \lambda < 2.1\,\mu m$), and SiO ($\lambda = 4.0\,\mu m$) for the different $\dot{M}$.

We observed an extension in all cases except for the MARCS model without the addition of a wind. The CO lines and the SiO lines seem to have the most prominent presence throughout the extended atmosphere (highest intensity compared to water or the continuum). Figures 3.4,3.5 and 3.6 show the spectra, the normalised spectra to the continuum, and squared visibility amplitudes ($|V|^2$) computed from
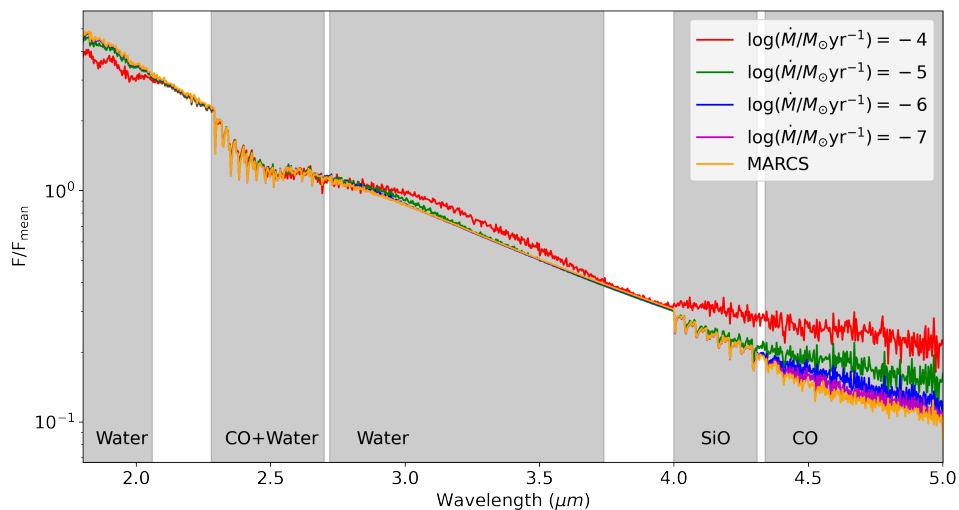
FIGURE 3.4: Normalised model spectra with respect to the mean flux for $\dot{M} = 10^{-4}$ (red), 10^{-5} (green), 10^{-6} (blue), and 10^{-7} $M_{\odot}$/yr (purple). We also plotted the spectra and visibilities based on the MARCS model without a wind (orange). This is the case for R.E. We have convolved the results with the spectral resolution of $R = 1000$. The main differences within models can be seen in the water, CO, and SiO molecular bands, the corresponding wavelength regions are highlighted in light grey.

our base model with the different $\dot{M}$, from highest $\dot{M} = 10^{-4}$ $M_{\odot}$/yr, to the simple MARCS model without wind.

When comparing the spectra and $|V|^2$ in Figures 3.4, 3.5 and 3.6, there are several things to notice:

- In Figures 3.4 and 3.5, the spectral signatures of CO in the wavelength range of $\lambda = 2.29 - 2.7\,\mu$m ($K$ band) do not strongly depend on the $\dot{M}$, as they remain relatively unchanged. Only at high $\dot{M}$ and high resolution spectra do the low excitation lines start to become stronger, as predicted by Tsuji (1988).

- In the region $\lambda > 4.0\,\mu$m (L and M bands), the spectra show the presence of SiO lines at wavelengths up to $\sim 4.3\,\mu$m, which seem to remain in absorption up to high $\dot{M}$ ($\sim 10^{-4}$ $M_{\odot}$/yr). At $\gtrsim 4.3\,\mu$m we observed the presence of CO as we increased the $\dot{M}$. The CO lines in the M band were already observed in emission at low $\dot{M}$ (starting at $\dot{M} = 10^{-6}$ $M_{\odot}$/yr), while the CO at the K band remained in absorption.
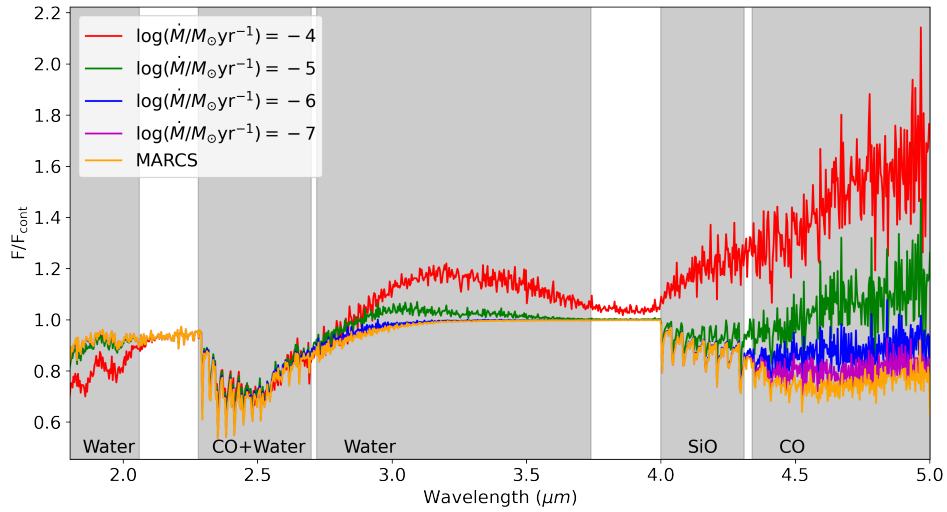
Figure 3.5: Same as Figure 3.4, but for the flux normalised to the continuum.
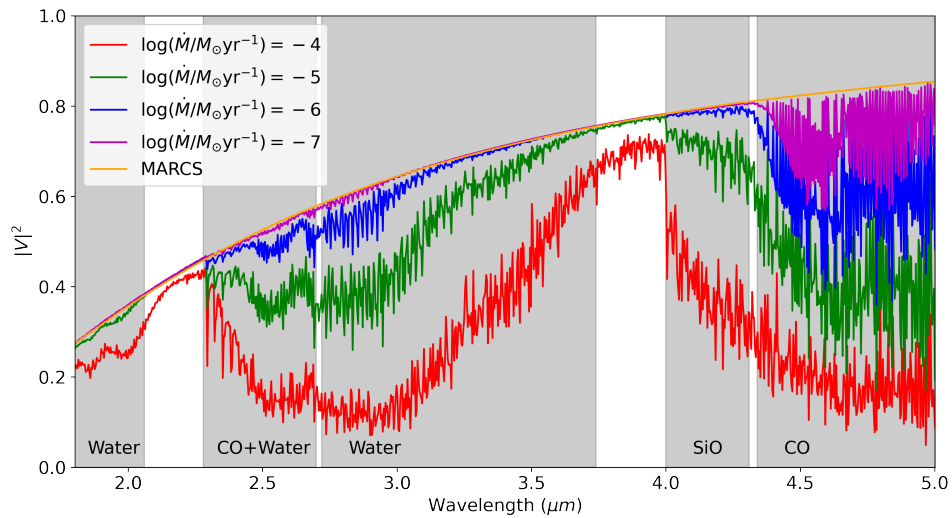
Figure 3.6: Same as Figure 3.4, but for the modelled visibility $|V|^2$. The baseline assumed is $B = 60$ m.

- In the $|V|^2$ (Figure 3.6), the most important thing to notice is that the extended molecular layers, mostly of the CO lines in $\lambda = 2.29 - 2.7\,\mu$m ($K$ band), are seen in the extended models. This extension was not reproduced earlier with MARCS or PHOENIX (Hauschildt and Baron, 1999) models alone.

- The CO extension increases with increased $\dot{M}$ (in all K, L and M bands). The atmospheric extension is best observed in the M band, as we already see a drop in $|V|^2$ for a low mass-loss rate of $\dot{M} = 10^{-7}\ M_\odot/$yr (in purple) as compared to a simple MARCS model with no extension (in orange).

- The visibility spectra are indicative of extended layers of water vapour (centred at $2.0\,\mu$m) for high $\dot{M}$ ($\gtrsim \dot{M} = 10^{-5}\ M_\odot/$yr), while the flux spectra are less sensitive. These water features are present in the observations of RSGs (e.g. Arroyo-Torres et al., 2015).

- Checking the $|V|^2$, we were not able to reproduce some atomic lines in the $2.10\,\mu$m $< \lambda < 2.30\,\mu$m region for mass-loss rates $\dot{M} < 10^{-4}\ M_\odot/$yr, which are the most sensitive to the stratification very close to the stellar surface (Kravchenko et al., 2020).

- Finally, when comparing both spectra and $|V|^2$, we see that while the CO absorption lines in the fluxes do not change between pure MARCS and MARCS+wind, the absorption features in the $|V|^2$ change considerably between simple MARCS and MARCS+wind models: while simple MARCS has no features at all, the $|V|^2$ presents strong drops with MARCS+wind. This could be because for the $|V|^2$ we are obtaining the spatial information (ie. observing the intensity with respect to the line of sight angle), so a drop on $|V|^2$ means that the CO is produced in this extended atmospheres. Since simple MARCS does not provide any extension at all, the drops will not be reproduced. However, when observing the flux, we see that for both models we obtain the same absorption components. This could be because when adding the wind, we will observe the flux integrated over the whole region, this flux will include the absorption feature at the line of sight gas material but also the emission of the CO produced at the surroundings of the gas. Both emission and absorption happening in the extended atmospheric material will contribute to the flux, cancelling each other so that we observe the same features as simple MARCS.

3.3.2 Variations of the base model

3.3.2.1 Density profile

So far, we have assumed the density parameters (Equation 4.2) from Harper et al. (2001): $\beta_{\mathrm{Harp}} = -1.10$ and $\gamma_{\mathrm{Harp}} = 0.45$. Figure 3.7 shows the spectra and $|V|^2$ for the K band for the different β values defined in Figure 3.1. We did not include the variations on γ because these produce an almost identical plot. Although the spectra remain unchanged by variations of β, the $|V|^2$ change slightly: as the density profile gets steeper (i.e. lower β or γ values), the extension features due to water in $\lambda = 2.35 - 2.5\,\mu\mathrm{m}$ become more prominent. This can be understood as water layers form close to the stellar surface (Kravchenko et al., 2020), and therefore are sensitive to variations in the density profile in this region. The measurements by Harper et al. (2001) and their constraints of β and γ were less sensitive to the region very close to the stellar surface.

Furthermore, in Figure 3.8 we show the spectra in the optical TiO region ($\lambda = 0.5 - 0.75\,\mu\mathrm{m}$) to see the effect of changing the β parameter in the TiO lines. Again, changing the γ parameter produces a very similar plot. A discussion concerning the general effect of this semi-empirical model on the TiO bands can be found in Davies and Plez (2021). Briefly, an increase in the mass-loss rate causes the TiO absorption lines to deepen, shifting the star to later spectral types (e.g. for a zero-wind model of spectral type M0, if we apply $\dot{M} = 10^{-6}$, $\dot{M} = 10^{-5.5}$, and $\dot{M} = 10^{-5}\ M_\odot/\mathrm{yr}$ in our model the star is classified as M1, M2, and $>$M5, respectively). Changing the density profile parameters with a fixed $\dot{M}$ affects the TiO bands, also shifting the stellar classification slightly to later spectral types as we deepen the TiO bands (Figure 3.8). On the other hand, the TiO bands may be more sensitive to a higher chromospheric temperature component than the molecular layers in the near-IR, which may cause the TiO lines to be less deep (cf. Section 3.2.1).

3.3.2.2 Temperature profile

Figures 3.9 and 3.10 show the spectra and $|V|^2$ for our two temperature stratifications defined in Section 3.2, R.E and temperature inversion, with $\dot{M} = 10^{-4}$ $M_\odot/\mathrm{yr}$ and $\dot{M} = 10^{-6}\ M_\odot/\mathrm{yr}$, respectively.
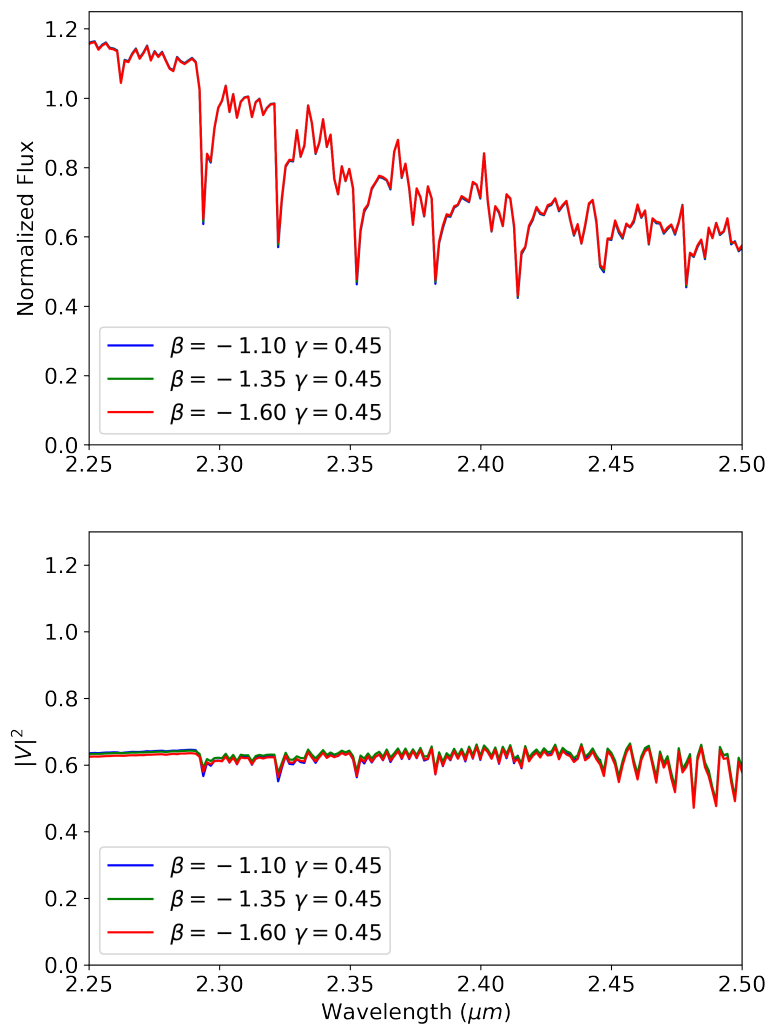
FIGURE 3.7: Normalised model spectra (*upper panel*) and $|V|^2$ (*lower panel*) for a fixed $\gamma = 0.45$ and the different $\beta = -1.10$ (blue), -1.35 (green), and -1.60 (red) in the K band. The baseline used is $B = 63.8$ m, corresponding to the case study of HD 95687 in Section 3.4. We can see that as the β gets lower, the water features in $\lambda = 2.35 - 2.5\,\mu$m become slightly more prominent.

When comparing both temperature profiles in Figures 3.9 and 3.10, we see the main difference in the CO lines: in the K band region $\lambda = 2.29 - 2.7\,\mu$m, the CO is in emission when using the temperature inversion profile (as also predicted by O'Gorman et al., 2020), while for R.E. it remains in absorption even for very high $\dot{M}$ such as $\dot{M} = 10^{-4}\ M_\odot/$yr. This difference can be seen in the lower panels of Figures 3.9 and 3.10, where the R.E. shows less extension in the CO region as compared with the temperature inversion. For lower mass-loss rates ($\dot{M} = 10^{-6}$ $M_\odot/$yr, Figure 3.10), it gets harder to see the difference in both profiles. The only region that seems to make a difference is the M band ($4.5 < \lambda < 5\,\mu$m), where we
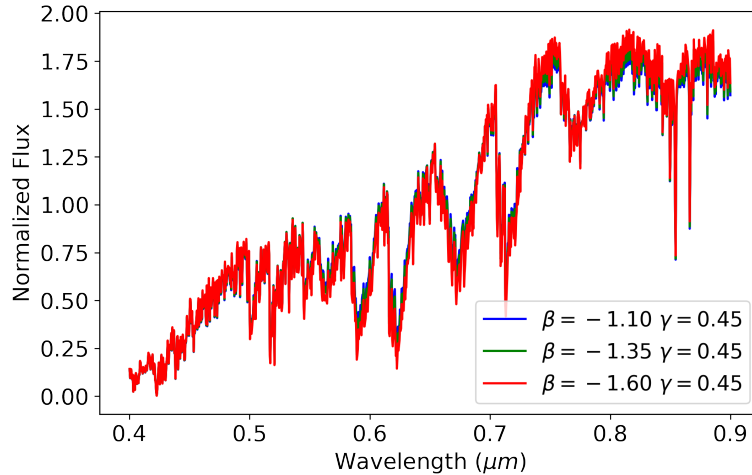
FIGURE 3.8: Normalised model spectra for a fixed $\gamma = 0.45$ and the different $\beta = -1.10$ (blue), -1.35 (green), and -1.60 (red) in the optical TiO band region. As we decrease β, the TiO bands deepen slightly.

see emission in the temperature inversion case.

Observations of CO lines in the K band generally show CO in absorption, even for an extreme case such as the RSG VY CMa (Wittkowski et al., 2012), confirming that the lower temperature based on R.E. is better suited to describe the CO MOLsphere than the higher temperature components of the chromospheric temperature inversion (cf. Section 3.2.1).

To sum up this section, the MARCS+wind model shows significant atmospheric extension in all wavelengths compared to a simple MARCS model (Figure 3.3). Such an extension has been observed, but it has so far not been reproduced by current models (Arroyo-Torres et al., 2013). As we increase the $\dot{M}$ for a R.E. temperature profile, the CO, SiO, and water remain relatively unchanged in the spectra (Figure 3.4); whereas for the $|V|^2$, we see a larger extension in all cases (Figure 3.6). The R.E. seems to better reproduce the spectra than the temperature inversion as we did not observe the CO in emission in our case studies (see Section 3.4) nor other previously published data (e.g. Wittkowski et al., 2012; Arroyo-Torres et al., 2013, 2015). Changing the β and γ parameters in Equation 4.2 deepens the water features in the $|V|^2$.
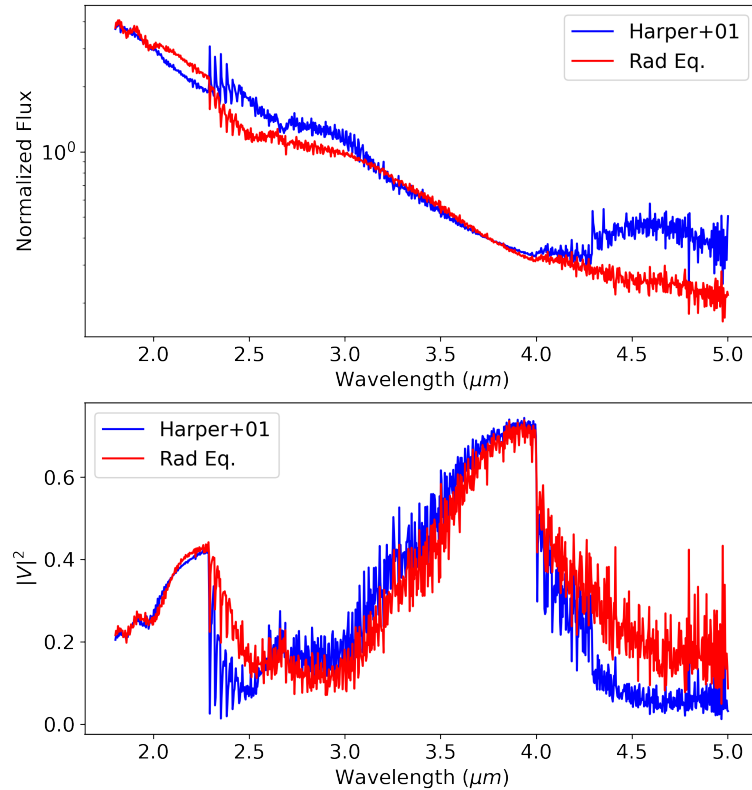
FIGURE 3.9: Normalised model spectra (*upper panel*) and $|V|^2$ (*lower panel*) for our base model with simple radiative equilibrium (red) and the chromospheric temperature inversion profile by Harper et al. (2001) (blue). Both models with a $\dot{M} = 10^{-4.0}$ $M_\odot$/yr. We can see that the main differences are in the regions $\lambda = 2.35 - 3.0\,\mu$m and $\lambda > 4.0\,\mu$m due to CO, where for the *Harper+01* case the molecular lines appear more strongly in emission, and the visibilities are decreased due to a larger apparent diameter of the star.
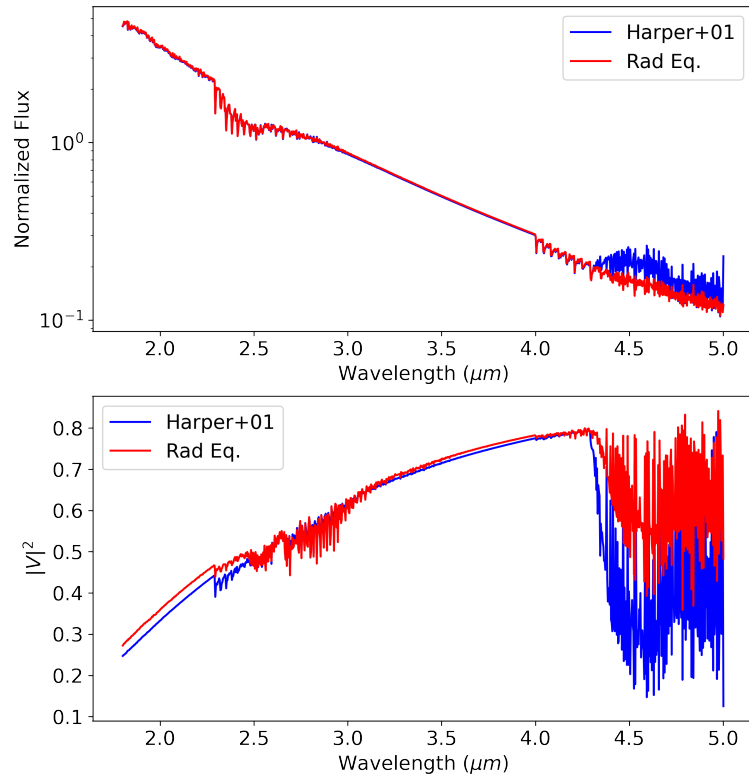
Figure 3.10: Same as Figure 3.9, but with a $\dot{M} = 10^{-6.0}\ M_\odot/\mathrm{yr}$. In this case, the main differences are only in the $\lambda > 4.0\,\mu$m region due to CO, where for the *Harper+01* case the molecular lines appear more strongly in emission, and the visibilities are decreased due to a larger apparent diameter of the star.

3.4 Case study: Comparison with HD 95687 and V602 Car

In this section, we compare our model to published VLTI/AMBER data of the two RSGs HD 95687 and V602 Car available in Arroyo-Torres et al. (2015). As previously mentioned, we have chosen these two RSGs since they sample different luminosities, $\dot{M}$, and masses. In addition, the data are readily available, and these are two well-studied RSGs whose fundamental parameters (e.g. $T_{\rm eff}$, $\log g$, $\theta_{\rm Ross}$, and $\log L/L_{\odot}$) are well known. The data were taken using the AMBER medium-resolution mode ($R \sim 1500$) in the $K - 2.1\,\mu$m and $K - 2.3\,\mu$m bands.

The parameters used for each initial MARCS model are shown in Table 4.5, following Arroyo-Torres et al. (2015). HD 95687 is characterised by a smaller luminosity, mass, and radius than V602 Car. In addition, HD 95687 shows a weaker atmospheric extension than V602 Car.

To estimate both $\theta_{\rm Ross}$ and A, for each studied model, we computed the $|V|^2$ as a function of their spatial frequency B/λ_o where λ_o corresponds to the continuum region $2.23 - 2.27\,\mu$m. We have compared the model and data $|V|^2$, and found the best-fitting $\theta_{\rm Ross}$ and A by means of a χ^2 minimisation.

Figures 3.11 and 3.12 show the MARCS model fit to the data of Arroyo-Torres et al. (2015) and our initial MARCS+wind model fit with $\beta_{\rm Harp} = -1.10$ and $\gamma_{\rm Harp} = 0.45$, compared to the data of HD 95687 and V602 Car, respectively. For our model fit, we checked both the spectra and $|V|^2$. We used a range of mass-loss rates of $-7 < \log \dot{M}/M_{\odot} < -4$ with a grid spacing of $\Delta \dot{M}/M_{\odot} = 0.25$. We obtained a best fit of $\log \dot{M}/M_{\odot} = -5.50$ for HD 95687 and $\log \dot{M}/M_{\odot} = -5.0$ for V602 Car. These $\dot{M}$ are reasonable when compared with typical mass-loss

Table 3.1: Parameters of the MARCS models used for the analysis of each RSG. From left to right: Luminosity $\log L/L_{\odot}$, effective temperature $T_{\rm eff}$, surface gravity $\log g$, metallicity [Z], microturbulence ξ, and mass as in Arroyo-Torres et al. (2015). The last column shows the radius of the star in the photosphere in solar units (defined at $\tau_{\rm Ross} = 2/3$).

RSG	$\log L/L_{\odot}$	$T_{\rm eff}$ (K)	$\log g$	[Z]	ξ (km/s)	$M/M_{\odot}$	$R_{\star}/R_{\odot}$
HD 95687	4.8	3500	0.0	0	5	15	690
V602 Car	5.1	3400	-0.5	0	5	20	1015

prescriptions (e.g. de Jager et al., 1988; Schröder and Cuntz, 2005; Beasor et al., 2020).

For the temperature profile, we used R.E. since the temperature inversion would either show depleted CO lines ($\lambda = 2.29 - 2.7\,\mu$m) for the spectra, which do not match with the observations, or not enough extension for the $|V|^2$. Therefore, it is not possible to find a model with the temperature inversion profile that fits both spectra and $|V|^2$ simultaneously.

We estimate for our best-fit models a $\theta_{\mathrm{Ross}} = 5.35 \pm 0.7$ mas and 2.9 ± 0.8 mas, and $A = 1.0 \pm 0.14$ and 1.0 ± 0.08 for V602 Car and HD 95687, respectively. The errors in θ_{Ross} and A were derived by the minimum values in the 68% dispersion contours of the χ^2 fit, which for 2 degrees of freedom corresponds to $\chi^2 < \chi^2_{\mathrm{min}} + 2.3$ (Avni, 1976). Our results are in agreement with Arroyo-Torres et al. (2015) within the error limits.

In this work, we show that when adding a wind to a MARCS model, we are now able to qualitatively fit the spectra and $|V|^2$. This is something that current existing models are unable to do.

This initial fit can be further improved by modifying the inner wind density profile. Figures 3.13 and 3.14 show both the spectra and $|V|^2$ of the new fit changing the density parameters in comparison with the data and the initial MARCS+wind fit for HD 95687 and V602 Car, respectively. The main difference between both MARCS+wind models can be found in the $|V|^2$ water region at $\lambda = 2.29 - 2.5\,\mu$m, where the new γ and β fit better.

We notice that, although our best-fit model for HD 95687 can accurately reproduce both flux and $|V|^2$, this succeeds for V602 Car to a lower extent: the flux is well reproduced in Figure 3.14, but the $|V|^2$ is still missing some extension, especially in the region $\lambda = 2.29 - 2.5\,\mu$m. As previously mentioned, this region not only includes CO, but also the presence of water. A possible explanation for this mismatch could be that for increasing $\dot{M}$, the models still fail to reproduce the extension of the water or CO layers. Another possibility is that since our model neglects velocity gradients, it underestimates the equivalent widths of lines. Broader and stronger lines would help to increase the apparent stellar extension at those wavelengths.
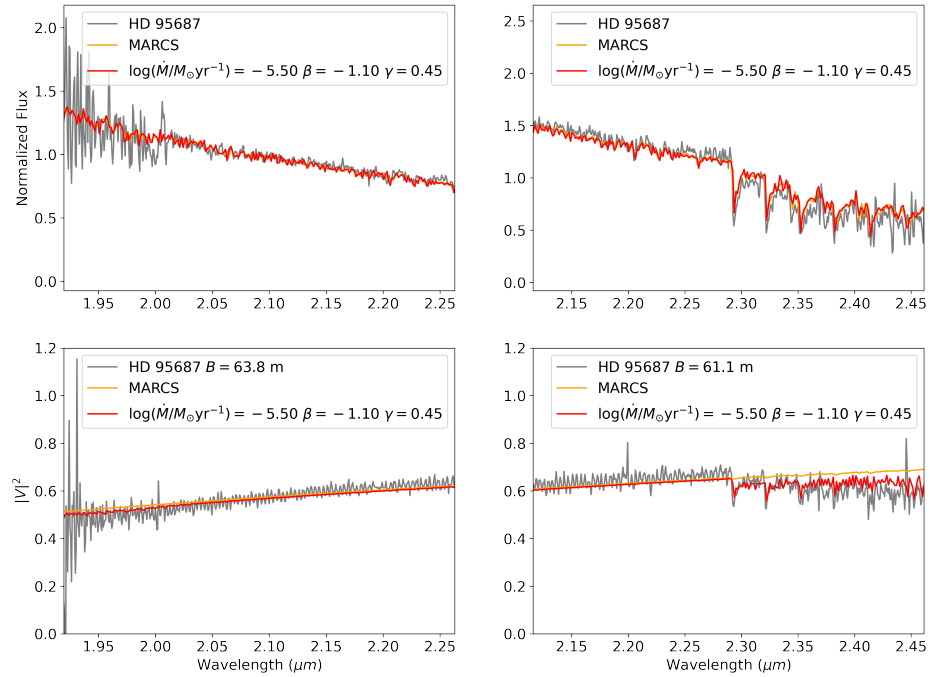
Figure 3.11: *Upper left:* Normalised flux for the RSG HD 95687 (grey), as observed with VLT/AMBER for the $K - 2.1\,\mu$m bands. Our initial best-fit model with $\beta = -1.10$ and $\gamma = 0.45$ is shown in red, corresponding to the parameters of the density profile by Harper et al. (2001). The pure MARCS model fit is shown in orange. As expected, the fluxes are well represented by both our fit and MARCS. *Upper right:* Same as the upper left panel, but for the $K - 2.3\,\mu$m band. *Lower left:* Same as the upper left panel, but for the $|V|^2$ and a baseline of $B = 60.8$ m. *Lower right:* Same as the lower right panel, but for the $K - 2.3\,\mu$m band and a baseline of $B = 63.2$ m. Our model can represent the data better than simple MARCS.
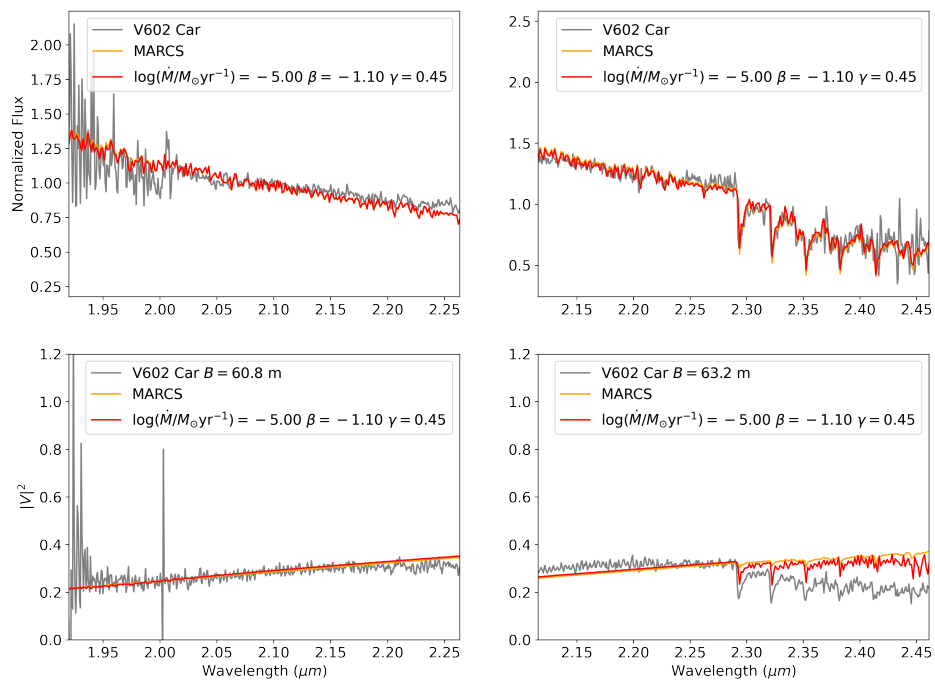
Figure 3.12: Same as Figure 3.11, but for V602 Car.
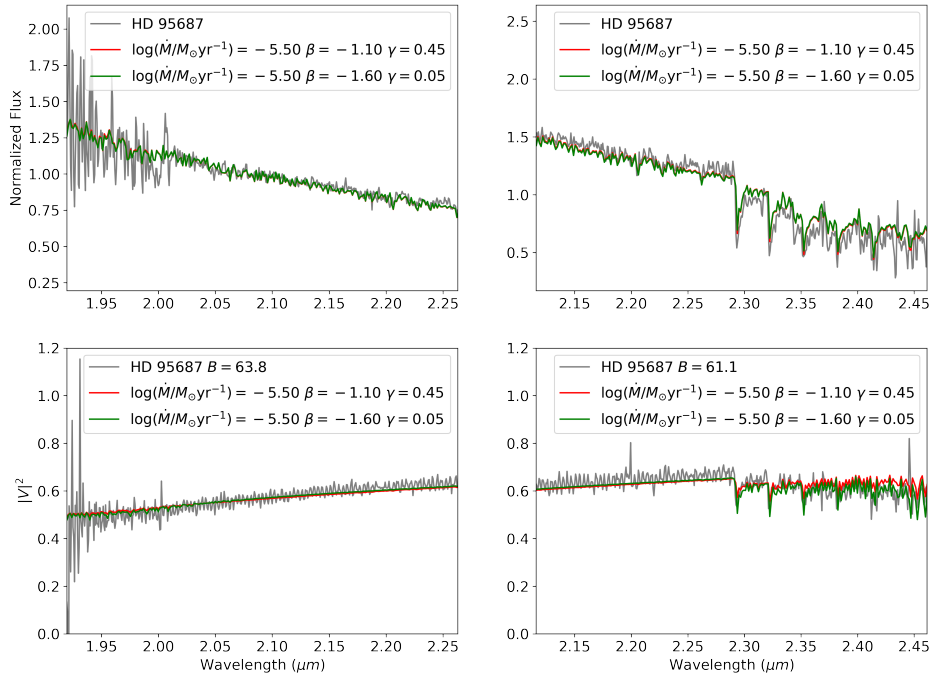
Figure 3.13: *Upper left:* Normalised flux for the RSG HD 95687 (grey), as observed with VLT/AMBER for the $K - 2.1\,\mu$m bands. Our initial best-fit model with $\beta = -1.10$ and $\gamma = 0.45$ is shown in red, corresponding to the parameters of the density profile by Harper et al. (2001). The final best-fit model with $\beta = -1.60$ and $\gamma = 0.05$ is shown in green. *Upper right:* Same as the upper left panel, but for the $K - 2.3\,\mu$m band. *Lower left:* Same as the upper left panel, but for the $|V|^2$ and a baseline of $B = 60.8$ m. *Lower right:* Same as the lower right panel, but for the $K - 2.3\,\mu$m band and a baseline of $B = 63.2$ m. The best-fit model for β and γ can reproduce the water features in $\lambda = 2.29 - 2.5\,\mu$m with a better accuracy than our initial best fit.
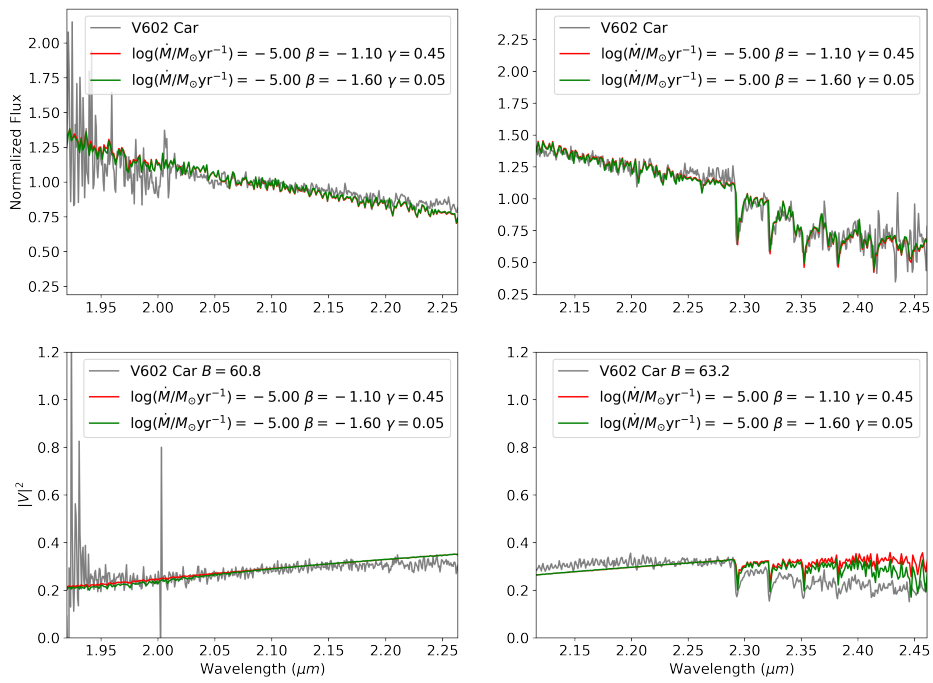
FIGURE 3.14: Same as Figure 3.13, but for V602 Car.

3.5   Summary and conclusion

We present 1D modelling for the extended atmospheres of RSGs based on simple R.E. and chromospheric temperature inversion by Harper et al. (2001), and we computed synthetic flux spectra and synthetic interferometric visibility spectra. When comparing our models to a simple MARCS or PHOENIX models, our synthetic $|V|^2$ showed a stronger atmospheric extension and could fit, for the first time, the observed extension in the case studies.

Regarding the temperature profile, we find that the R.E. reproduces the spectra better than the chromospheric temperature inversion since we do not observe any emission in the CO bands, which are the result of models based on a temperature inversion. The possible reason that R.E. fits better than the temperature inversion – even though RSGs are known to have a chromosphere – could be, on the one hand, because of the presence of different spatial cells with different temperatures in the hot lukewarm chromospheres of RSGs (O'Gorman et al., 2020). On the other hand, we do not know the effect that the dust could make where $T > 800$ K; although, we expect it to be small.

Moreover, localised gaseous ejections, related to magnetic fields and surface activity were recently suggested as a major contributor to mass loss from RSGs (Humphreys and Jones, 2022; Andrews et al., 2022; López Ariste et al., 2022). To explore this effect in detail, we would need to use 3D models, which is out of the scope of this work. Our 1D modelling approach relies on an azimuthally averaged stratification, which is a good approximation for many aspects, but may not reproduce some of the observed features.

When compared to the observations, we obtain a mass-loss rate that is in accordance with typical mass-loss prescriptions (e.g. de Jager et al., 1988; Schröder and Cuntz, 2005; Beasor et al., 2020). However, in order to fit both the water and CO extensions simultaneously, the density shape should be steeper close to the surface of the star than previously expected by Harper et al. (2001).

Most importantly, we were able to reproduce the $|V|^2$ extension of the case studies. Simple stellar atmosphere models such as MARCS do not show extension at all. However, the description very close to the stellar surface may not be optimum yet, as we were not able to reproduce some atomic lines in the $2.10\,\mu\mathrm{m} < \lambda < 2.30\,\mu\mathrm{m}$

$|V|^2$ region, which are the most sensitive to the stratification very close to the stellar surface.

This is the first extended atmosphere model to our knowledge that can reproduce, in great detail, both the spectra and $|V|^2$ simultaneously. Therefore, we have shown the immense potential of this semi-empirical model of MARCS+wind, not only to match the spectral features without the need of dusty shells, but also the visibilities obtained by interferometric means.

Chapter 4

Further modelling with GRAVITY and MATISSE data

The following chapter contains the publication to be submitted to A&A, where the author performed the full data calibration, reduction, analysis, discussion, writing and development of all the figures. The work has been carried out at the European Southern Observatory (ESO) headquarters in Garching, Germany.

4.1   Abstract

Mass loss plays a crucial role in the lives of massive stars, especially as the star leaves the main sequence and evolves all the way to the red supergiant (RSG) phase. Despite its importance, the physical processes that trigger mass-loss events in RSGs are still not well understood. In Chapter 3, we have shown that adding the effect of a semi-empirical wind can accurately reproduce the extensions in the atmospheres of RSGs, where the mass-loss events are taking place, particularly focusing in the CO and water lines.

In this chapter, by adding a static wind to a MARCS atmospheric model, we compute the synthetic observables to match the new interferometric data taken with VLTI/MATISSE and VLTI/GRAVITY for the RSGs AH Sco, KW Sgr, V602 Car, CK Car and V460 Car. KW Sgr uses published VLTI/AMBER data instead of GRAVITY. The MATISSE wavelength range also includes the presence of the SiO molecule at $4.0\,\mu$m with a spectral resolution of $R \sim 500$. The model intensities

with respect to the line of sight angle (μ) as well as the spectra and visibilities were computed using the stellar transfer code TURBOSPECTRUM. We found the best-fit model, mass-loss rate and best-fit angular Rosseland diameter for the observations. Then, we simultaneously match our model to the data studying a wavelength range of $1.8 - 5.0\,\mu$m corresponding to the K, L and M bands.

We obtain a range of Rosseland angular diameters between $3.00 < \theta_{\mathrm{Ross}} < 5.05$ mas and a range of mass-loss rates of $-6.5 < \log \dot{M}/M_{\odot}\mathrm{yr}^{-1} < -4$ over all our targets. Moreover, we are able to reproduce the drops in the visibilities due to CO, water and SiO. The SiO abundance is shown to start increasing at $R \sim 2R_{\star}$ and its relative intensity depends on the luminosity assumed in our model.

This work provides further demonstration that our MARCS+wind model can reproduce the observed physical extension of RSG atmospheres for several spectral diagnostics spanning a broad wavelength range. We reproduce both spectra and visibilities of newly obtained data as well as provide temperature and density stratifications that are consistent with the observations. With the new MATISSE data, we studied the extension of SiO as a precursor of silicate dust.

4.2 Observations and data reduction

We observed the RSGs KW Sgr (ID: 109.231U.001, PI:Wittkowski), AH-Sco (ID: 109.231U.002, PI:Wittkowski), V602 Car, CK Car and V460 Car (ID:110.23P1.001, PI: González-Torà) with VLTI/MATISSE. We also observed AH Sco (ID:0101.D-0616(B), PI: Wittkowski), V602 Car and VAR Cet (ID:110.23.P1.002, PI: González-Torà) with VLTI/GRAVITY.

For the GRAVITY observations ($1.8 < \lambda < 2.4\,\mu$m), the targets were observed as snapshots with single split-polarisation mode and the medium interferometric baseline configuration. We used the HIGH spectral resolution $R \sim 4000$ mode. The sequences were observed as CAL-SCI-CAL, meaning we first observed a calibrator, then the science target and again a calibrator. For each of these three observations, the sequence was OOSOOS, where O denotes the object (SCI or CAL) and S the sky position. The sequences were observed for the same night, using two different calibrators for the same science target.

For the MATISSE observations ($2.8 < \lambda < 13 \, \mu$m), the targets were observed as snapshots with the medium interferometric baseline configuration. For the L and M bands we used the MED spectral resolution $R \sim 500$, while for the N band the HIGH $R \sim 1000$ for AH Sco and KW Sgr, and LOW $R \sim 30$ for V602 Car, CK Car and V460 Car. We observed the sequences CAL-L, SCI, CAL-N for the same night, where CAL-L is the calibrator for the L and M bands, SCI is the science target and CAL-N is the calibrator for the N band. Usually, we cannot use the same calibrators for the L/M and N bands, since we need specific angular diameters and magnitudes that depend on the bands we are observing. Our observations were all taken with the new GRA4MAT mode, to obtain the full wavelength coverage of $2.8 < \lambda < 5 \, \mu$m in the L and M bands.

The date and time of the observations, as well as the observing conditions are shown in Tables 4.1 and 4.2 for GRAVITY and MATISSE, respectively. The stellar properties of our observed calibrators are shown in Table 4.3.

The targets studied are variable stars, whose variability between times of observations could affect the results. We have checked the dates when the observations were taken in Tables 4.1 and 4.2 and compared with the light curves of the targets using the enhanced light curves available by the *American Association of Variable Star Observers*[1]. For the case of AH Sco and KW Sgr, in both cases the observations were taken around the minimum of the variability cycles. For the other RSGs, the observations were taken with less than a month, so the variability of the stars in this short period would not affect our results.

4.2.1 Data reduction

For the data reduction, we used the ESOReflex software with the GRAVITY pipeline version 1.6.0 and the MATISSE pipeline version 1.7.6[2]. The steps of the data reduction for both instruments are described in Lapeyrere et al. (2014) and Millour et al. (2016), respectively. The $|V|^2$, the visibilities, closure phases, differential phases and coherent fluxes are calculated by the pipeline.

Once the raw data has been reduced, the second ESOReflex workflow calibrates the visibilities of the science data using the different calibrators. For MATISSE,

---

[1] https://www.aavso.org/LCGv2/
[2] The reduction pipelines are available at http://www.eso.org/sci/software/pipelines/

TABLE 4.1: Summary of the VLTI/GRAVITY data obtained for the five observed RSGs and their calibrators: the target name, the date when the observation was taken, UT time at the start of the observation, the seeing of the science target, the coherence time τ_0 at the start of the observation, calibrator name, seeing of the calibrator, coherence time of the calibrator, and AT configuration.

Target	Date	UT	Seeing sci ('')	τ_0 (ms)	Calibrator	Seeing calib ('')	τ_0 (ms)	AT configuration
AH Sco	17-06-18	01:21:25	1.09	2.23	HD159881	1.05	3.60	K0G2D0J3/Medium
					HD152636	0.89	2.23	K0G2D0J3/Medium
V602 Car	22-01-23	05:23:32	0.65	8.20	HD96442	0.7	7.94	K0G2D0J3/Medium
					HD103859	0.63	7.84	K0G2D0J3/Medium
CK Car	22-01-23	04:34:00	0.68	7.5	HD89736	0.71	6.9	K0G2D0J3/Medium
					HD90677	0.82	6.1	K0G2D0J3/Medium
V460 Car	25-11-22	05:40:34	0.75	9.1	Q Car	1.06	6.5	K0G2D0J3/Medium
					HD 60228	0.65	11.1	K0G2D0J3/Medium

TABLE 4.2: Summary of the VLTI/MATISSE data obtained for the five observed RSGs and their calibrators: the target name, the date when the observation was taken, UT time at the start of the observation, the seeing of the science target, the coherence time τ_0 at the start of the observation, calibrator name, seeing of the calibrator, coherence time of the calibrator, and AT configuration.

Target	Date	UT	Seeing sci ($''$)	τ_0 (ms)	Calibrator	Band	Seeing calib ($''$)	τ_0 (ms)	AT configuration
AH Sco	26-08-22	23:45:59	0.43	7.2	gam02 Nor	L&M	0.81	6.7	K0G2D0J3/Medium
					eps Sco	N	0.33	8.0	K0G2D0J3/Medium
KW Sgr	28-08-22	00:16:46	0.43	3.1	nu Oph	L&M	0.65	3.5	K0G2D0J3/Medium
					eps Sco	N	0.45	4.2	K0G2D0J3/Medium
V602 Car	19-01-23	06:57:36	0.65	1.62	HD94683	L&M	0.73	1.97	K0G2D0J3/Medium
					HD91056	N	0.51	1.91	K0G2D0J3/Medium
CK Car	27-02-23	03:16:25	0.46	9.4	HD94683	L&M	0.88	8.3	K0G2D0J3/Medium
					HD302821	N	0.44	13.2	K0G2D0J3/Medium
V460 Car	26-12-22	04:06:43	1.16	2.5	zet Vol	L&M	0.93	2.9	K0G2D0J3/Medium
					CD-55 3254	N	0.86	2.9	K0G2D0J3/Medium

Table 4.3: Properties of the calibrators for the VLTI/MATISSE and GRAV-
ITY observations: name, spectral type, limb-darked disk diameter (LDD) from
Bourges et al. (2017), and the stellar parameters of the synthetic spectra
(MARCS, Gustafsson et al., 2008) used for the calibrators: effective temper-
ature (T_{eff}), surface gravity ($\log g$) and metallicity [Z] available in the VizieR
database of astronomical catalogues (Ochsenbein et al., 2000).

Name	Spectral type	LDD diameter (mas)	T_{eff} (K)	$\log g$	[Z]
gam02 Nor	K0III	2.46±0.25	4750	3.0	0.25
eps Sco	K1III	5.93±0.45	4500	2.5	-0.25
nu Oph	K1III	2.83±0.29	5000	3.0	0.00
HD94683	K4III	2.49±0.25	4000	0.0	0.00
HD91056	M0III	4.40±0.49	3800	1.0	0.00
HD16074	K2III	1.77±0.13	4250	-0.5	0.00
ups Cet	M0III	5.91±0.76	3800	1.15	-0.05
HD302821	A7Ie	1.26±0.10	3700	0.00	0.00
zet Vol	K0III	2.23±0.21	4700	2.5	-0.2
CD-55 3254	M3	2.76±0.27	3300	0.00	0.00
HD159881	K5III	2.81±0.24	4500	2.5	-0.25
HD152636	K5III	2.39±0.22	4000	2.5	-0.05
HD96442	M1/2III	1.64±0.16	4000	0.00	0.00
HD103859	K4III	1.43±0.11	4000	0.00	0.00
80 Cet	M0III	3.57±0.36	4000	0.00	0.00
HD89736	K5/M0III	2.58±0.23	3900	0.00	0.00
HD90677	K3II	1.99±0.19	4000	0.00	0.00
Q Car	K3III	2.45±0.27	4300	0.00	0.00
HD60228	M1III	2.51±0.24	3900	0.00	0.00

the calibration workflow changes slightly for both L/M and N bands: for the N
band, we used the coherent integration instead, and we have changed the spectral
binning to 11 bins/λ and the coherent integration time to 0.3 s.

ESOreflex does not provide us with a flux calibration method, therefore we
calibrated the flux by our own means. The flux calibration for the GRAVITY and
MATISSE data was done with the following steps, for each of the four telescopes:
firstly, the data was corrected for the offsets of the absolute wavelength calibration,
by checking a sky model for the whole K band using the SkyCalc Model calculator
(Noll et al., 2012; Jones et al., 2013) and the individual telluric lines at $\lambda =
3.903\,\mu$m for the L and M bands and $\lambda = 9.576\,\mu$m for the N band. Table 4.4
shows the offsets of the absolute wavelength calibration for each band and target.

Secondly, the calibrator flux was divided by the MARCS model flux, using the
parameters in Table 4.3 (for this step, the MARCS flux was binned to match the
resolution of the data) to obtain the spectral transfer function. Finally, the science
flux was divided by the spectral transfer function so that it can be normalised.

Table 4.4: Wavelength offset from the telluric lines for each target and band observed in μm. The spectral resolution for the K band is $R \sim 4000$, for the L and M bands is $R \sim 500$, and for the N band it is $R \sim 1000$ for AH Sco and KW Sgr and $R \sim 30$ for the rest We did not include the KW Sgr offset in the K band because the information is not available in Arroyo-Torres et al. (2013).

Target	K (μm)	L/M (μm)	N (μm)
AH Sco	0.0003	0.0013	0.0135
KW Sgr	-	0.0002	0.0148
V602 Car	0.0006	0.0013	0.0403
CK Car	0.0006	0.0014	0.0403
V460 Car	0.0006	0.0013	0.0405

For KW Sgr, the requested K-band VLTI-GRAVITY data could not be obtained, and we used instead published VLTI/AMBER data for KW Sgr available in Arroyo-Torres et al. (2013). The data was taken using the AMBER medium-resolution mode R$\sim$1500 in the $K - 2.1\,\mu$m and $K - 2.3\,\mu$m bands. The reader is referred to Arroyo-Torres et al. (2013) for information about the data acquisition and reduction.

4.3 Methods

4.3.1 Model

The model is based on work by Davies and Plez (2021) and has been discussed in Davies and Plez (2021) and Chapter 3 of this thesis. Here we will briefly summarise the most important features, the reader is referred to Chapter 3 for an extensive discussion.

To a MARCS model atmosphere we plug in the effect of a stellar wind, using the mass continuity expression

$$\dot{M} = 4\pi r^2 \rho(r) v(r), \tag{4.1}$$

where ρ and v are the density and velocity as a function of the stellar radial coordinate r, respectively. The wind density $\rho_{\text{wind}}(r)$ has the following shape proposed by Harper et al. (2001):

$$\rho_{\text{wind}} = \frac{\rho_{\text{phot.}}}{(R_{\text{max}}/R_\star)^2} \left(1 - \left(\frac{0.998}{(R_{\text{max}}/R_\star)} \right)^\gamma \right)^\beta, \tag{4.2}$$

where $R_{\max}$ is the arbitrary outer-most radius of the model, in our case $\sim 8.5\,R_\star$.

The β and γ parameters define the smoothness of the extended wind region. We have performed the same analysis as in Chapter 3: using a grid with $-1.1 < \beta < -1.60$ in steps of $\Delta\beta = 0.25$ and $0.05 < \gamma < 0.45$ in steps of $\Delta\gamma = 0.2$. Our best fit parameters were found to be $\beta = -1.60$ and $\gamma = 0.05$ for all sources, which are consistent with the best fit from Chapter 3 (see Chapter 3 for a discussion of the best β and γ parameter determination). The velocity profile was found assuming a fiducial wind limit of $v_\infty = 25 \pm 5$ km/s, that is the value matched to Richards and Yates (1998); van Loon et al. (2005) and Beasor and Davies (2017), and Equation 4.1.

For the temperature profile, we assume the same two profiles as in Chapter 3, one following simple radiative equilibrium (R.E.) and another assuming a temperature inversion in the chromosphere of the star that peaks at $\sim 1.4\,R_\star$ and decreases again, following Harper et al. (2001). As in Chapter 3, the chromospheric temperature profile did not fit well the spectra and $|V|^2$ simultaneously, unlike R.E.. The reason is that this temperature inversion profile shows the CO lines in the region $2.3 < \lambda < 2.4\,\mu$m for the flux as emission lines. Since we do not observe any emission lines in the observations, we decided to use only the results based on R.E.. A fit with both profiles for AH Sco is shown in Appendix C for comparison. For more details, a full discussion about the different temperature profiles of the MARCS+wind model can be found in Chapter 3.

We re-sampled the temperature, density and velocity profiles to a constant logarithmic optical depth sampling $\Delta\log(\tau)$ (see the reasons for this re-sampling in Davies and Plez (2021) and Chapter 3). Finally, we defined the outer boundary of the model where the local temperature is < 800 K. Below this temperature, our code is unable to reliably converge the molecular equilibrium. In addition, some species would be depleted to dust grains. As a clarification, the $\tau_\lambda = 1$ surface is always within this radius if $\log \dot{M}/M_\odot \mathrm{yr}^{-1} < -4$.

4.3.2 Analysis

We computed the spectra and intensity profiles with respect to the radius of the star using the radiative transfer code TURBOSPECTRUM v19.1 (Plez, 2012). Setting a wavelength range from $1.8\,\mu$m to $5.0\,\mu$m with a step of $0.1\mathring{A}$ in order to

TABLE 4.5: The parameters for the MARCS models used for the analysis of each RSG. From left to right: Luminosity $\log L/L_\odot$, effective temperature T_{eff}, surface gravity $\log g$, metallicity [Z], microturbulence ξ, and mass as in Arroyo-Torres et al. (2013, 2015); Cruzalèbes et al. (2019). The last column shows the radius of the star in the photosphere in solar units (defined at $\tau_{\text{Ross}} = 2/3$).

RSG	$\log L/L_\odot$	T_{eff} (K)	$\log g$	[Z]	ξ (km/s)	$M/M_\odot$	$R_\star/R_\odot$
AH Sco	5.52	3600	-0.5	0	5	20	1411
KW Sgr	5.24	3700	0.0	0	5	20	1009
V602 Car	5.1	3400	-0.5	0	5	20	1015
CK Car	4.86	3500	0.0	0	5	15	690
V460 Car	4.46	3600	-0.5	0	5	15	539

resolve the microturbulence.

For the spectral synthesis, we included a list of atomic and molecular data[3]. Chemical equilibrium was solved for 92 atoms and their first two ions, including Fe, Ca, Si, and Ti, and molecular data for CO, TiO, H_2O, OH, CN, and SiO was included, among about 600 species.

The stellar parameters assumed in the MARCS model for the targets observed are shown in Table 4.5. The parameters were found in Arroyo-Torres et al. (2013, 2015) for AH Sco, KW Sgr and V602 Car and in Cruzalèbes et al. (2019) for CK Car and V460 Car. We used the MARCS model with the parameters from Table 4.5 as the initial model to plug in the stellar wind.

4.4 Results

We computed the visibilities with the same method as in Section 2.3 of Chapter 3. Briefly, we used the Hankel transform defined in Davis et al. (2000), estimated the angular diameter of the outermost layer of the model (θ_{Model}) using the relation with the Rosseland angular diameter θ_{Ross} found in Davis et al. (2000) and Wittkowski et al. (2004), and scaled the final model with an A factor that allows for the attribution of a fraction of the flux to an over-resolved circumstellar component (Arroyo-Torres et al., 2013). This A component depends on the wavelength range we are observing with.

---

[3]The atomic and molecular data is available at `https://github.com/bertrandplez/Turbospectrum2019`
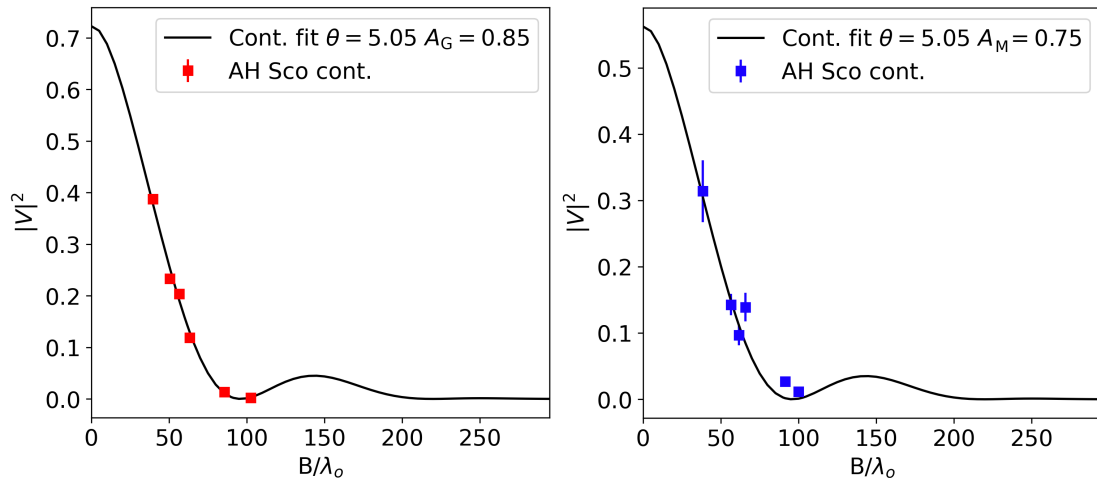
FIGURE 4.1: *Left panel:* Baseline with respect to the spatial frequency for the GRAVITY data accounting for the continuum, in red for the data points of AH Sco and in black the best fit model. *Right panel:* Same as the left panel but for MATISSE data.

To estimate both θ_{Ross} and A, for each studied model, we computed the $|V|^2$ as a function of their spatial frequency B/λ in the whole wavelength range of the K, L and M bands. We compared the model and data $|V|^2$ of both instruments, and found the best-fit θ_{Ross} and A by means of a χ^2 minimisation. For the case of KW Sgr, we used the AMBER data instead. We found the same best-fit A_L and A_M values for the L and M bands, while the best-fit A_K in the K band was different.

Table 4.6 shows the best fit for the θ_{Ross}, $A_{\mathrm{L/M}}$ and A_{K} of each RSG. The errors in θ_{Ross} and the A values were derived by the minimum values in the 68% dispersion contours of the χ^2 fit, which for 2 degrees of freedom corresponds to $\chi^2 < \chi^2_{\mathrm{min}} + 2.3$ (Avni, 1976). Our results are in agreement with Arroyo-Torres et al. (2013, 2015) within the error limits.

Figure 4.1 shows the baseline with respect to the angular frequency, for the best fit model accounting for the continuum in the GRAVITY and MATISSE data. This is the case for AH Sco, the rest of the targets produce similar plots. We see that in all cases the best model fits the data points well for the determined model θ. As expected, the A parameter changes depending on the instrument and wavelength range we are observing.

We used a range of mass-loss rates of $-7 < \log \dot{M}/M_\odot \mathrm{yr}^{-1} < -4$ with a grid spacing of $\Delta \log \dot{M}/M_\odot \mathrm{yr}^{-1} = 0.50$ to determine the best $\dot{M}$ fit. In the last

TABLE 4.6: From left to right: The best fit θ_{Ross} of the star, the A value for the K and L/M bands, respectively, and the $\log \dot{M}/M_\odot \mathrm{yr}^{-1}$ fit from the model. The fixed parameters of our model for all targets are the density profile parameters $\beta = -1.60$ and $\gamma = 0.05$, and simple R.E. for the temperature profile.

RSG	θ_{Ross} (mas)	$A_{\mathrm{L/M}}$	A_{K}	$\log \dot{M}/M_\odot \mathrm{yr}^{-1}$
AH Sco	5.05 ± 0.5	0.75 ± 0.05	0.85 ± 0.05	-4.0 ± 0.50
KW Sgr	3.00 ± 0.4	0.85 ± 0.05	0.9 ± 0.05	-4.5 ± 0.50
V602 Car	5.5 ± 0.5	0.85 ± 0.05	0.7 ± 0.05	-5.0 ± 0.50
CK Car	3.95 ± 0.5	1 ± 0.05	1 ± 0.05	-5.0 ± 0.50
V460 Car	3.05 ± 0.6	0.95 ± 0.05	0.95 ± 0.05	-6.5 ± 0.50

column of Table 4.6 we also show the best fit $\log \dot{M}/M_\odot \mathrm{yr}^{-1}$ for our static wind model and the errors corresponding to the grid spacing.

When checking the $\log \dot{M}/M_\odot \mathrm{yr}^{-1}$ column in Table 4.6, we see that our best fit mass-loss rate is in accordance with typical mass-loss prescriptions (e.g., de Jager et al., 1988; Schröder and Cuntz, 2005). As the stars become more luminous, the $\dot{M}$ becomes very high compared to recent prescriptions (e.g., Beasor et al., 2020), which is the case of AH Sco and KW Sgr. This could mean that our model has still some limitations. Even though we have checked that we are not hitting the edge of our grid models, it could be that the temperature or density profiles are still not optimum. Another reason for this high $\dot{M}$ would be that since the pure MARCS model is very compact, we could need an unrealistically higher $\dot{M}$ to reproduce the observations.

Figure 4.2 shows a 2D intensity plot for the model of AH Sco and the different wavelengths showing water, continuum, CO and SiO. We see that, while the continuum seems to be mainly present at $R = 1\,R_\star$, the rest of the molecules are present at extended layers: water near the photosphere $R \sim 1.001\,R_\star$, as seen in Chapter 3, while CO and SiO at $R > 1\,R_\star$.

4.4.1 GRAVITY

Figures 4.3, 4.4, 4.5 and 4.6 show the reduced data for the K band, the best-fit MARCS+wind model for the temperature profile of R.E. and the initial best pure MARCS model fit for AH Sco, V602 Car, CK Car and V460 Car, respectively. We include every baseline of the observations. Our R.E. model reproduces better both the fluxes and $|V|^2$ than the pure MARCS model.
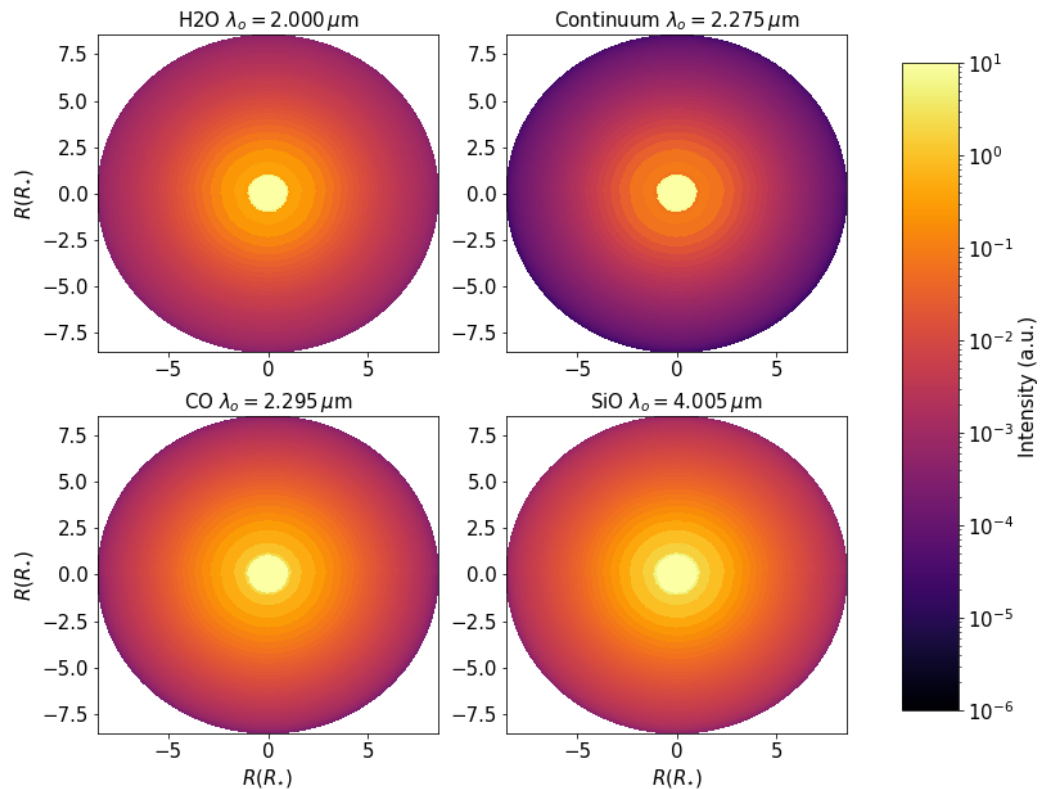
FIGURE 4.2: 2D plot showing the intensity of the water, continuum, CO and
SiO regions for our extended model of AH Sco.

The most important features that our model can reproduce in this wavelength range are the CO absorption lines in $\lambda = 2.29 - 2.7\,\mu$m as well as the water signatures at $\lambda = 1.8 - 2.2\,\mu$m and at the edge of the band $\lambda > 2.35\,\mu$m. These features are presented as a broader shape in the absorption lines in the flux as well as the $|V|^2$. We see that for all the cases, while the pure MARCS model matches our model and the data in the spectra, the $|V|^2$ extensions for the different baselines are substantially better reproduced by our model as compared to pure MARCS. While MARCS seems to be able to show only some faint CO features in the $|V|^2$, our model can match better the shapes in the whole $|V|^2$ for all the studied targets. This means that the layers where the CO lines are formed are more extended than in the MARCS models.
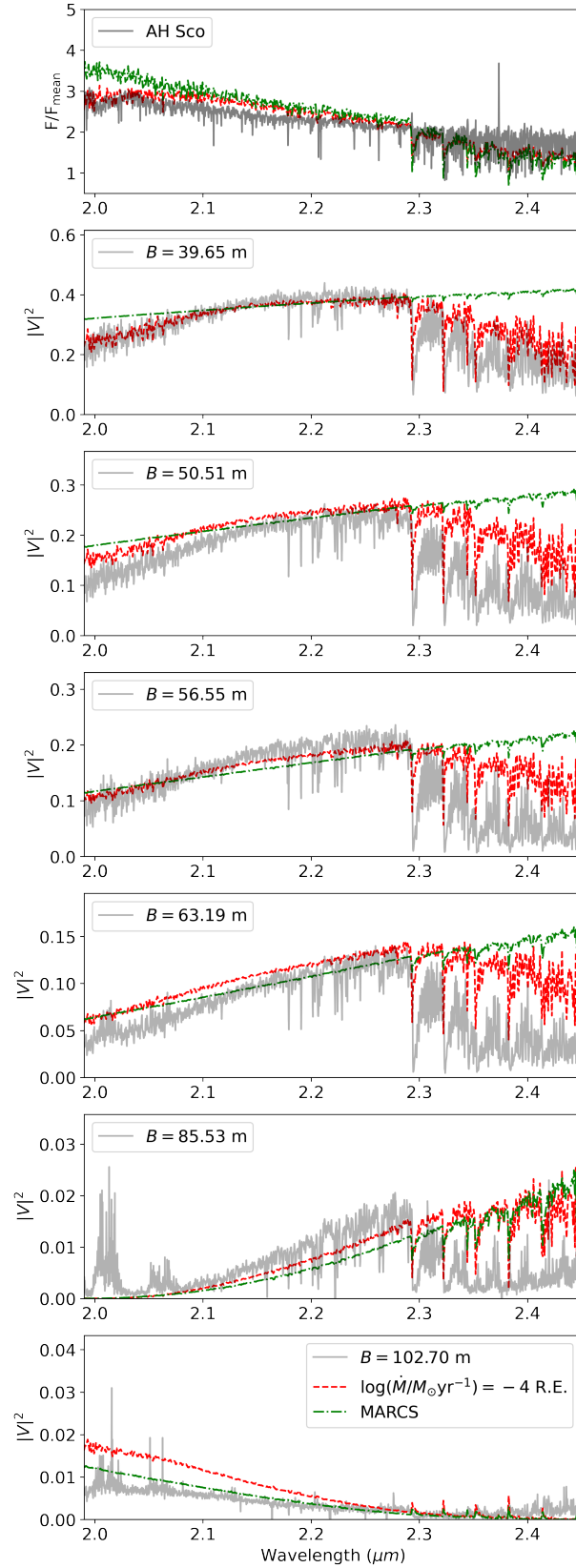
FIGURE 4.3: *Upper panel:* Normalised flux for the RSG AH Sco (grey), as observed with VLTI/GRAVITY for the K band. Our best-fit model is shown in red for R.E., while the pure MARCS model fit is shown in green. *Lower panels:* Same as the upper panel but for the $|V|^2$ with different baselines. Both flux and $|V|^2$ are better represented by our fit.
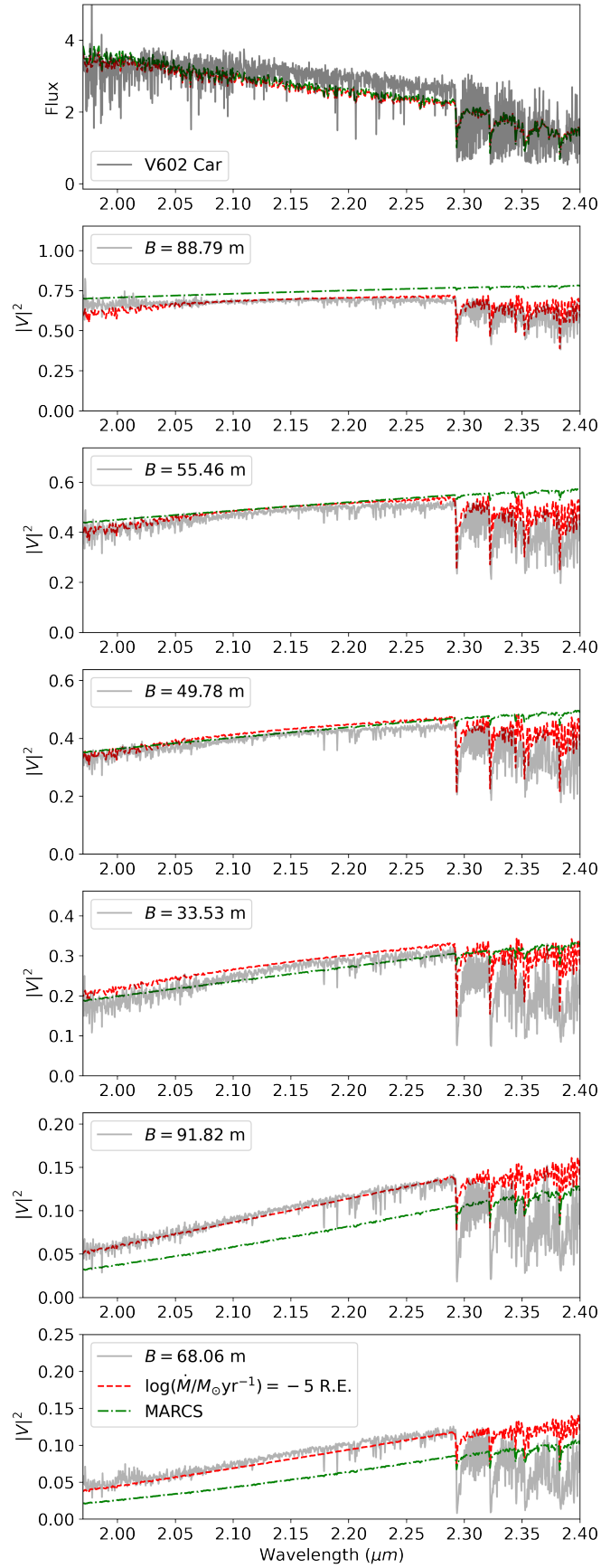
Figure 4.4: Same as Figure 4.3 but for V602 Car.
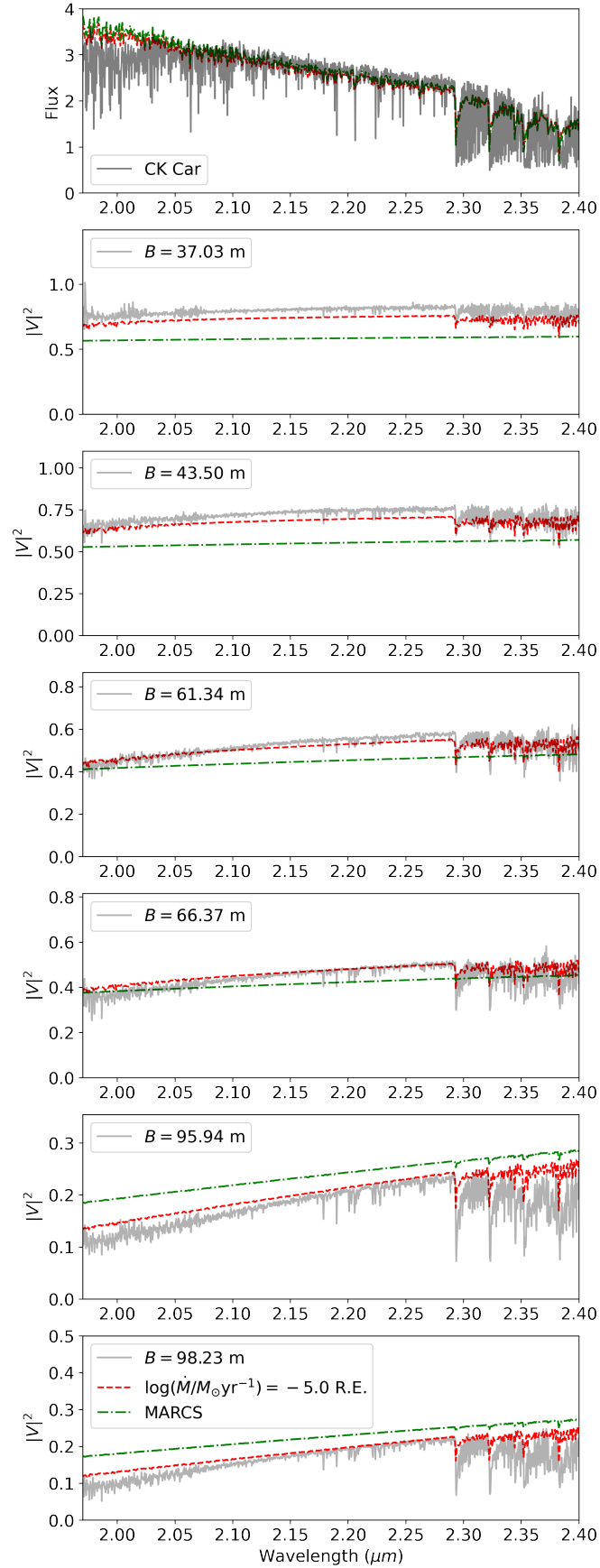
FIGURE 4.5: Same as Figure 4.3 but for CK Car.
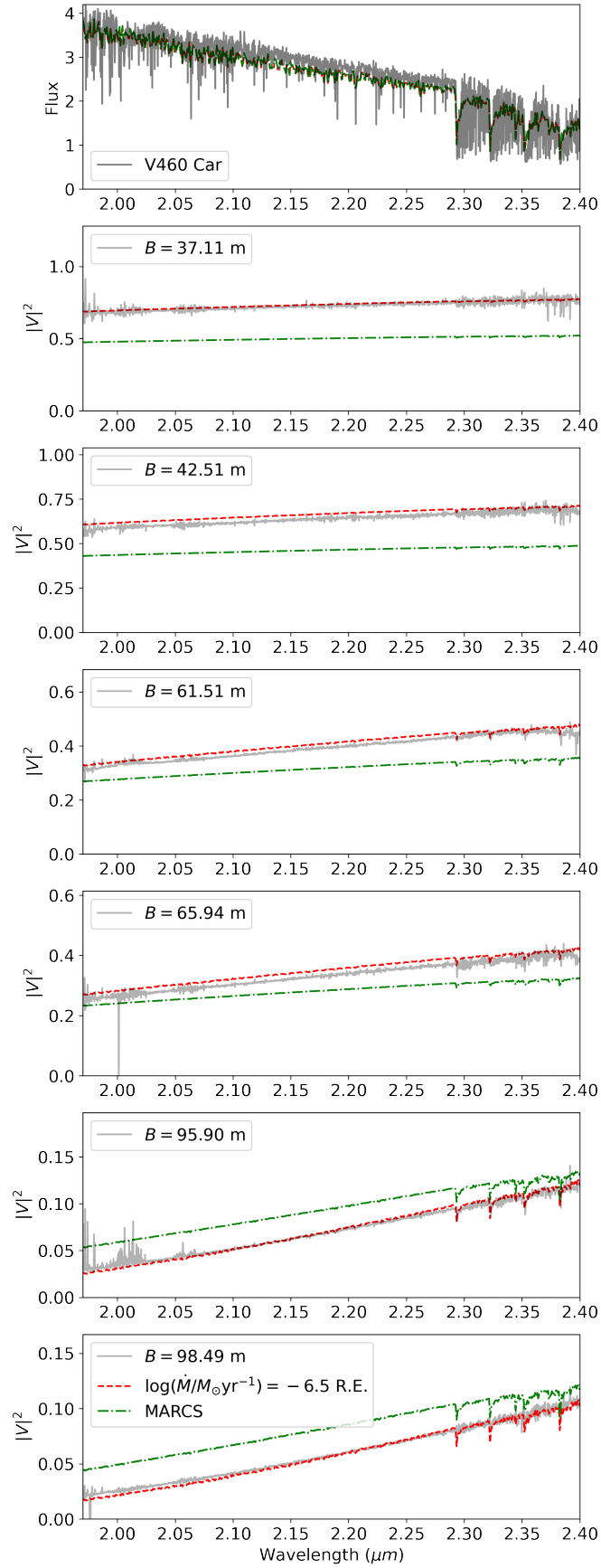
Figure 4.6: Same as Figure 4.3 but for V460 Car.

4.4.2 MATISSE

Figures 4.7, 4.8, 4.9, 4.10 and 4.11 show the MATISSE reduced data for the L and M bands, the best fit MARCS+wind model for the temperature profiles with R.E. and the initial best pure MARCS model fit for AH Sco, KW Sgr, V602 Car, CK Car and V460 Car, respectively. Our model reproduces better both the fluxes and $|V|^2$ than the pure MARCS model.

The most important feature that our model can reproduce in the L band is the SiO absorption line at $\lambda = 4.0\,\mu$m. Our model matches better the spectra than compared to MARCS at $\lambda > 4.0\,\mu$m, specifically for AH Sco (Figure 4.3), where the SiO features an increase in the flux that MARCS does not reproduce. Regarding the $|V|^2$ extensions for the different baselines, pure MARCS does not reproduce at all the extension in SiO, while our model can fit the data and reproduce the SiO feature. This is the first time that a model can reproduce the extension in SiO using MATISSE spectro-interferometry data of RSGs.

As for the M band, the visibilities are clearly lower than predicted by pure MARCS and better consistent with our model. This is due to the presence of CO in this band (see Chapter 3 for an extended discussion). In this band, R.E. and the chromospheric temperature profile have strong differences, where the chromospheric temperature profile shows CO in emission in this wavelength region. Four our targets, R.E. still reproduces better this wavelength region.

The reduced MATISSE N band data is shown in Appendix D. It has not been analysed since that wavelength region is highly affected by dust, and therefore cannot be matched to our model.

4.4.3 AMBER

Figure 4.12 shows the published AMBER data in the K band by Arroyo-Torres et al. (2013), the best fit MARCS+wind model and the initial best pure MARCS, since we did not have GRAVITY data for KW Sgr.

In Figure 4.12, the extension in the CO lines ($\lambda > 2.3\,\mu$m) appears to be under-represented, while the same model fits better the MATISSE data (Figure 4.8). As mentioned in Chapter 3, a possible explanation for this mismatch could be that for increasing $\dot{M}$, the models still fail to reproduce the extension of the water or CO
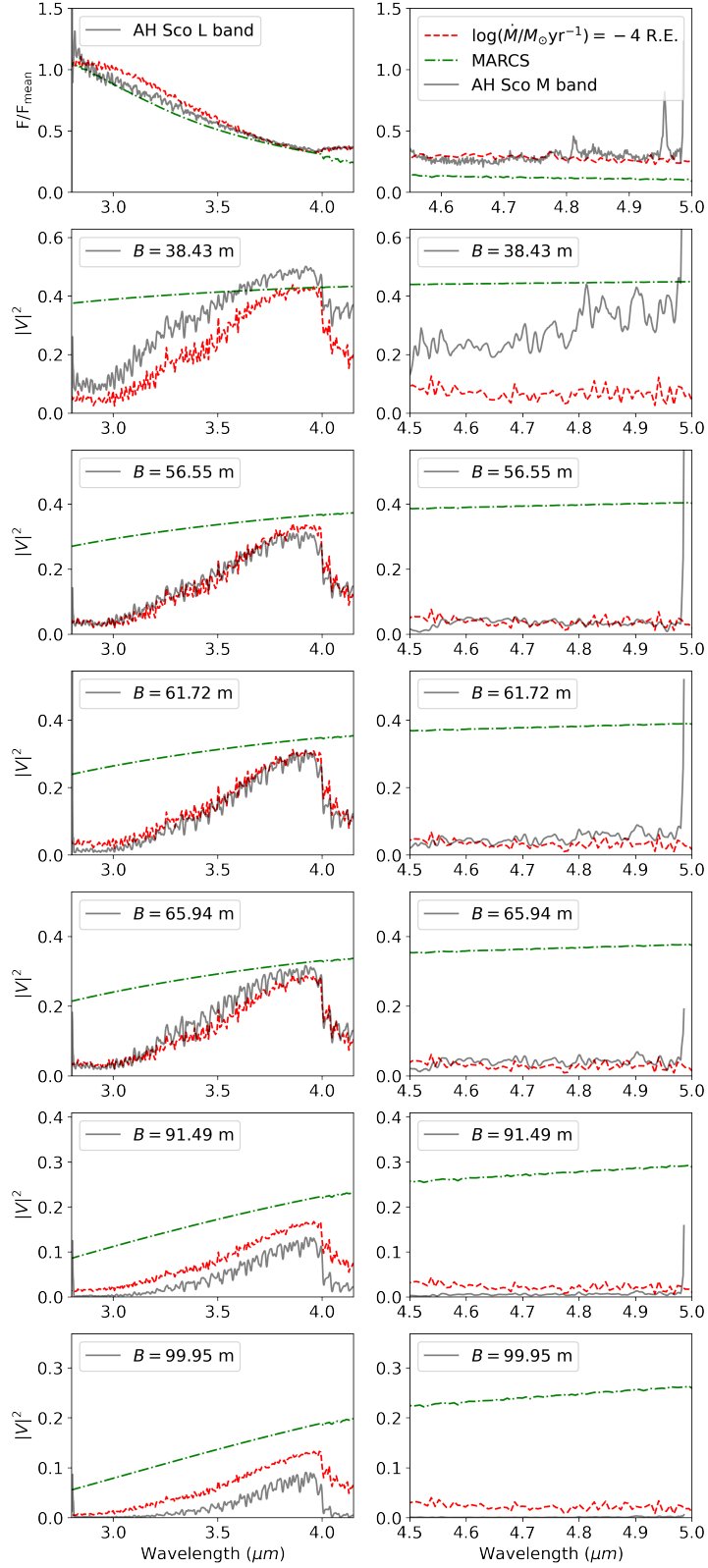
FIGURE 4.7: *Upper panel:* Normalised flux for the RSG AH Sco (grey), as observed with VLTI/MATISSE for the *L* (*left panels*) and *M* bands (*right panels*). Our best-fit model is shown in red, while the pure MARCS model fit is shown in green. *Lower panels:* Same as the upper panel but for the $|V|^2$ with different baselines. Both flux and $|V|^2$ are better represented by our fit.
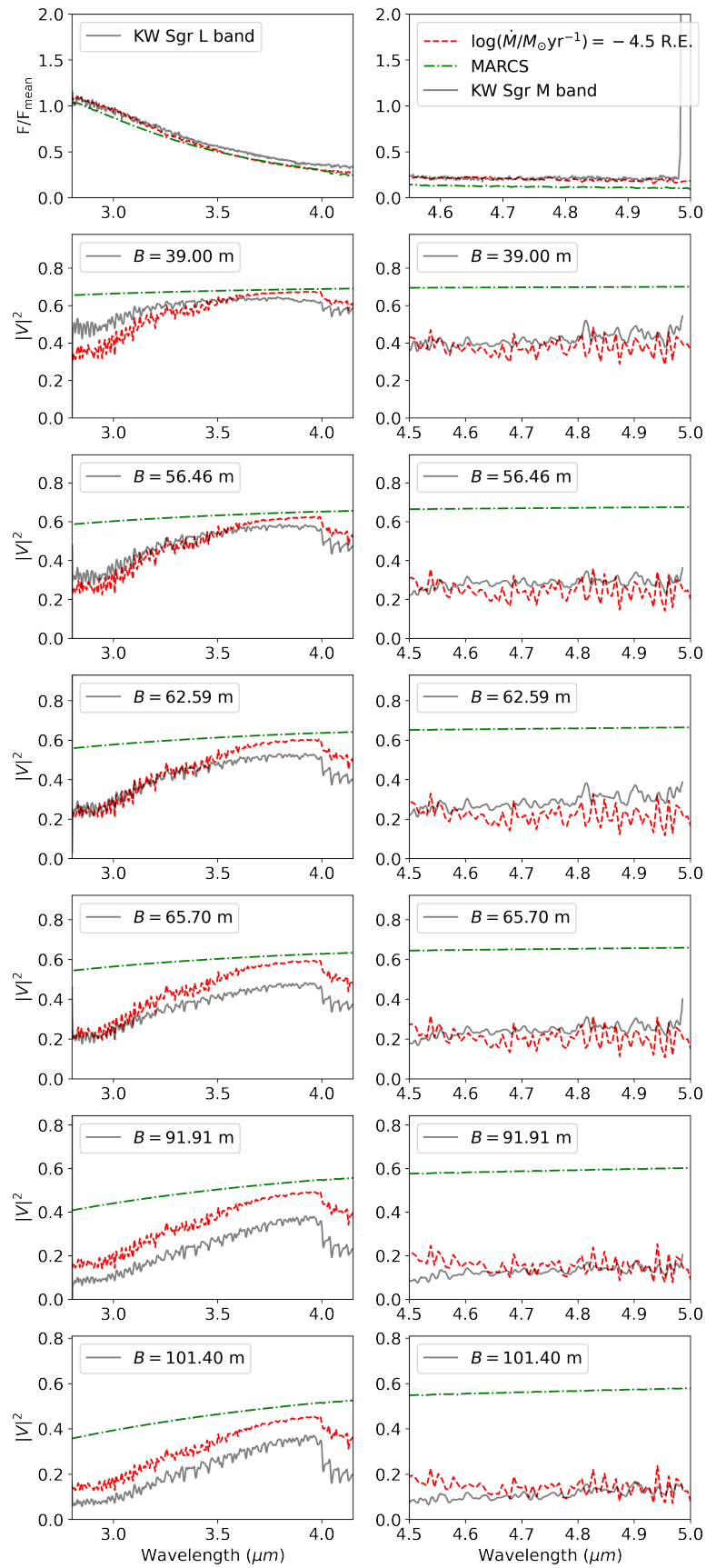
FIGURE 4.8: Same as Figure 4.7 but for KW Sgr.
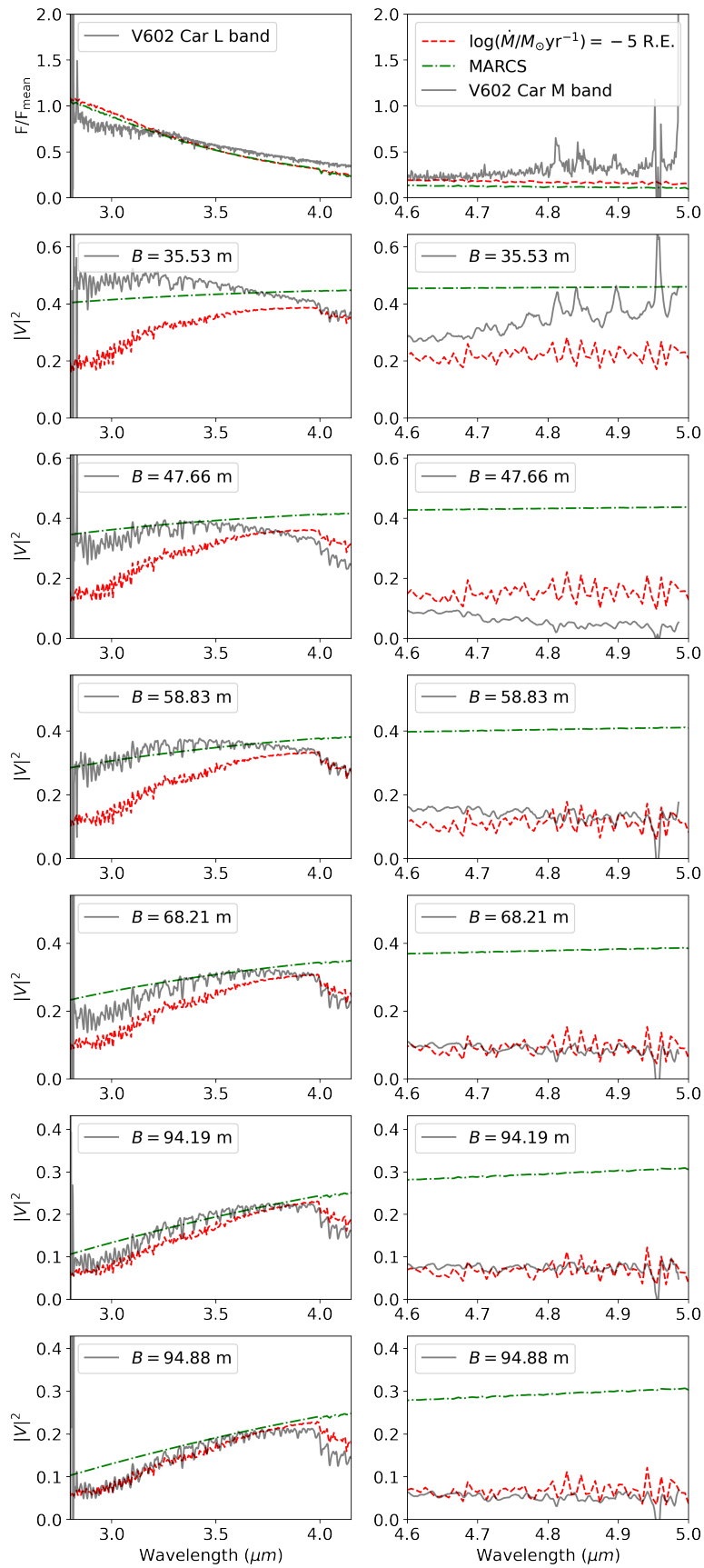
Figure 4.9: Same as Figure 4.7 but for V602 Car.
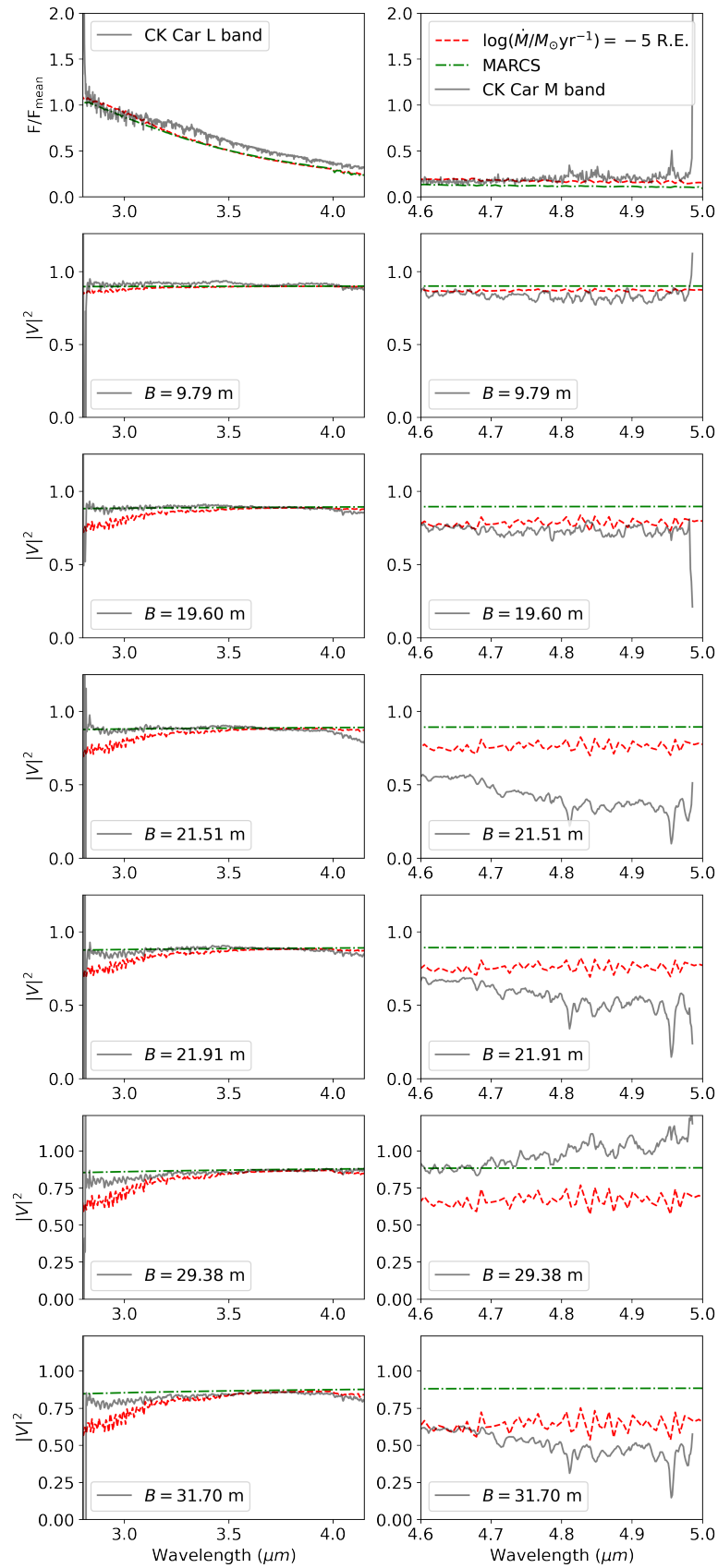
Figure 4.10: Same as Figure 4.7 but for CK Car.
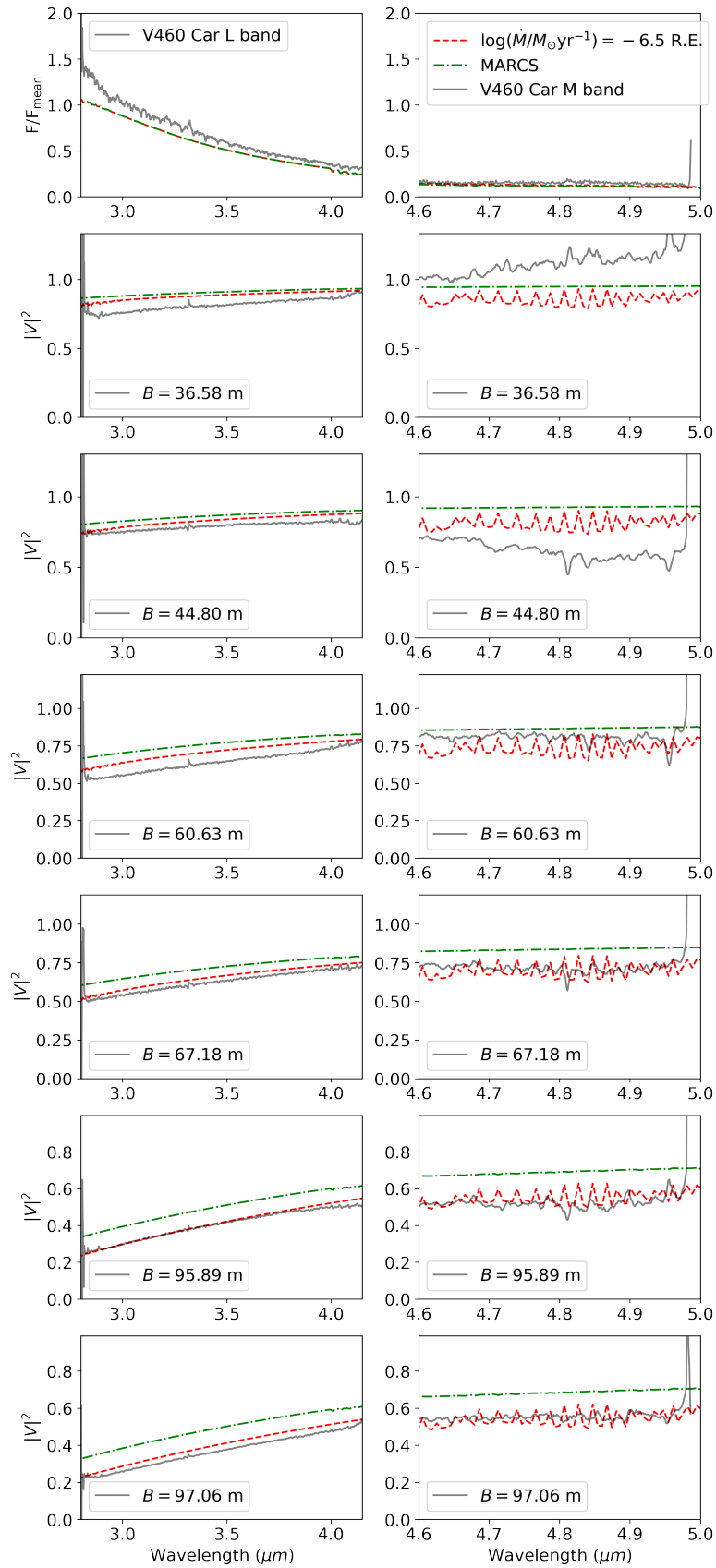
FIGURE 4.11: Same as Figure 4.7 but for V460 Car.
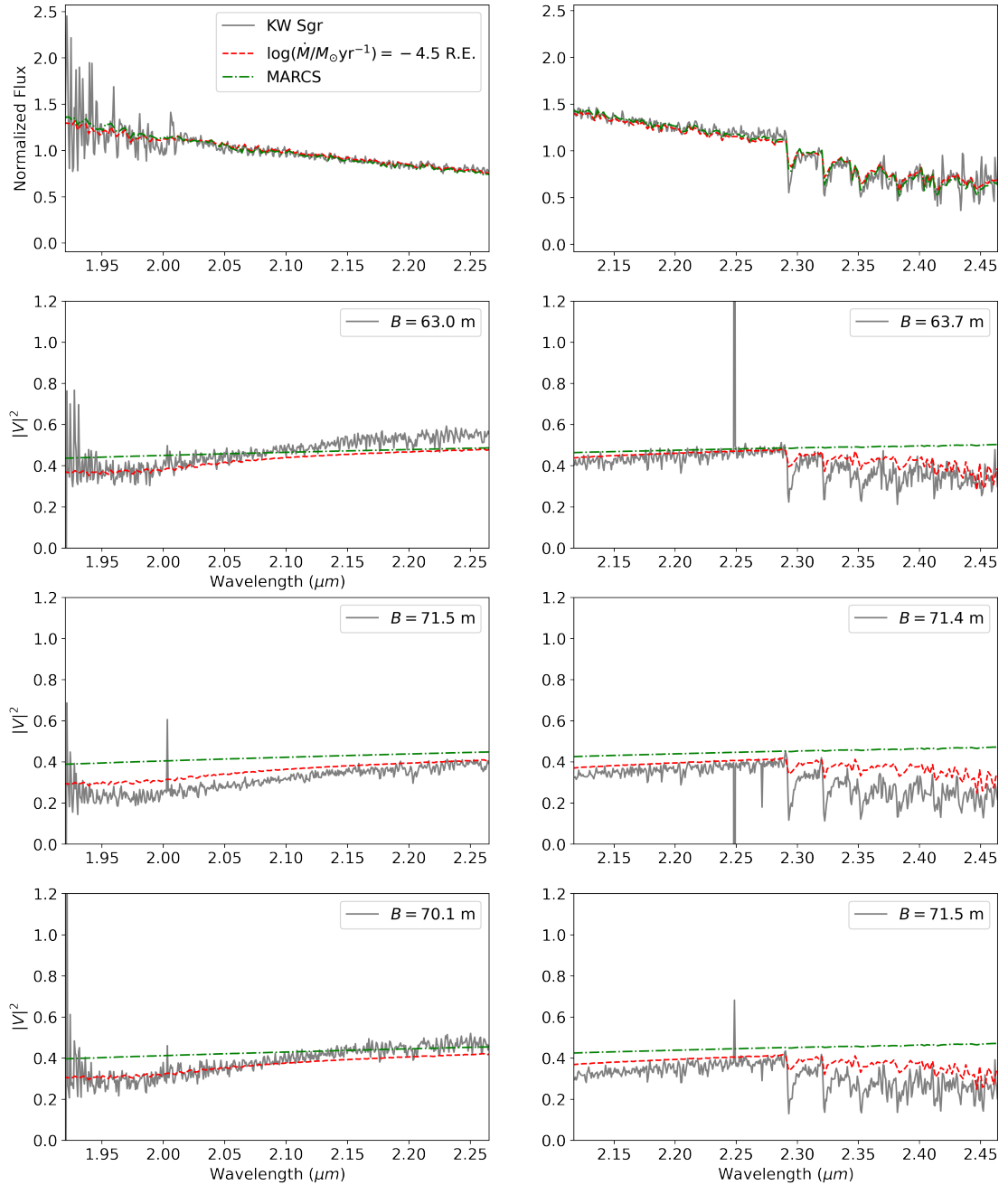
FIGURE 4.12: *Upper left:* Normalised flux for the RSG KW Sgr (grey), as observed with VLT/AMBER for the $K - 2.1\,\mu$m bands. Our best-fit model is shown in red while the pure MARCS model fit is shown in green. As expected, the fluxes are well represented by both our fit and MARCS. *Upper right:* Same as the upper left panel, but for the $K - 2.3\,\mu$m band. *Lower left:* Same as the upper left panel, but for the $|V|^2$ with the different baselines. *Lower right:* Same as the lower right panel, but for the $K - 2.3\,\mu$m band and different baselines. Our model can represent the data better than pure MARCS.
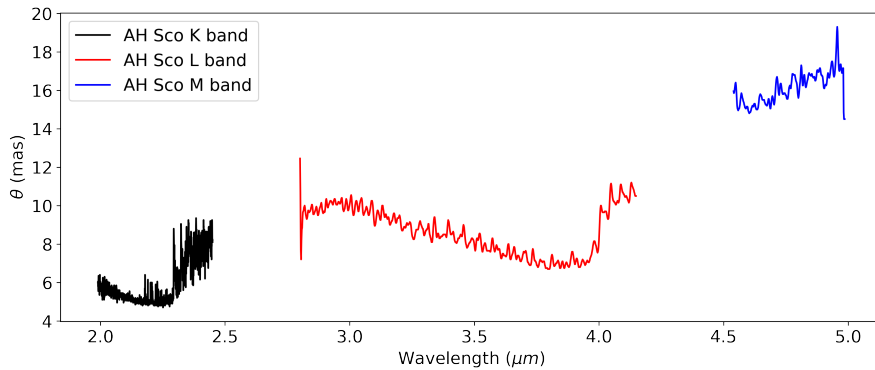
FIGURE 4.13: Results for the uniform disk (UD) model fit using the AH Sco data in the K, L and M bands.

layers. In addition, since our model neglects velocity gradients, it underestimates the equivalent widths of lines which would help to increase the apparent stellar extension at those wavelengths.

4.4.4   Uniform Disk model

In order to illustrate the apparent size of the star as a function of wavelength across the K, L and M bands, we also describe our data with one of the most simple models to describe the photospheric emission of a star: the uniform disk (UD) model. The intensity of the uniform disk model, I_{UD} is described as:

$$I_{\mathrm{UD}}(\rho) = \begin{cases} 4/(\pi\theta^2) & \text{if } \rho \leq \theta/2 \\ 0 & \text{if } \rho > \theta/2 \end{cases} \tag{4.3}$$

where ρ and θ are the polar coordinates in the object plane (Berger and Segransan, 2007). Assuming a fixed A and following Equation 4.3, we can obtain a best fit angular diameter θ for each wavelength. Figure 4.13 shows the best UD θ fit for each one of the K, L and M bands.We see that for each individual band, θ increases for specific wavelengths where molecules are present (e.g., θ increases at the CO lines in $\lambda > 2.3\,\mu$m or there is a big increase in $\lambda = 4.0\,\mu$m due to SiO). This indicates that these molecules are formed in the extended atmospheric region.

The simple UD model already illustrates the extended atmosphere of RSGs over a large wavelength range from $1.8 < \lambda < 5.0\,\mu$m, but with our MARCS+wind model we are able to accurately reproduce this extension for the first time.

4.5 Discussion

After finding the optimised model for each of the targets, the profiles are consistent with the characteristics as in Chapter 3 (i.e. simple R.E. for the temperature and a density profile with $\beta = -1.60$ and $\gamma = 0.05$). Moreover, we see that both a single density and temperature profile fits well both GRAVITY and MATISSE observations simultaneously, as well as the AMBER observation to a certain extent.

4.5.1 Formation of SiO

SiO is one of the most important molecules in the atmosphere and circumstellar envelope of evolved cool massive stars, as it is a precursor of silicate dust formation. MARCS models alone cannot explain the presence of SiO lines in cooler red giants and RSGs even when taking into account the dust emission. This means that the SiO is formed in the extended molecular atmosphere (Ohnaka, 2014).

Mapping the extended molecular atmosphere where the SiO is present is important to understand the mass-loss mechanisms in cool evolved stars. Indeed, the wind acceleration takes place in the region between the photosphere and the inner region of the circumestellar envelope. Some attempts to understand the dust formation processes and to map the circumstellar environment in cool evolved stars include the ATOMIUM project using ALMA (Gottlieb et al., 2022) or more recently, VLT/SPHERE observations (Montargès et al., 2023).

Our work focuses on the region where the wind is accelerated. SiO is the strongest feature of our L band MATISSE data. Therefore, we can study the presence and formation of SiO in this extended atmospheric region. Figure 4.14 shows the intensity at the SiO line ($\lambda = 4\,\mu$m) minus the intensity at the near continuum ($\lambda \sim 3.8\,\mu$m) with respect to the radius of the star for the best-fit models of our targets. We see that the SiO formation depends on the luminosity used for our model, since each of the RSGs represented have a different luminosity as seen in Table 4.5. As the luminosity increases, the formation shifts to higher $R_\star$. In any case, the SiO production starts at a $R > 2.5\,R_\star$, which means that the production of SiO starts way beneath we reach the maximum extension of our model ($R \sim 8.5\,R_\star$). In this case, the temperature formation of dust silicates and the depletion of SiO would be at $T > 800$ K. According to the model temperature
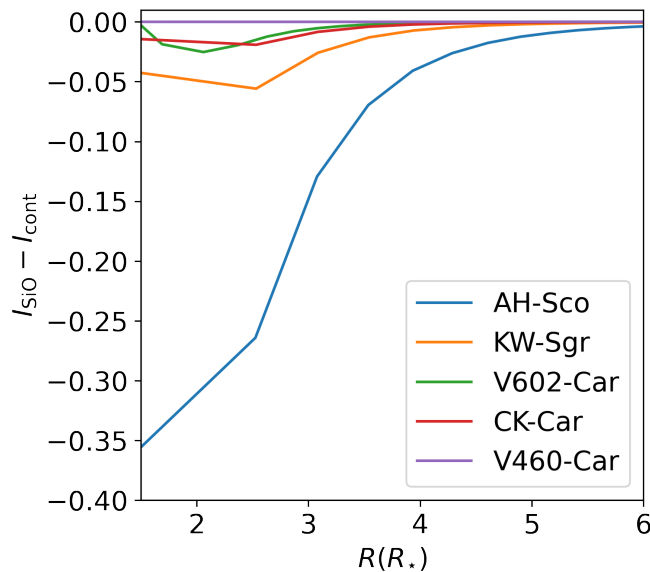
FIGURE 4.14: Intensity at the SiO line minus the continuum with respect to radius of the star for the case of R.E. for each different best fit model corresponding to the RSG studied.

profile it will indicate a temperature of the order of $T \sim 1500$K, which is in accordance with previous work by Gail et al. (2020). It could be also possible that SiO and dust silicates co-exist, as dust production may not be completely efficient.

4.6 Summary and conclusion

We used the 1D modelling approach to add a wind to a pure MARCS model as in Davies and Plez (2021) and Chapter 3 to compare with new MATISSE and GRAVITY data of five RSGs. Aside from obtaining the CO and water lines with the GRAVITY data, the MATISSE data adds the SiO line at $\lambda = 4\,\mu$m and additional CO transitions in the M band. After comparing the synthetic interferometric visibility and synthetic flux spectra to the data, we see that our models can reproduce better the $|V|^2$ for the observations in all baselines as compared to pure MARCS. We fit simultaneously the MATISSE and GRAVITY wavelength coverage. Therefore, we are able to reproduce extensions for the first time in the L and M bands, and can also reproduce again the extensions for the K band as in Chapter 3.

Our best-fit mass-loss rate increases as the star becomes more luminous. The density and temperature stratification profiles of our model are in accordance

with the profiles found in Chapter 3: simple R. E. for the temperature profile and a steeper density profile with smoothness parameters of $\beta = -1.60$ and $\gamma = 0.05$ (as defined in Equation 4.2). In addition, the formation of SiO occurs at $R \sim 2\,R_\star$, where the temperature is to the order of $T \sim 1500$K.

This is one of the first studies of RSGs using the MATISSE instrument after Chiavassa et al. (2022). Moreover, Chiavassa et al. (2022) used low spectral resolution, while we obtain the data with medium spectral resolution. Complementing with GRAVITY observations in the K band, we have obtained some of the most complete spectro-interferometric data up to date of RSGs, covering the wavelength range of $1.8 < \lambda < 13\,\mu$m.

To conclude, this chapter shows the potential of the simple 1D MARCS+wind model to fit several spectral bands, providing accurate extensions for the first time in the $|V|^2$. This model approach could be adapted to other lower and intermediate-mass stars such as Miras. In the future, we would like to compare this result with recent 3D extended models (e.g., Ahmad et al., 2023).

Chapter 5

Conclusions and Future work

This chapter presents a short summary of my work along with the main takeaways and future prospects.

5.1 Red supergiants in low metallicity environments

Evolutionary models predict a metallicity (Z) dependence on the Hayashi limit. This limit dictates the minimum effective temperature (T_{eff}) a star can have when still maintaining hydrostatic equilibrium. When comparing with observations, if this Z-dependence is not the same as model predictions, it implies that the assumptions used to simulate convection are not correct (e.g., mixing length theory). This means that there should be a Z-dependence with the mixing length parameter instead, which would be important for all studies of stellar physics and all astronomy that relies on it. We analysed VLT/X-SHOOTER spectroscopic data of RSGs in different Z environments (the Magellanic clouds and the metal poor galaxy Wolf-Lundmark Mellotte, WLM). We compared my results to those from population synthesis, based on model predictions from evolutionary tracks. We found that our Z trend with respect to the temperatures of RSGs leads to discrepancies with current evolutionary models. These important results show *that the mixing length parameter in current massive evolutionary models has to be re-evaluated.*

97

5.2 Spatially extended atmospheres of red supergiants

We applied a semi-empirical model to describe the extended atmospheres of RSGs using optical interferometric data from the ESO Very Large Telescope Interferometer (VLTI) instruments AMBER, MATISSE and GRAVITY. The model is based on a combination of simple MARCS models and adding a semi-analytic description of a stellar wind with a constant $\dot{M}$ (Davies and Plez, 2021).

After defining the stellar structure model, we used the radiative transfer code TURBOSPECTRUM (Plez, 2012) to obtain fluxes and intensities with respect to the line of sight angle for different wavelength ranges. With these intensities, we could compute the squared visibility amplitudes ($|V|^2$). The $|V|^2$ in molecular bands are tightly co-related with $\dot{M}$, for a higher $\dot{M}$ we obtain stronger $|V|^2$ features. Therefore, by studying the changes on both $|V|^2$ and flux simultaneously we can better fit the $\dot{M}$ of our model. With the optical interferometric data in the K band ($1.8\,\mu\text{m} < \lambda < 2.5\,\mu\text{m}$), we compared the $|V|^2$ and spectral fluxes from different RSGs and my model predictions, to obtain the best estimations for the $\dot{M}$, the temperature and density profiles of the stellar wind. Our model not only reproduces the intensity profiles, but it can also accurately reproduce for the first time the drop of $|V|^2$ in molecular lines of water and CO. *This work has been able to reproduce for the first time the spatial extension of the atmosphere of RSGs.* These results have a big impact in massive stellar astrophysics and all astronomy dependent on them, providing for the first time accurate empirical structure stratification profiles of evolved massive stars.

5.3 Further modelling with VLTI/GRAVITY and MATISSE data

We obtained, reduced and analysed new data of RSGs in the Milky Way using the VLTI/GRAVITY and MATISSE instruments, comprising the K, L, M and N bands ($1.8\,\mu\text{m} < \lambda < 13\,\mu\text{m}$). Using this extended wavelength range in new targets, we were able to reproduce for the first time the drop of $|V|^2$ in molecular lines of not only water and CO, but also SiO. Aside from being one of the only

studies to date that uses MATISSE to observe the atmospheric structure of RSGs, it also represents *one of the most complete spectro-interferometric data coverage of RSGs up to date.*

Comparing the data of a broader wavelength range to our modelling approach allowed us to corroborate the potential of our extended models. The analysis also produced for the first time angular diameter determinations, temperature and density stratifications for the new targets.

Even though the $\dot{M}$ obtained are very high compared to current prescriptions (e.g., Beasor et al., 2020), we speculate that a possible reason for this high $\dot{M}$ would be that since the pure MARCS model is very compact, we could need a higher $\dot{M}$ to reproduce the same extensions observed. For future work, we would compare with averaged 3D hydrodynamical models (e.g., Chiavassa et al., 2009, 2010, 2011b,a) to our current models. Despite the 3D models not being extended enough for RSGs yet, comparing with 3D averaged models of Mira stars we can already see that the $\dot{M}$ needed to reproduce the same $|V|^2$ is lower. This is because the models are not as compact as MARCS.

Finally, our models show that the formation of SiO occurs at a $T \sim 1500K$, before the dust shell appearance. There is also a dependence on the formation of the SiO and the luminosity of our model, in a way that higher luminosities produce a steeper formation of SiO at a slightly higher radius.

5.4 Future work: a new mass loss rate prescription

Evolutionary codes predict that massive stars from 8 to $25 - 30\,M_\odot$ will evolve all the way to the RSG stage, core-collapsing in a H-rich SN type II-P (Choi et al., 2016). However, when compared to observations, the upper limit to the mass range for SN II-P progenitors is found to be $\sim 17\,M_\odot$ instead. This mass discrepancy is the so-called *RSG problem* (Smartt, 2009). A possible solution includes increasing the mass-loss rates ($\dot{M}$) to lower the mass where the H-envelope is shred, but there is no consensus whether a high $\dot{M}$ can occur or not. If the RSG shreds its H-envelope, it could become a hot stripped progenitor, moving away from the RSG stage and exploding as a different type of SN (H-poor, type I). Therefore,

mass loss dictates the final fate of massive stars: it determines whether they will produce a SN at all, and if so, which type (i.e. H-rich/H-poor). Mass loss is then crucial to develop accurate stellar evolutionary tracks, obtaining the correct stellar structure models and upper mass limits for SN progenitors.

Despite its importance, the physical processes that trigger mass loss in the atmospheres of RSGs are still not fully understood, and remain one of the key questions in stellar astrophysics. As a consequence, their $\dot{M}$ can not be derived from first principles. The current $\dot{M}$ prescriptions are based purely on observations. The most commonly used $\dot{M}$ prescription for RSGs (de Jager et al., 1988) is more than 30 years old and based on a small sample of archival observations (< 10 stars). Other $\dot{M}$ prescription attempts focus on $\dot{M}$ biased towards the mid-IR (e.g., van Loon et al., 2005; Goldman et al., 2017). Recently, Beasor et al. (2021a) developed a $\dot{M}$ prescription studying RSGs dust excess in stellar clusters, finding not only a $\dot{M}$ relation with luminosity (L), but also with the initial stellar mass (M_{init}). Beasor et al. (2021a) found out that the previous prescriptions over-estimate $\dot{M}$ by up to a factor of 20, and in consequence that the $\dot{M}$ in the RSGs phase are not effective at removing their H-rich envelope prior to core-collapse. These controversial claims imply that single star evolution is irrelevant for massive stars.Therefore, the only way to obtain core-collapse SN type Ib/c would be through binary evolution, since the mass lost in the single RSG phase by winds seems to be insignificant. However, these findings suffer from substantial systematic errors in getting $\dot{M}$ from dust (e.g., gas to dust ratio, composition).

In this thesis, the improved stellar atmospheric models introduced have the potential to retrieve $\dot{M}$ from RSG spectra that are free of the systematics described above. We measure the $\dot{M}$ at a smaller radii than the dust region thanks to the high angular resolution of interferometry.

With my current spectro-interferometric data, by studying the changes on both $|V|^2$ and flux simultaneously, we can better fit the $\dot{M}$ of our model. Once benchmarked the models using both flux and $|V|^2$, we can obtain an $\dot{M}$ by fitting the spectra alone. In Chapter 3, we see that our synthetic spectra also shows differences when comparing to pure MARCS, so with the bench-marked models, the spectral features would be enough to determine $\dot{M}$. Then, we will be able to measure $\dot{M}$ from optical and near-IR spectra alone by using e.g., Gaia (Gaia Collaboration et al., 2018), X-Shooter (Vernet et al., 2011) or CRIRES (Kaeufl et al., 2004) observations.

By using this independent $\dot{M}$ determination, we can compare with the predictions from previous mass-loss prescriptions to determine whether the $\dot{M}$ are high enough to allow the SN progenitor to shred its H-envelope.

Ultimately, we will produce a *new $\dot{M}$ prescription based on optical, near- and mid-IR spectra*. With my newly measured stellar information, we can obtain new evolutionary tracks with the stellar code MESA (Paxton et al., 2011).

Finally, we propose to add the dust contribution to our model by studying the N band data of my VLTI/MATISSE observations. This N band wavelength region ($8\,\mu\text{m} < \lambda < 13\,\mu\text{m}$) is largely affected by dust. Our initial model does not include the dust contribution, since it is expected to have little to no effect at $T_{\text{eff}} > 800$ K, so $R < 8R_\star$ (Gail et al., 2020). To obtain a complete picture for the full stellar atmospheric description of RSGs, we need to add the contribution of the dust produced at $T_{\text{eff}} < 800$ K. This means including the dusty shell contribution in addition to our MARCS+wind model. By comparing with the heavily dust affected N band, we would be able to *obtain for the first time a complete picture of the stellar structure model of RSGs*. This stellar structure model will allow us to improve the previous $\dot{M}$ prescriptions based on dust excess (e.g., de Jager et al., 1988; Beasor et al., 2021a).

To sum up, the future work outcomes include: a new $\dot{M}$ prescription independent from dust, new MESA evolutionary tracks, production of grids for the most complete stellar atmospheric model of RSGs, and the prediction of many observed properties including the rates for H-rich/poor single star SN, and surface abundances prior to SN.

Appendix A

Statistical significance test
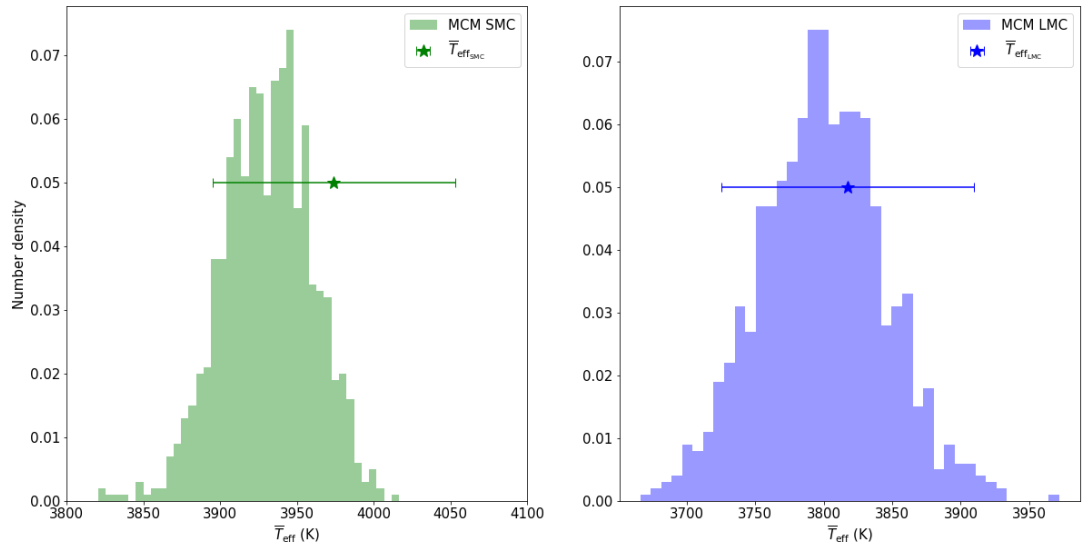
FIGURE A.1: Two panels showing the results for the statistical significance of our sample in the MCs. *Left:* Shows the histogram produced from the Monte-Carlo like simulation of the SMC sub-sample stars from Tabernero et al. (2018) with the same spectral type as our sub-sample, an the average T_{eff} for the full sample of Tabernero et al. (2018). *Right:* The same as *left* but for the LMC.

Appendix B

Analysis of RSGs
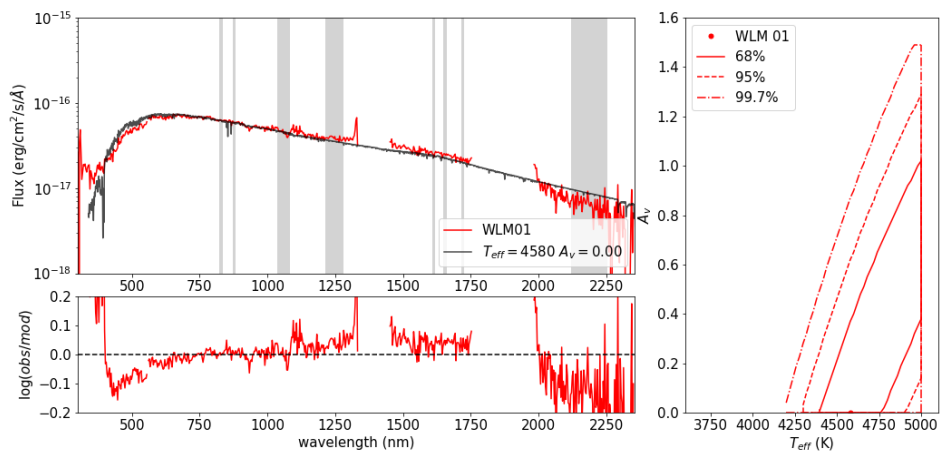
FIGURE B.1: Three panels showing the results of the analysis for WLM 01. *Upper left:* Shows the smoothed data (red) and best fitted MARCS model (black), while the SED regions for the analysis are shown in gray. *Lower left:* The residuals of the fit. *Right:* shows the 68%, 95% and 99.7% confidence contours for the best fitted effective temperature and extinction.
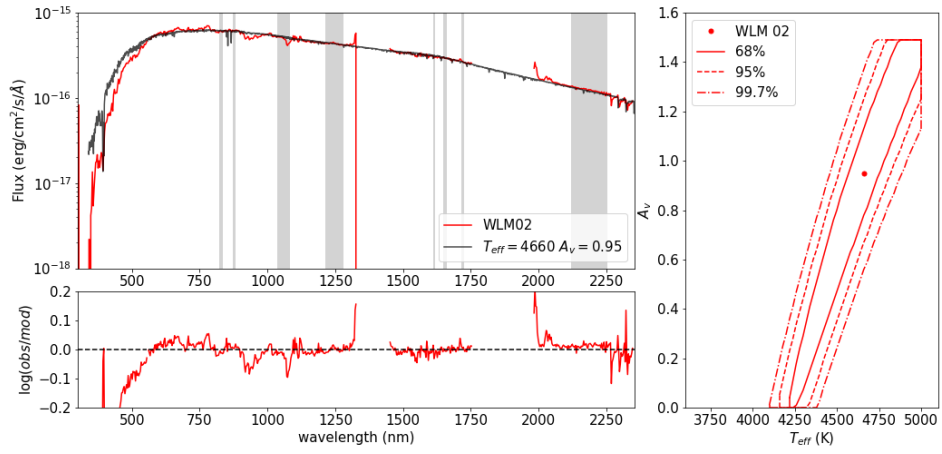
FIGURE B.2: Same as Fig. B.1 but for WLM 02.
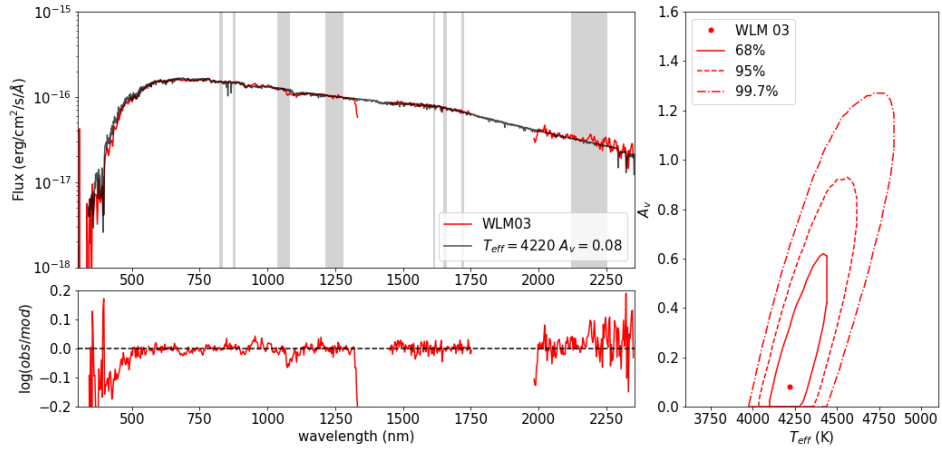
FIGURE B.3: Same as Fig. B.1 but for WLM 03.
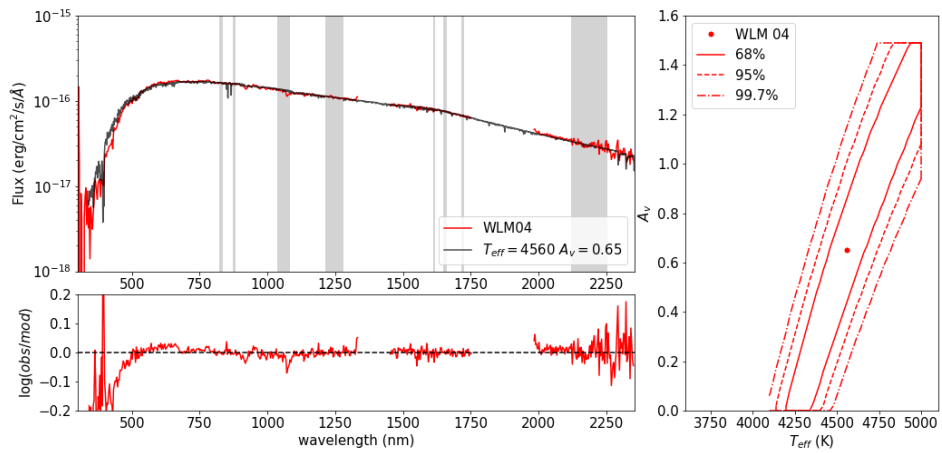
FIGURE B.4: Same as Fig. B.1 but for WLM 04.
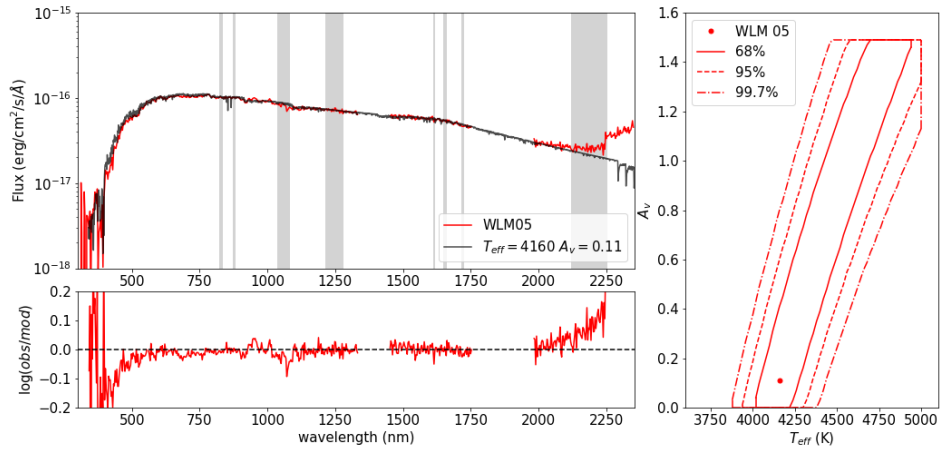
Figure B.5: Same as Fig. B.1 but for WLM 05.
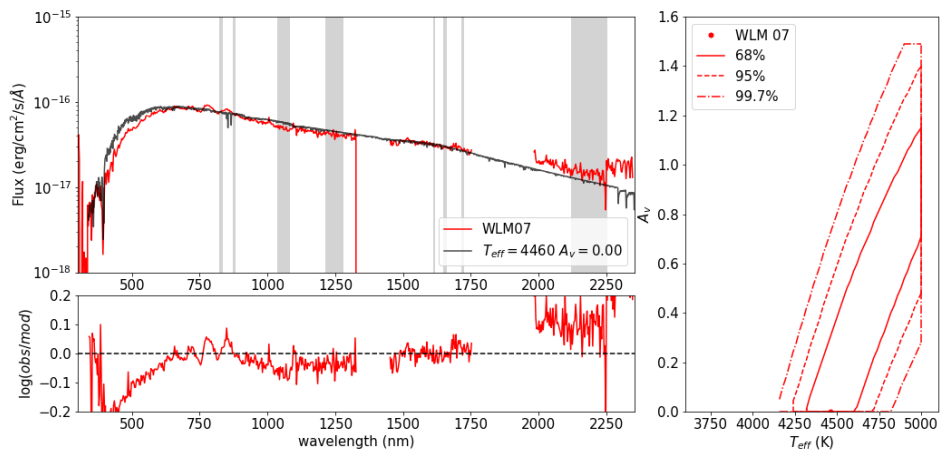
Figure B.6: Same as Fig. B.1 but for WLM 07. This star is the problematic case and we suspect it is not part of the galaxy WLM.
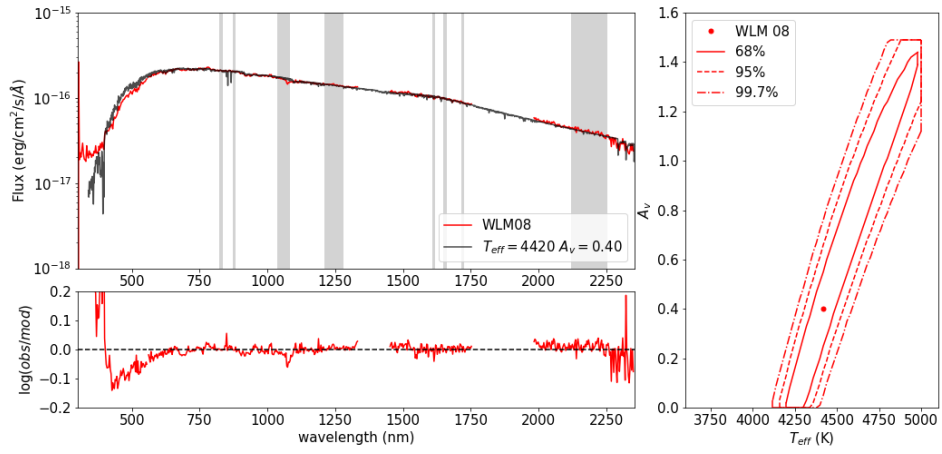
FIGURE B.7: Same as Fig. B.1 but for WLM 08.
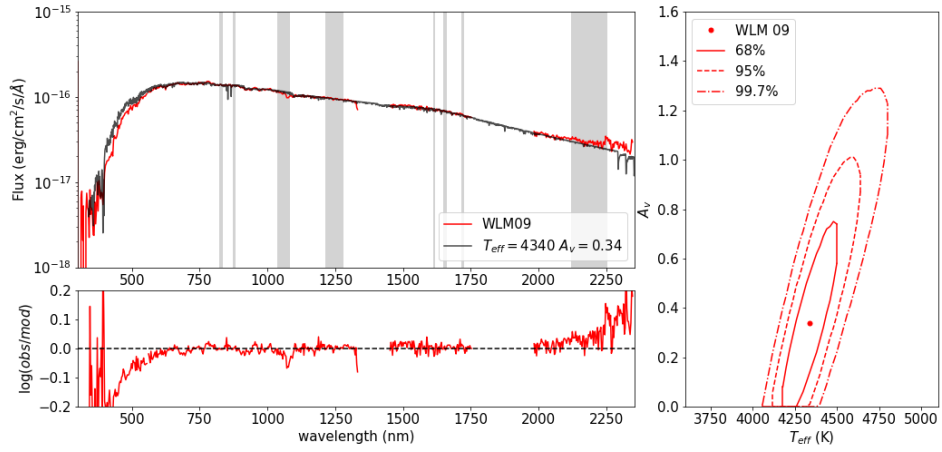
FIGURE B.8: Same as Fig. B.1 but for WLM 09.
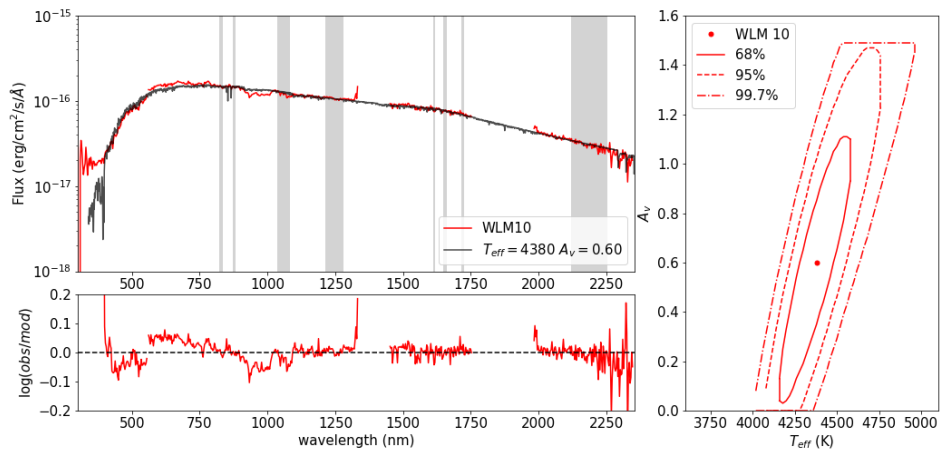
FIGURE B.9: Same as Fig. B.1 but for WLM 10.
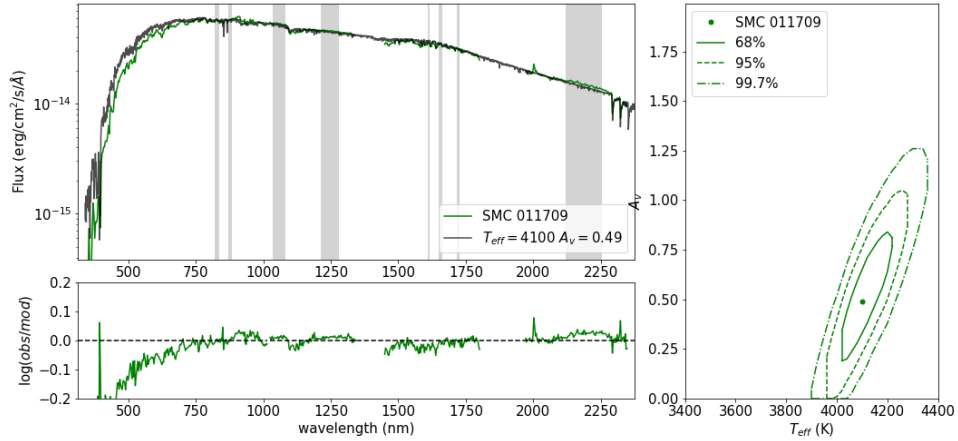
FIGURE B.10: Three panels showing the results of the analysis for the SMC 011709. *Upper left:* Shows the smoothed data (green) and best fitted MARCS model (black), while the SED regions for the analysis are shown in gray. *Lower left:* The residuals of the fit. *Right:* shows the 68%, 95% and 99.7% confidence contours for the best fitted effective temperature and extinction.
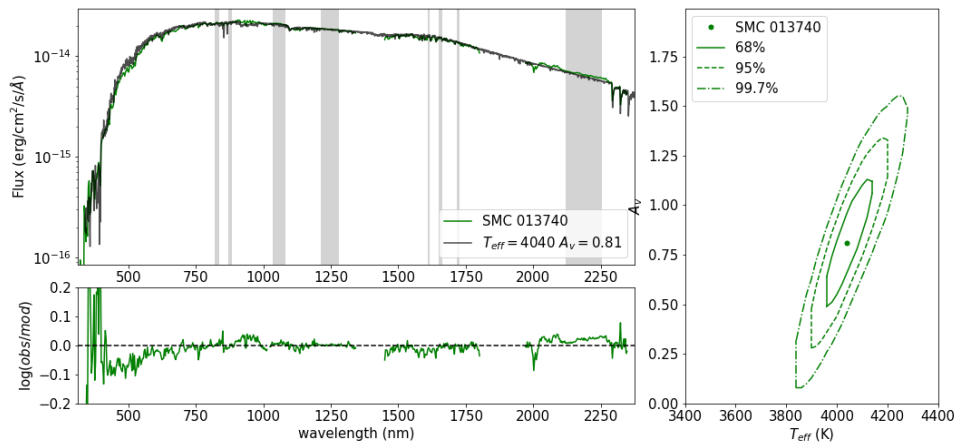
FIGURE B.11: Same as Fig. B.10 but for SMC 013740.
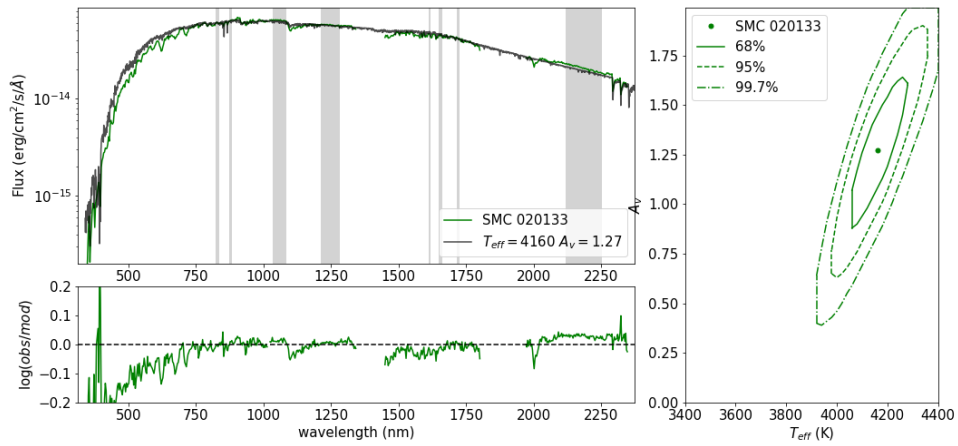
FIGURE B.12: Same as Fig. B.10 but for SMC 020133.
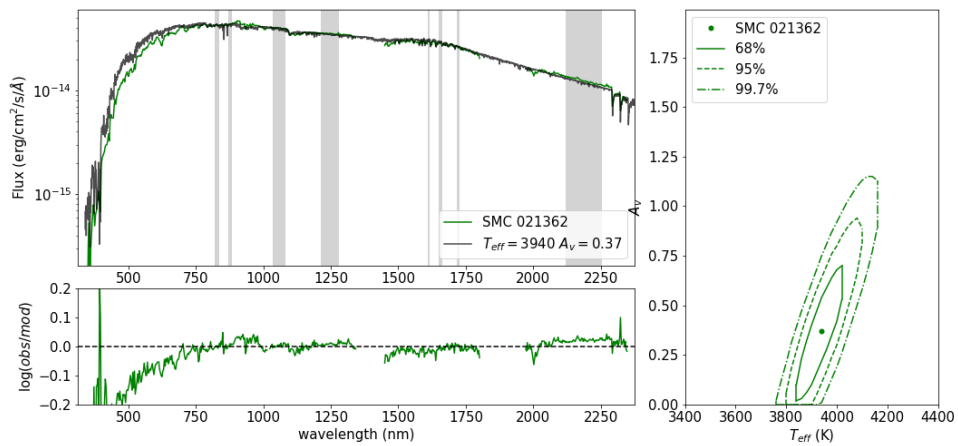
FIGURE B.13: Same as Fig. B.10 but for SMC 021362.
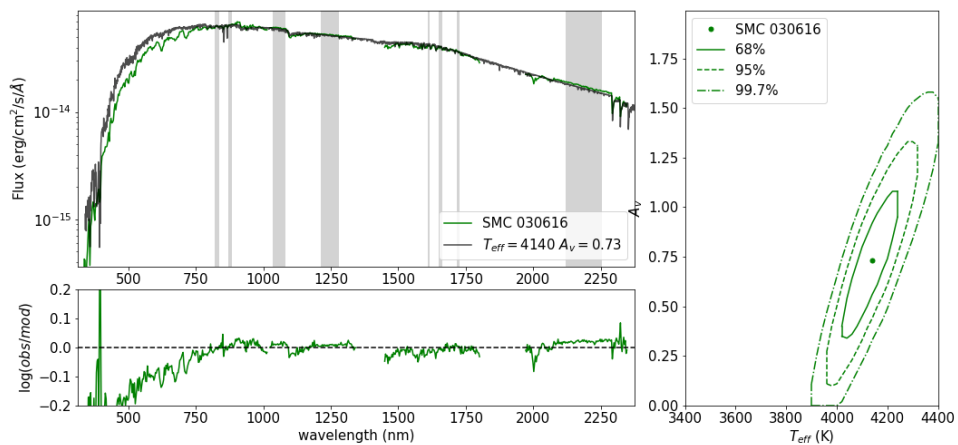
FIGURE B.14: Same as Fig. B.10 but for SMC 030616.
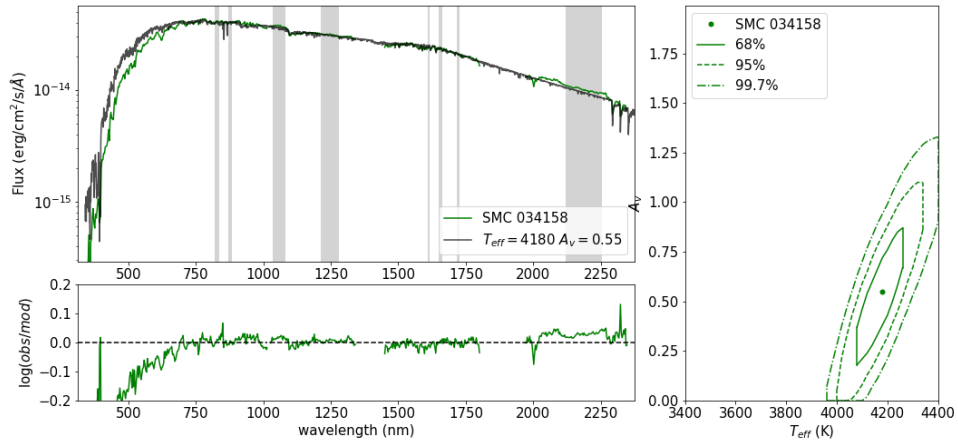
FIGURE B.15: Same as Fig. B.10 but for SMC 034158.
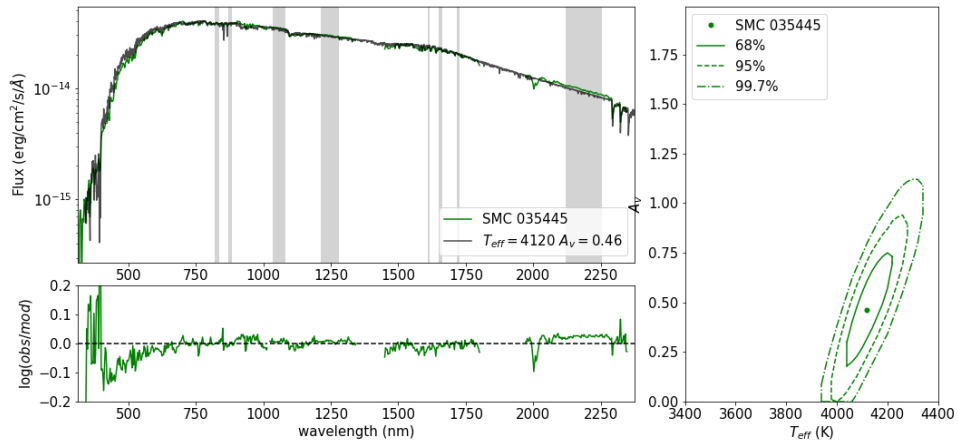
FIGURE B.16: Same as Fig. B.10 but for SMC 035445.
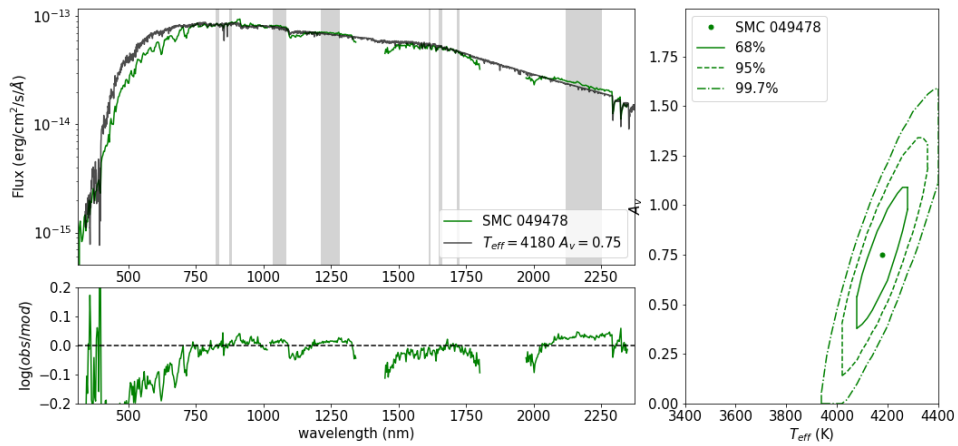
FIGURE B.17: Same as Fig. B.10 but for SMC 049478.
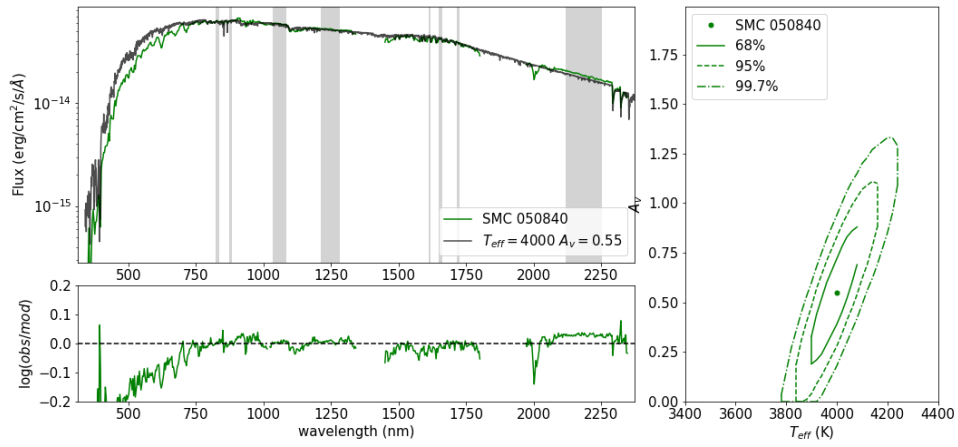
FIGURE B.18: Same as Fig. B.10 but for SMC 050840.
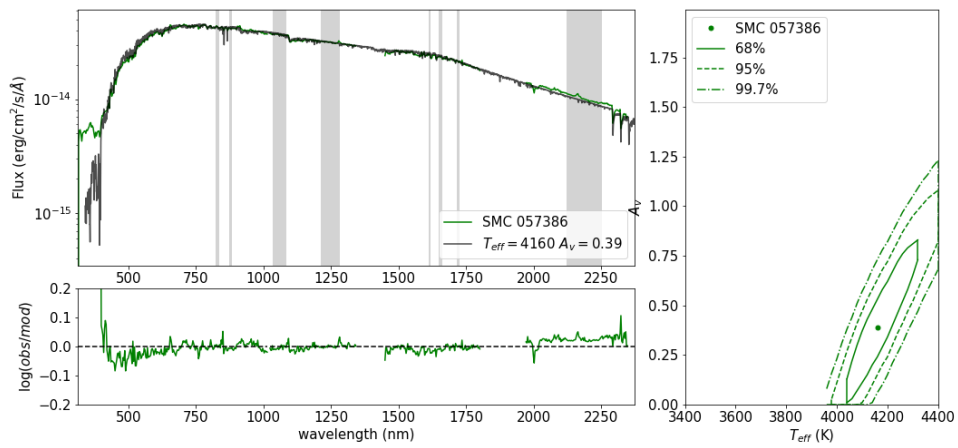
FIGURE B.19: Same as Fig. B.10 but for SMC 057386.
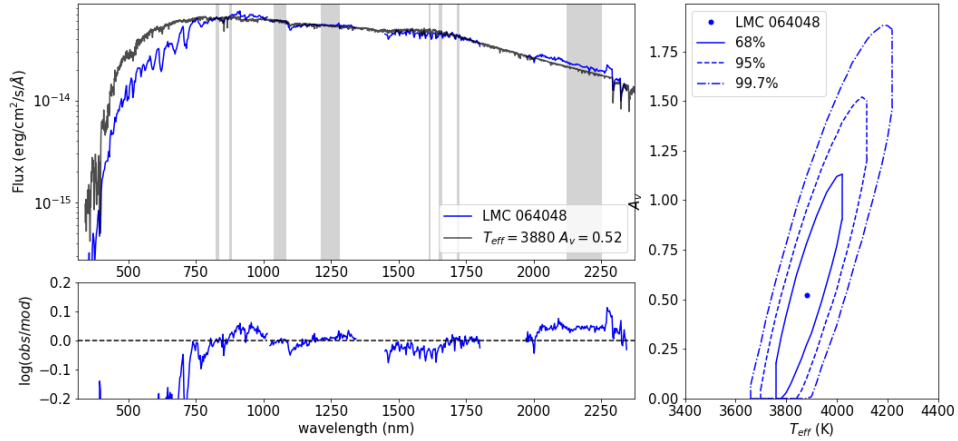
Figure B.20: Three panels showing the results of the analysis at the LMC 064048. *Upper left:* Shows the smoothed data (blue) and best fitted MARCS model (black), while the SED regions for the analysis are shown in gray. *Lower left:* The residuals of the fit. *Right:* shows the 68%, 95% and 99.7% confidence contours for the best fitted effective temperature and extinction.
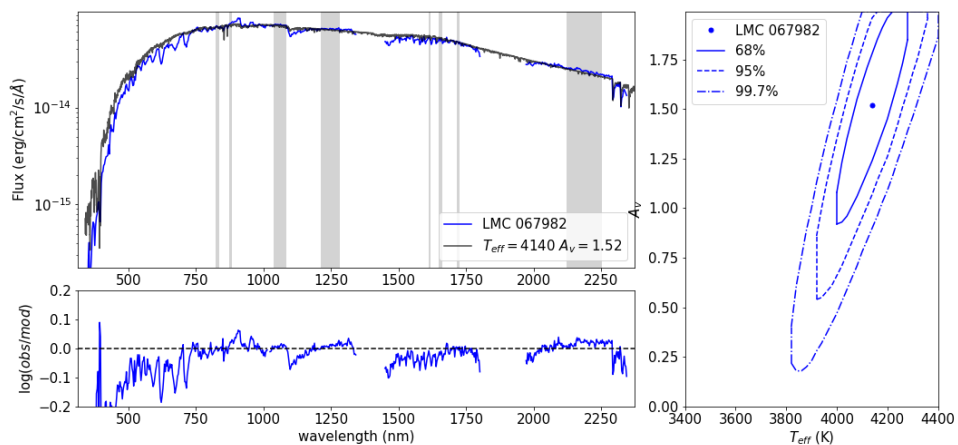
Figure B.21: Same as Fig. B.20 but for LMC 067982.
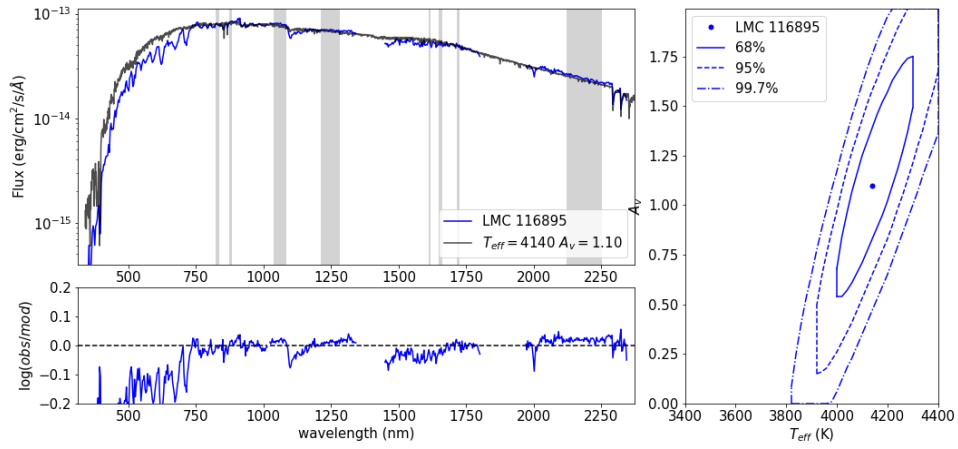
Figure B.22: Same as Fig. B.20 but for LMC 116895.
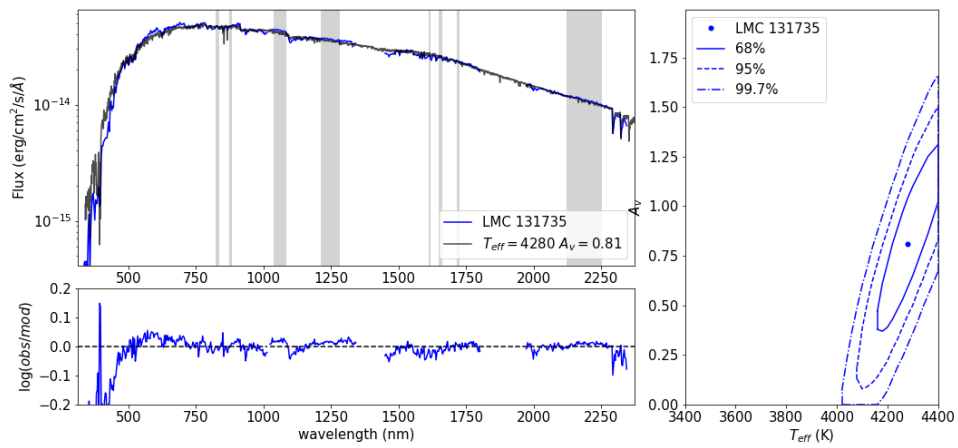
Figure B.23: Same as Fig. B.20 but for LMC 131735.
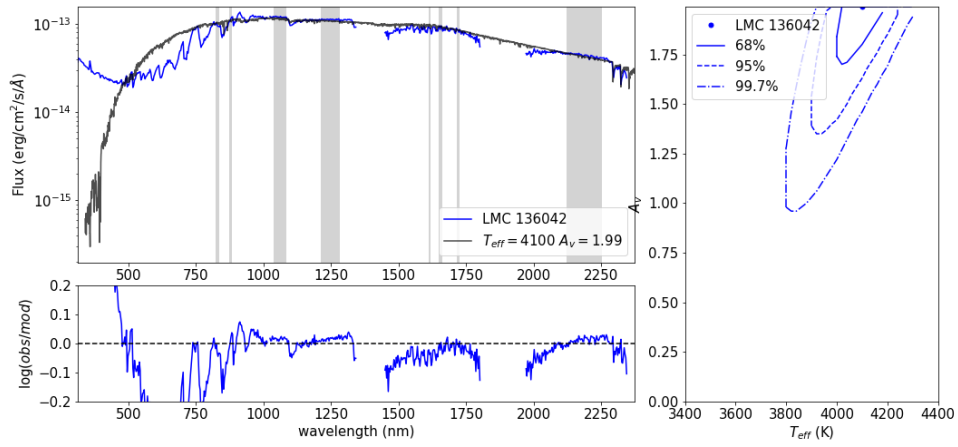
Figure B.24: Same as Fig. B.20 but for LMC 136042. This is a problematic case that can have a near blue star that contaminates the spectrum.
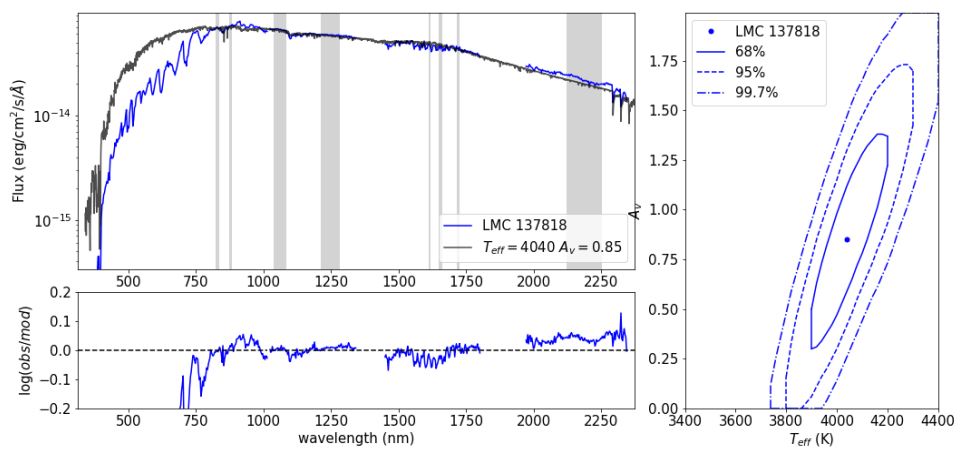
Figure B.25: Same as Fig. B.20 but for LMC 137818.
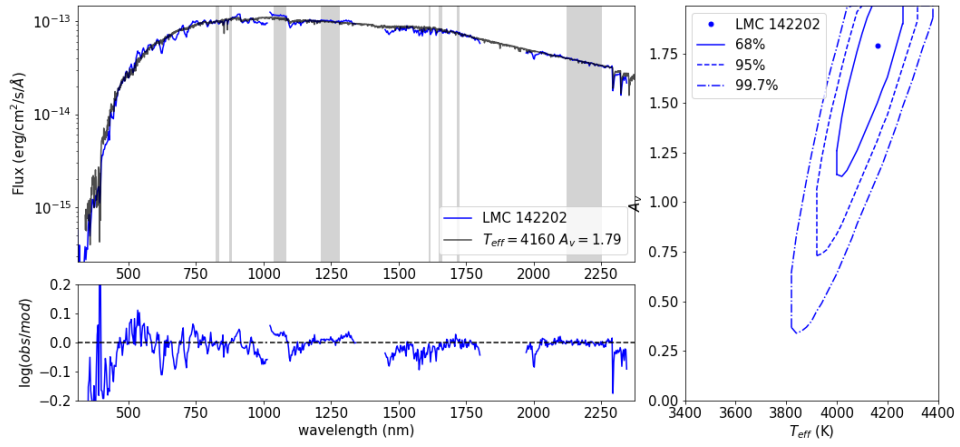
Figure B.26: Same as Fig. B.20 but for LMC 142202.
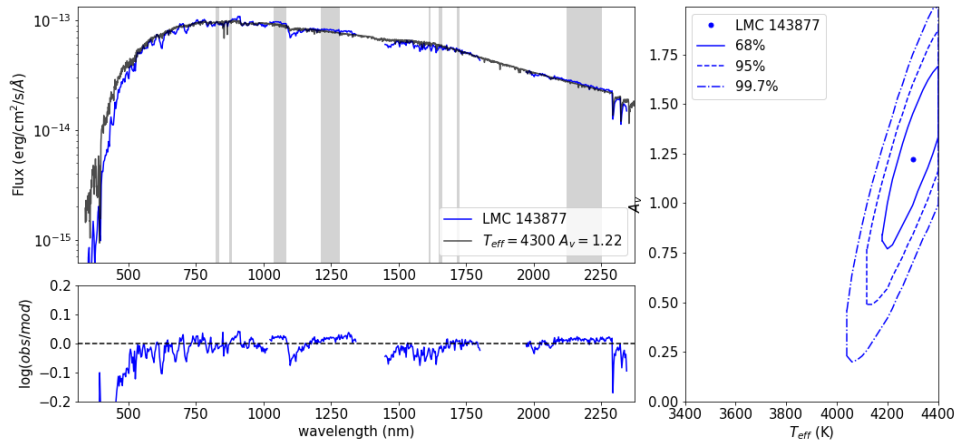
Figure B.27: Same as Fig. B.20 but for LMC 143877.
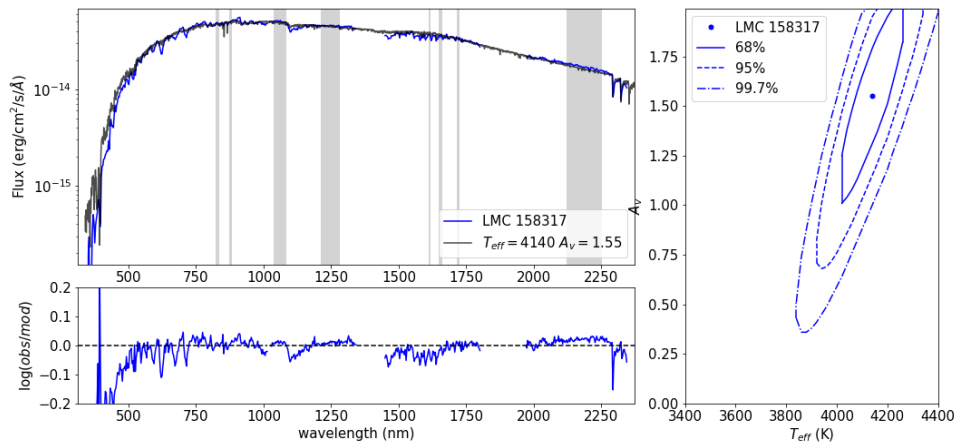
Figure B.28: Same as Fig. B.20 but for LMC 158317.

Appendix C

Chromospheric temperature profile fit
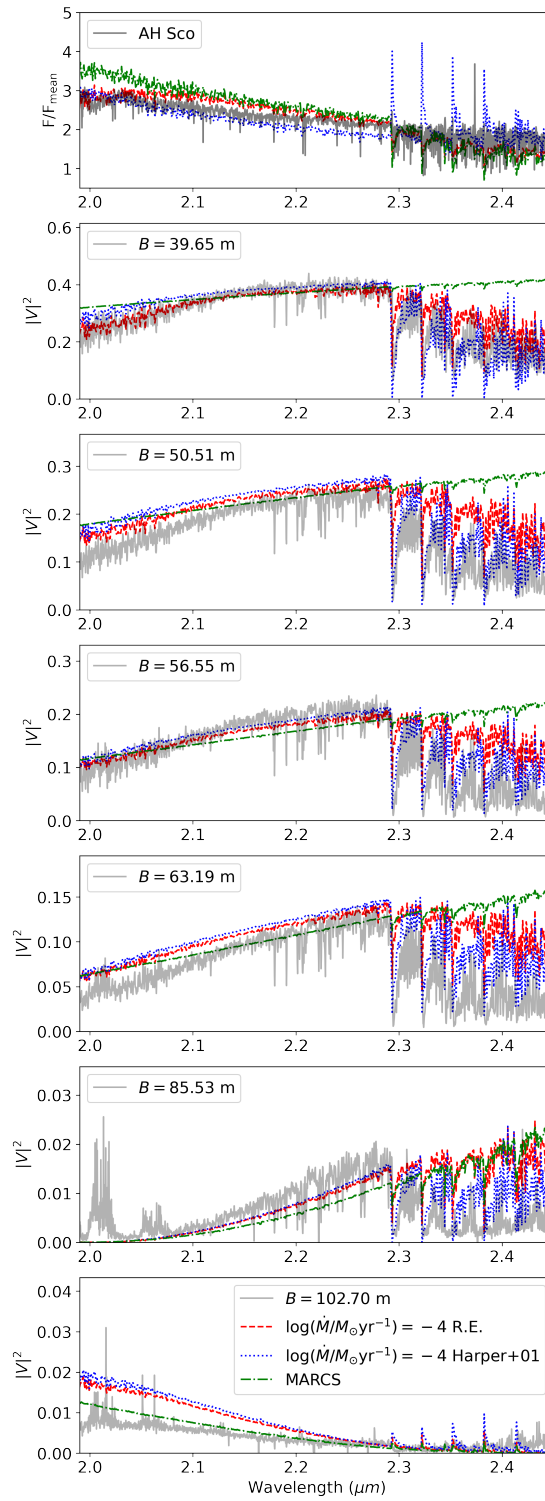
FIGURE C.1: *Upper left:*   Normalized flux for the RSG AH Sco (grey), as observed with VLTI/GRAVITY for the K band. Our best-fit model is shown in red for R.E., and in blue for chromospheric temperature profile, while the pure MARCS model fit is shown in green. *Rest:*   Same as the upper panel but for the $|V|^2$ with different baselines. We see that the CO lines are in emission for the chromospheric temperature profile flux, which is not observed in the data.
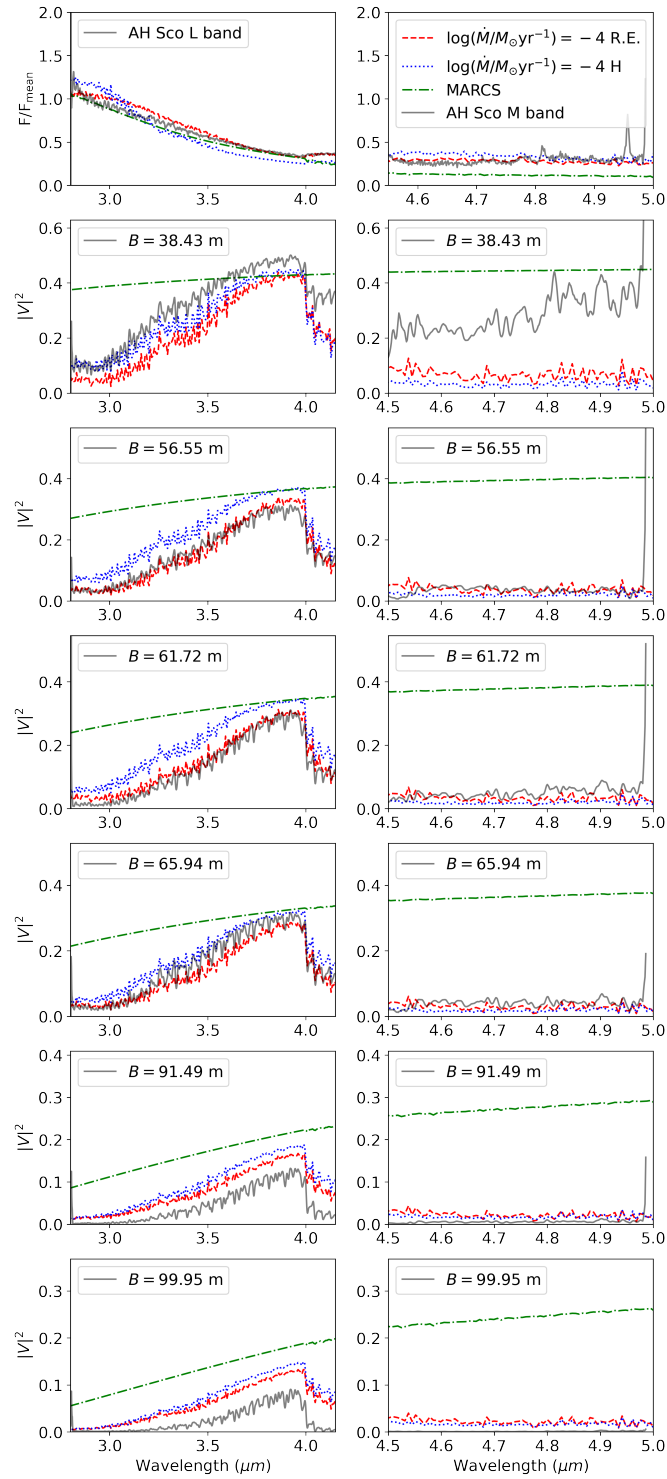
FIGURE C.2: *Up:* Normalized flux for the RSG AH Sco (grey), as observed with VLTI/MATISSE for the *L* (*right panels*) and *M* bands (*left panels*). Our best-fit model is shown in red, and in blue the chromopheric temperature profile, while the pure MARCS model fit is shown in green. *Low:* Same as the upper panel but for the $|V|^2$ with different baselines. Again, both flux and $|V|^2$ are better represented by our R.E. fit.

Appendix D

VLTI/MATISSE N-band data
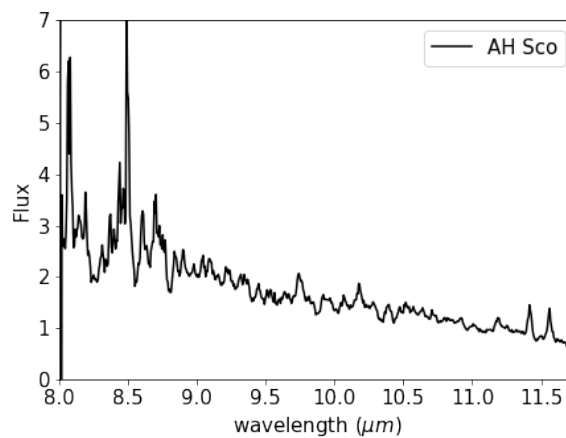
FIGURE D.1: Reduced N band normalized flux for AH Sco. We excluded the region $\lambda > 12\,\mu$m because it was polluted by very high noise.
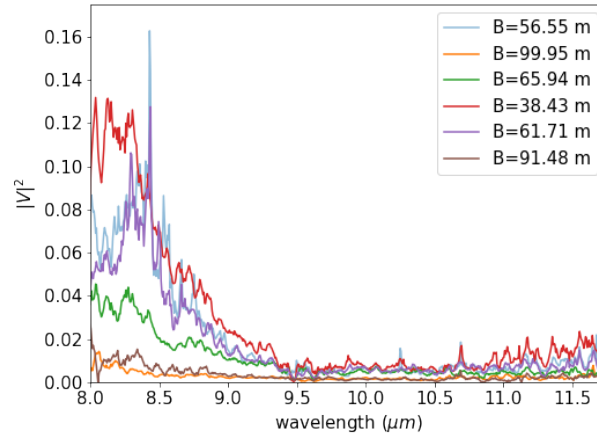
FIGURE D.2: Reduced N band $|V|^2$ for AH Sco, for each of the four beams. We excluded the region $\lambda > 12\,\mu$m because it was polluted by very high noise.
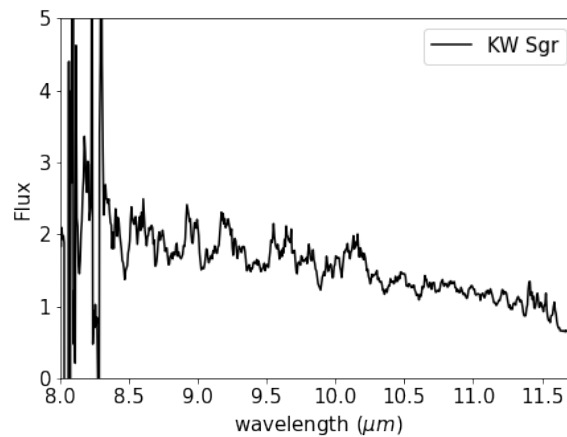
FIGURE D.3: Same as Figure D.1 but for KW Sgr.
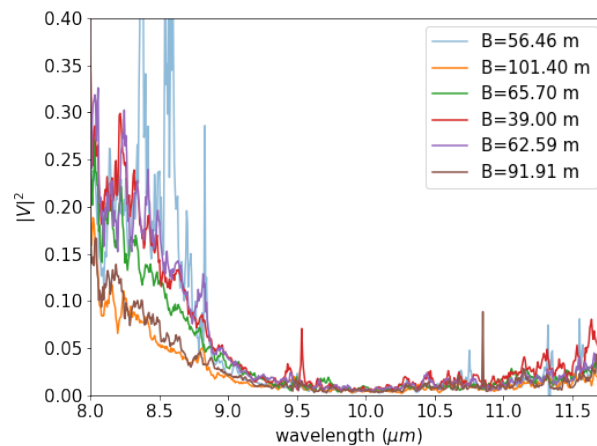
FIGURE D.4: Same as Figure D.2 but for KW Sgr.
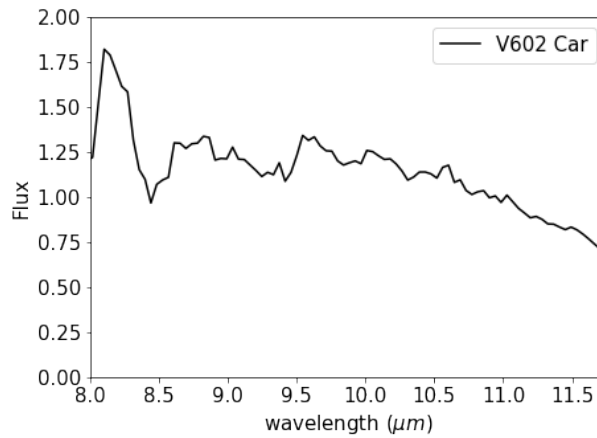
FIGURE D.5: Same as Figure D.1 but for V602 Car. The resolution is LOW in this case.
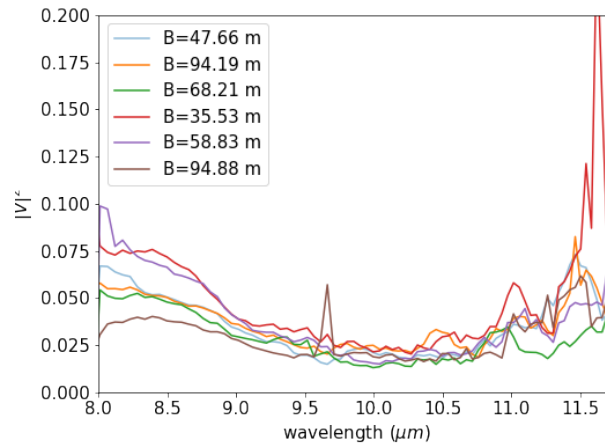
FIGURE D.6: Same as Figure D.2 but for V602 Car. The resolution is LOW in this case.
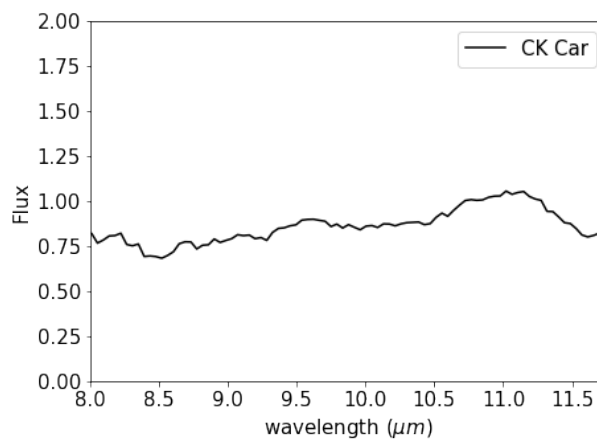
FIGURE D.7: Same as Figure D.1 but for CK Car. The resolution is LOW in this case.
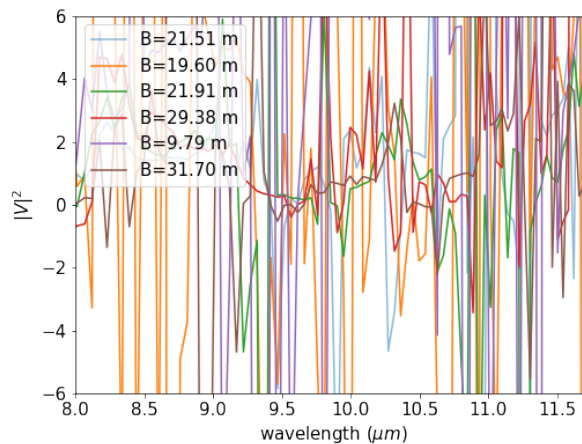
FIGURE D.8: Same as Figure D.2 but for CK Car. The resolution is LOW in this case.
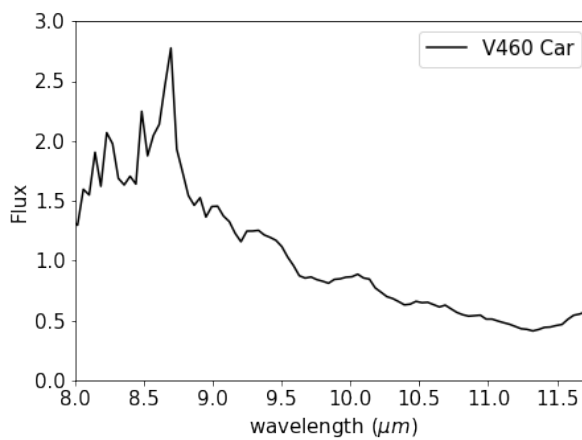
FIGURE D.9: Same as Figure D.1 but for V460 Car. The resolution is LOW in this case.
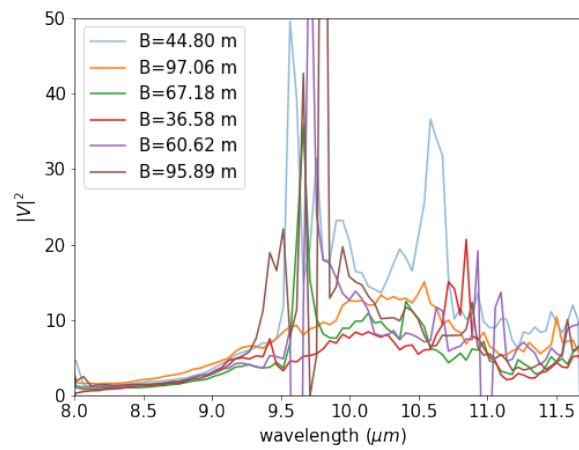
FIGURE D.10: Same as Figure D.2 but for V460 Car. The resolution is LOW in this case.

Bibliography

Ahmad, A., Freytag, B., and Höfner, S. (2023). Properties of self-excited pulsations in 3D simulations of AGB stars and red supergiants. *A&A*, 669:A49.

Anderson, L. S. and Athay, R. G. (1989a). Chromospheric and Coronal Heating. *ApJ*, 336:1089.

Anderson, L. S. and Athay, R. G. (1989b). Model Solar Chromosphere with Prescribed Heating. *ApJ*, 346:1010.

Andrews, H., De Beck, E., and Hirvonen, P. (2022). Multiple components in the molecular outflow of the red supergiant NML Cyg. *MNRAS*, 510(1):383–398.

Arroyo-Torres, B., Wittkowski, M., Chiavassa, A., Scholz, M., Freytag, B., Marcaide, J. M., Hauschildt, P. H., Wood, P. R., and Abellan, F. J. (2015). What causes the large extensions of red supergiant atmospheres?. Comparisons of interferometric observations with 1D hydrostatic, 3D convection, and 1D pulsating model atmospheres. *A&A*, 575:A50.

Arroyo-Torres, B., Wittkowski, M., Marcaide, J. M., and Hauschildt, P. H. (2013). The atmospheric structure and fundamental parameters of the red supergiants AH Scorpii, UY Scuti, and KW Sagittarii. *A&A*, 554:A76.

Avni, Y. (1976). Energy spectra of X-ray clusters of galaxies. *ApJ*, 210:642–646.

Beasor, E. R. and Davies, B. (2017). The evolution of red supergiant mass-loss rates. *Monthly Notices of the Royal Astronomical Society*, 475(1):55–62.

Beasor, E. R. and Davies, B. (2018). The evolution of red supergiant mass-loss rates. *MNRAS*, 475(1):55–62.

Beasor, E. R., Davies, B., and Smith, N. (2021a). The Impact of Realistic Red Supergiant Mass Loss on Stellar Evolution. *ApJ*, 922(1):55.

Beasor, E. R., Davies, B., Smith, N., Gehrz, R. D., and Figer, D. F. (2021b). The Age of Westerlund 1 Revisited. *ApJ*, 912(1):16.

Beasor, E. R., Davies, B., Smith, N., van Loon, J. T., Gehrz, R. D., and Figer, D. F. (2020). A new mass-loss rate prescription for red supergiants. *MNRAS*, 492(4):5994–6006.

Bergemann, M., Kudritzki, R. P., Davies, B., Plez, B., Gazak, Z., and Chiavassa, A. (2013a). <3D> NLTE line formation in the atmospheres of red supergiants. In Kervella, P., Le Bertre, T., and Perrin, G., editors, *EAS Publications Series*, volume 60 of *EAS Publications Series*, pages 103–109.

Bergemann, M., Kudritzki, R.-P., Würl, M., Plez, B., Davies, B., and Gazak, Z. (2013b). Red Supergiant Stars as Cosmic Abundance Probes. II. NLTE Effects in J-band Silicon Lines. *ApJ*, 764(2):115.

Berger, J. P. and Segransan, D. (2007). An introduction to visibility modeling. *New A Rev.*, 51(8-9):576–582.

Bertelli, G., Bressan, A., Chiosi, C., Fagotto, F., and Nasi, E. (1994). Theoretical isochrones from models with new radiative opacities. *A&AS*, 106:275–302.

Böhm-Vitense, E. (1958). Über die Wasserstoffkonvektionszone in Sternen verschiedener Effektivtemperaturen und Leuchtkräfte. Mit 5 Textabbildungen. *ZAp*, 46:108.

Bourges, L., Mella, G., Lafrasse, S., Duvert, G., Chelli, A., Le Bouquin, J. B., Delfosse, X., and Chesneau, O. (2017). VizieR Online Data Catalog: JMMC Stellar Diameters Catalogue - JSDC. Version 2 (Bourges+, 2017). *VizieR Online Data Catalog*, page II/346.

Bowen, G. H. (1988). Dynamical Modeling of Long-Period Variable Star Atmospheres. *ApJ*, 329:299.

Boyer, M. L., McQuinn, K. B. W., Barmby, P., Bonanos, A. Z., Gehrz, R. D., Gordon, K. D., Groenewegen, M. A. T., Lagadec, E., Lennon, D., Marengo, M., Meixner, M., Skillman, E., Sloan, G. C., Sonneborn, G., van Loon, J. T., and Zijlstra, A. (2015). An Infrared Census of Dust in nearby Galaxies with Spitzer (DUSTiNGS). I. Overview. *ApJS*, 216(1):10.

Bradshaw, P. (1974). Possible origin of Prandt's mixing-length theory. *Nature*, 249(5453):135–136.

Brott, I., de Mink, S. E., Cantiello, M., Langer, N., de Koter, A., Evans, C. J., Hunter, I., Trundle, C., and Vink, J. S. (2011). Rotating massive main-sequence stars. I. Grids of evolutionary models and isochrones. *A&A*, 530:A115.

Cardelli, J. A., Clayton, G. C., and Mathis, J. S. (1989). The Relationship between Infrared, Optical, and Ultraviolet Extinction. *ApJ*, 345:245.

Carlsson, M. and Stein, R. F. (1995). Does a Nonmagnetic Solar Chromosphere Exist? *ApJ*, 440:L29.

Chambers, K. C., Magnier, E. A., Metcalfe, N., Flewelling, H. A., Huber, M. E., Waters, C. Z., Denneau, L., Draper, P. W., Farrow, D., Finkbeiner, D. P., Holmberg, C., Koppenhoefer, J., Price, P. A., Rest, A., Saglia, R. P., Schlafly, E. F., Smartt, S. J., Sweeney, W., Wainscoat, R. J., Burgett, W. S., Chastel, S., Grav, T., Heasley, J. N., Hodapp, K. W., Jedicke, R., Kaiser, N., Kudritzki, R. P., Luppino, G. A., Lupton, R. H., Monet, D. G., Morgan, J. S., Onaka, P. M., Shiao, B., Stubbs, C. W., Tonry, J. L., White, R., Bañados, E., Bell, E. F., Bender, R., Bernard, E. J., Boegner, M., Boffi, F., Botticella, M. T., Calamida, A., Casertano, S., Chen, W. P., Chen, X., Cole, S., Deacon, N., Frenk, C., Fitzsimmons, A., Gezari, S., Gibbs, V., Goessl, C., Goggia, T., Gourgue, R., Goldman, B., Grant, P., Grebel, E. K., Hambly, N. C., Hasinger, G., Heavens, A. F., Heckman, T. M., Henderson, R., Henning, T., Holman, M., Hopp, U., Ip, W. H., Isani, S., Jackson, M., Keyes, C. D., Koekemoer, A. M., Kotak, R., Le, D., Liska, D., Long, K. S., Lucey, J. R., Liu, M., Martin, N. F., Masci, G., McLean, B., Mindel, E., Misra, P., Morganson, E., Murphy, D. N. A., Obaika, A., Narayan, G., Nieto-Santisteban, M. A., Norberg, P., Peacock, J. A., Pier, E. A., Postman, M., Primak, N., Rae, C., Rai, A., Riess, A., Riffeser, A., Rix, H. W., Röser, S., Russel, R., Rutz, L., Schilbach, E., Schultz, A. S. B., Scolnic, D., Strolger, L., Szalay, A., Seitz, S., Small, E., Smith, K. W., Soderblom, D. R., Taylor, P., Thomson, R., Taylor, A. N., Thakar, A. R., Thiel, J., Thilker, D., Unger, D., Urata, Y., Valenti, J., Wagner, J., Walder, T., Walter, F., Watters, S. P., Werner, S., Wood-Vasey, W. M., and Wyse, R. (2016). The Pan-STARRS1 Surveys. *arXiv e-prints*, page arXiv:1612.05560.

Chiavassa, A., Freytag, B., Masseron, T., and Plez, B. (2011a). Radiative hydrodynamics simulations of red supergiant stars. IV. Gray versus non-gray opacities. *A&A*, 535:A22.

Chiavassa, A., Haubois, X., Young, J. S., Plez, B., Josselin, E., Perrin, G., and Freytag, B. (2010). Radiative hydrodynamics simulations of red supergiant stars. II. Simulations of convection on Betelgeuse match interferometric observations. *A&A*, 515:A12.

Chiavassa, A., Kravchenko, K., Montargès, M., Millour, F., Matter, A., Freytag, B., Wittkowski, M., Hocdé, V., Cruzalèbes, P., Allouche, F., Lopez, B., Lagarde, S., Petrov, R. G., Meilland, A., Robbe-Dubois, S., Hofmann, K. H., Weigelt, G., Berio, P., Bendjoya, P., Bettonvil, F., Domiciano de Souza, A., Heininger, M., Henning, T., Isbell, J. W., Jaffe, W., Labadie, L., Lehmitz, M., Meisenheimer, K., Soulain, A., Varga, J., Augereau, J. C., van Boekel, R., Burtscher, L., Danchi, W. C., Dominik, C., Drevon, J., Gámez Rosas, V., Hogerheijde, M. R., Hron, J., Klarmann, L., Kokoulina, E., Lagadec, E., Leftley, J., Mosoni, L., Nardetto, N., Paladini, C., Pantin, E., Schertl, D., Stee, P., Szabados, L., Waters, R., Wolf, S., and Yoffe, G. (2022). The extended atmosphere and circumstellar environment of the cool evolved star VX Sagittarii as seen by MATISSE. *A&A*, 658:A185.

Chiavassa, A., Pasquato, E., Jorissen, A., Sacuto, S., Babusiaux, C., Freytag, B., Ludwig, H. G., Cruzalèbes, P., Rabbia, Y., Spang, A., and Chesneau, O. (2011b). Radiative hydrodynamic simulations of red supergiant stars. III. Spectro-photocentric variability, photometric variability, and consequences on Gaia measurements. *A&A*, 528:A120.

Chiavassa, A., Plez, B., Josselin, E., and Freytag, B. (2009). Radiative hydrodynamics simulations of red supergiant stars. I. interpretation of interferometric observations. *A&A*, 506(3):1351–1365.

Chiosi, C. and Maeder, A. (1986). The evolution of massive stars with mass loss. *ARA&A*, 24:329–375.

Choi, J., Dotter, A., Conroy, C., Cantiello, M., Paxton, B., and Johnson, B. D. (2016). MESA ISOCHRONES AND STELLAR TRACKS (MIST). i. SOLAR-SCALED MODELS. *The Astrophysical Journal*, 823(2):102.

Choi, J., Dotter, A., Conroy, C., Cantiello, M., Paxton, B., and Johnson, B. D. (2016). Mesa Isochrones and Stellar Tracks (MIST). I. Solar-scaled Models. *ApJ*, 823(2):102.

Chun, S.-H., Yoon, S.-C., Jung, M.-K., Kim, D. U., and Kim, J. (2018). Evolutionary Models of Red Supergiants: Evidence for A Metallicity-dependent Mixing Length and Implications for Type IIP Supernova Progenitors. *ApJ*, 853(1):79.

Climent, J. B., Wittkowski, M., Chiavassa, A., Baron, F., Marcaide, J. M., Guirado, J. C., Freytag, B., Höfner, S., Haubois, X., and Woillez, J. (2020). VLTI-PIONIER imaging of the red supergiant V602 Carinae. *A&A*, 635:A160.

Collins, G. W., I. (1978). *The virial theorem in stellar astrophysics.*

Crain, R. A., Schaye, J., Bower, R. G., Furlong, M., Schaller, M., Theuns, T., Dalla Vecchia, C., Frenk, C. S., McCarthy, I. G., Helly, J. C., Jenkins, A., Rosas-Guevara, Y. M., White, S. D. M., and Trayford, J. W. (2015). The EAGLE simulations of galaxy formation: calibration of subgrid physics and model variations. *MNRAS*, 450(2):1937–1961.

Crowther, P. A. (2013). On the association between core-collapse supernovae and H ii regions. *MNRAS*, 428(3):1927–1943.

Cruzalèbes, P., Petrov, R. G., Robbe-Dubois, S., Varga, J., Burtscher, L., Allouche, F., Berio, P., Hofmann, K. H., Hron, J., Jaffe, W., Lagarde, S., Lopez, B., Matter, A., Meilland, A., Meisenheimer, K., Millour, F., and Schertl, D. (2019). A catalogue of stellar diameters and fluxes for mid-infrared interferometry. *MNRAS*, 490(3):3158–3176.

Danchi, W. C., Tuthill, P. G., and Monnier, J. D. (2001). Near-Infrared Interferometric Images of the Hot Inner Disk surrounding the Massive Young Star MWC 349A. *ApJ*, 562(1):440–445.

Davies, B. and Beasor, E. R. (2020). The 'red supergiant problem': the upper luminosity boundary of Type II supernova progenitors. *MNRAS*, 493(1):468–476.

Davies, B., Crowther, P. A., and Beasor, E. R. (2018a). The luminosities of cool supergiants in the Magellanic Clouds, and the Humphreys-Davidson limit revisited. *MNRAS*, 478(3):3138–3148.

Davies, B., Crowther, P. A., and Beasor, E. R. (2018b). VizieR Online Data Catalog: Luminous cool supergiants in Magellanic Clouds (Davies+, 2018). *VizieR Online Data Catalog*, page J/MNRAS/478/3138.

Davies, B., Kudritzki, R.-P., and Figer, D. F. (2010). The potential of red super-giants as extragalactic abundance probes at low spectral resolution. *MNRAS*, 407(2):1203–1211.

Davies, B., Kudritzki, R.-P., Gazak, Z., Plez, B., Bergemann, M., Evans, C., and Patrick, L. (2015). Red Supergiants as Cosmic Abundance Probes: The Magellanic Clouds. *ApJ*, 806(1):21.

Davies, B., Kudritzki, R.-P., Lardo, C., Bergemann, M., Beasor, E., Plez, B., Evans, C., Bastian, N., and Patrick, L. R. (2017). Red Supergiants as Cosmic Abundance Probes: Massive Star Clusters in M83 and the Mass-Metallicity Relation of Nearby Galaxies. *ApJ*, 847(2):112.

Davies, B., Kudritzki, R. P., Plez, B., Bergemann, M., Lançon, A., Trager, S., Gazak, Z., Evans, C., and Chiavassa, A. (2013a). The Temperatures of Red Supergiants: how cool are the coolest massive stars? In Kervella, P., Le Bertre, T., and Perrin, G., editors, *EAS Publications Series*, volume 60 of *EAS Publications Series*, pages 69–76.

Davies, B., Kudritzki, R.-P., Plez, B., Trager, S., Lançon, A., Gazak, Z., Bergemann, M., Evans, C., and Chiavassa, A. (2013b). The Temperatures of Red Supergiants. *ApJ*, 767(1):3.

Davies, B. and Plez, B. (2021). The impact of winds on the spectral appearance of red supergiants. *MNRAS*, 508(4):5757–5765.

Davis, J., Tango, W. J., and Booth, A. J. (2000). Limb-darkening corrections for interferometric uniform disc stellar angular diameters. *MNRAS*, 318(2):387–392.

De Beck, E., Decin, L., de Koter, A., Justtanont, K., Verhoelst, T., Kemper, F., and Menten, K. M. (2010). Probing the mass-loss history of AGB and red supergiant stars from CO rotational line profiles. II. CO line survey of evolved stars: derivation of mass-loss rate formulae. *A&A*, 523:A18.

de Jager, C. (1980). *The brightest stars*, volume 19.

de Jager, C., Nieuwenhuijzen, H., and van der Hucht, K. A. (1988). Mass loss rates in the Hertzsprung-Russell diagram. *A&AS*, 72:259–289.

Decin, L., Hony, S., de Koter, A., Justtanont, K., Tielens, A. G. G. M., and Waters, L. B. F. M. (2006). Probing the mass-loss history of AGB and red

supergiant stars from CO rotational line profiles. I. Theoretical model - Mass-loss history unravelled in ¡ASTROBJ¿VY CMa¡/ASTROBJ¿. *A&A*, 456(2):549–563.

Dessart, L., Hillier, D. J., Waldman, R., and Livne, E. (2013). Type II-Plateau supernova radiation: dependences on progenitor and explosion properties. *MNRAS*, 433(2):1745–1763.

Dharmawardena, T. E., Mairs, S., Scicluna, P., Bell, G., McDonald, I., Menten, K., Weiss, A., and Zijlstra, A. (2020). Betelgeuse Fainter in the Submillimeter Too: An Analysis of JCMT and APEX Monitoring during the Recent Optical Minimum. *ApJ*, 897(1):L9.

D'Odorico, S., Dekker, H., Mazzoleni, R., Vernet, J., Guinouard, I., Groot, P., Hammer, F., Rasmussen, P. K., Kaper, L., Navarro, R., Pallavicini, R., Peroux, C., and Zerbi, F. M. (2006). *X-shooter UV- to K-band intermediate-resolution high-efficiency spectrograph for the VLT: status report at the final design review*, volume 6269 of *Society of Photo-Optical Instrumentation Engineers (SPIE) Conference Series*, page 626933.

Dorda, R., Negueruela, I., González-Fernández, C., and Tabernero, H. M. (2016). Spectral type, temperature, and evolutionary stage in cool supergiants. *A&A*, 592:A16.

Dotter, A. (2016). MESA ISOCHRONES AND STELLAR TRACKS (MIST) 0: METHODS FOR THE CONSTRUCTION OF STELLAR ISOCHRONES. *The Astrophysical Journal Supplement Series*, 222(1):8.

Dullemond, C. P., Juhasz, A., Pohl, A., Sereshti, F., Shetty, R., Peters, T., Commercon, B., and Flock, M. (2012). RADMC-3D: A multi-purpose radiative transfer tool.

Dupree, A. K., Strassmeier, K. G., Calderwood, T., Granzer, T., Weber, M., Kravchenko, K., Matthews, L. D., Montargès, M., Tappin, J., and Thompson, W. T. (2022). The Great Dimming of Betelgeuse: A Surface Mass Ejection and Its Consequences. *ApJ*, 936(1):18.

Dupree, A. K., Strassmeier, K. G., Matthews, L. D., Uitenbroek, H., Calderwood, T., Granzer, T., Guinan, E. F., Leike, R., Montargès, M., Richards, A. M. S., Wasatonic, R., and Weber, M. (2020). Spatially Resolved Ultraviolet Spectroscopy of the Great Dimming of Betelgeuse. *ApJ*, 899(1):68.

Ekström, S., Georgy, C., Eggenberger, P., Meynet, G., Mowlavi, N., Wyttenbach, A., Granada, A., Decressin, T., Hirschi, R., Frischknecht, U., Charbonnel, C., and Maeder, A. (2012). Grids of stellar models with rotation. I. Models from 0.8 to 120 M_{okay} at solar metallicity (Z = 0.014). *A&A*, 537:A146.

Farrell, E., Groh, J. H., Meynet, G., and Eldridge, J. J. (2022). Numerical experiments to help understand cause and effect in massive star evolution. *MNRAS*, 512(3):4116–4135.

Ferraro, F. R., Fusi Pecci, F., Tosi, M., and Buonanno, R. (1989). A method for studying the star formation history of dwarf irregular galaxies - I. CCD photometry of WLM. *MNRAS*, 241:433–452.

Freytag, B., Steffen, M., Wedemeyer-Böhm, S., Ludwig, H.-G., Leenaarts, J., Schaffenberger, W., Allard, F., Chiavassa, A., Höfner, S., Kamp, I., and Steiner, O. (2010). CO5BOLD: COnservative COde for the COmputation of COmpressible COnvection in a BOx of L Dimensions with l=2,3. Astrophysics Source Code Library, record ascl:1011.014.

Gaia Collaboration, Brown, A. G. A., Vallenari, A., Prusti, T., de Bruijne, J. H. J., Babusiaux, C., Bailer-Jones, C. A. L., Biermann, M., Evans, D. W., Eyer, L., Jansen, F., Jordi, C., Klioner, S. A., Lammers, U., Lindegren, L., Luri, X., Mignard, F., Panem, C., Pourbaix, D., Randich, S., Sartoretti, P., Siddiqui, H. I., Soubiran, C., van Leeuwen, F., Walton, N. A., Arenou, F., Bastian, U., Cropper, M., Drimmel, R., Katz, D., Lattanzi, M. G., Bakker, J., Cacciari, C., Castañeda, J., Chaoul, L., Cheek, N., De Angeli, F., Fabricius, C., Guerra, R., Holl, B., Masana, E., Messineo, R., Mowlavi, N., Nienartowicz, K., Panuzzo, P., Portell, J., Riello, M., Seabroke, G. M., Tanga, P., Thévenin, F., Gracia-Abril, G., Comoretto, G., Garcia-Reinaldos, M., Teyssier, D., Altmann, M., Andrae, R., Audard, M., Bellas-Velidis, I., Benson, K., Berthier, J., Blomme, R., Burgess, P., Busso, G., Carry, B., Cellino, A., Clementini, G., Clotet, M., Creevey, O., Davidson, M., De Ridder, J., Delchambre, L., Dell'Oro, A., Ducourant, C., Fernández-Hernández, J., Fouesneau, M., Frémat, Y., Galluccio, L., García-Torres, M., González-Núñez, J., González-Vidal, J. J., Gosset, E., Guy, L. P., Halbwachs, J. L., Hambly, N. C., Harrison, D. L., Hernández, J., Hestroffer, D., Hodgkin, S. T., Hutton, A., Jasniewicz, G., Jean-Antoine-Piccolo, A., Jordan, S., Korn, A. J., Krone-Martins, A., Lanzafame, A. C., Lebzelter, T., Löffler, W., Manteiga, M., Marrese, P. M., Martín-Fleitas, J. M.,

Moitinho, A., Mora, A., Muinonen, K., Osinde, J., Pancino, E., Pauwels, T., Petit, J. M., Recio-Blanco, A., Richards, P. J., Rimoldini, L., Robin, A. C., Sarro, L. M., Siopis, C., Smith, M., Sozzetti, A., Süveges, M., Torra, J., van Reeven, W., Abbas, U., Abreu Aramburu, A., Accart, S., Aerts, C., Altavilla, G., Álvarez, M. A., Alvarez, R., Alves, J., Anderson, R. I., Andrei, A. H., Anglada Varela, E., Antiche, E., Antoja, T., Arcay, B., Astraatmadja, T. L., Bach, N., Baker, S. G., Balaguer-Núñez, L., Balm, P., Barache, C., Barata, C., Barbato, D., Barblan, F., Barklem, P. S., Barrado, D., Barros, M., Barstow, M. A., Bartholomé Muñoz, S., Bassilana, J. L., Becciani, U., Bellazzini, M., Berihuete, A., Bertone, S., Bianchi, L., Bienaymé, O., Blanco-Cuaresma, S., Boch, T., Boeche, C., Bombrun, A., Borrachero, R., Bossini, D., Bouquillon, S., Bourda, G., Bragaglia, A., Bramante, L., Breddels, M. A., Bressan, A., Brouillet, N., Brüsemeister, T., Brugaletta, E., Bucciarelli, B., Burlacu, A., Busonero, D., Butkevich, A. G., Buzzi, R., Caffau, E., Cancelliere, R., Cannizzaro, G., Cantat-Gaudin, T., Carballo, R., Carlucci, T., Carrasco, J. M., Casamiquela, L., Castellani, M., Castro-Ginard, A., Charlot, P., Chemin, L., Chiavassa, A., Cocozza, G., Costigan, G., Cowell, S., Crifo, F., Crosta, M., Crowley, C., Cuypers, J., Dafonte, C., Damerdji, Y., Dapergolas, A., David, P., David, M., de Laverny, P., De Luise, F., De March, R., de Martino, D., de Souza, R., de Torres, A., Debosscher, J., del Pozo, E., Delbo, M., Delgado, A., Delgado, H. E., Di Matteo, P., Diakite, S., Diener, C., Distefano, E., Dolding, C., Drazinos, P., Durán, J., Edvardsson, B., Enke, H., Eriksson, K., Esquej, P., Eynard Bontemps, G., Fabre, C., Fabrizio, M., Faigler, S., Falcão, A. J., Farràs Casas, M., Federici, L., Fedorets, G., Fernique, P., Figueras, F., Filippi, F., Findeisen, K., Fonti, A., Fraile, E., Fraser, M., Frézouls, B., Gai, M., Galleti, S., Garabato, D., García-Sedano, F., Garofalo, A., Garralda, N., Gavel, A., Gavras, P., Gerssen, J., Geyer, R., Giacobbe, P., Gilmore, G., Girona, S., Giuffrida, G., Glass, F., Gomes, M., Granvik, M., Gueguen, A., Guerrier, A., Guiraud, J., Gutiérrez-Sánchez, R., Haigron, R., Hatzidimitriou, D., Hauser, M., Haywood, M., Heiter, U., Helmi, A., Heu, J., Hilger, T., Hobbs, D., Hofmann, W., Holland, G., Huckle, H. E., Hypki, A., Icardi, V., Janßen, K., Jevardat de Fombelle, G., Jonker, P. G., Juhász, Á. L., Julbe, F., Karampelas, A., Kewley, A., Klar, J., Kochoska, A., Kohley, R., Kolenberg, K., Kontizas, M., Kontizas, E., Koposov, S. E., Kordopatis, G., Kostrzewa-Rutkowska, Z., Koubsky, P., Lambert, S., Lanza, A. F., Lasne, Y., Lavigne, J. B., Le Fustec, Y., Le Poncin-Lafitte,

C., Lebreton, Y., Leccia, S., Leclerc, N., Lecoeur-Taibi, I., Lenhardt, H., Leroux, F., Liao, S., Licata, E., Lindstrøm, H. E. P., Lister, T. A., Livanou, E., Lobel, A., López, M., Managau, S., Mann, R. G., Mantelet, G., Marchal, O., Marchant, J. M., Marconi, M., Marinoni, S., Marschalkó, G., Marshall, D. J., Martino, M., Marton, G., Mary, N., Massari, D., Matijevič, G., Mazeh, T., McMillan, P. J., Messina, S., Michalik, D., Millar, N. R., Molina, D., Molinaro, R., Molnár, L., Montegriffo, P., Mor, R., Morbidelli, R., Morel, T., Morris, D., Mulone, A. F., Muraveva, T., Musella, I., Nelemans, G., Nicastro, L., Noval, L., O'Mullane, W., Ordénovic, C., Ordóñez-Blanco, D., Osborne, P., Pagani, C., Pagano, I., Pailler, F., Palacin, H., Palaversa, L., Panahi, A., Pawlak, M., Piersimoni, A. M., Pineau, F. X., Plachy, E., Plum, G., Poggio, E., Poujoulet, E., Prša, A., Pulone, L., Racero, E., Ragaini, S., Rambaux, N., Ramos-Lerate, M., Regibo, S., Reylé, C., Riclet, F., Ripepi, V., Riva, A., Rivard, A., Rixon, G., Roegiers, T., Roelens, M., Romero-Gómez, M., Rowell, N., Royer, F., Ruiz-Dern, L., Sadowski, G., Sagristà Sellés, T., Sahlmann, J., Salgado, J., Salguero, E., Sanna, N., Santana-Ros, T., Sarasso, M., Savietto, H., Schultheis, M., Sciacca, E., Segol, M., Segovia, J. C., Ségransan, D., Shih, I. C., Siltala, L., Silva, A. F., Smart, R. L., Smith, K. W., Solano, E., Solitro, F., Sordo, R., Soria Nieto, S., Souchay, J., Spagna, A., Spoto, F., Stampa, U., Steele, I. A., Steidelmüller, H., Stephenson, C. A., Stoev, H., Suess, F. F., Surdej, J., Szabados, L., Szegedi-Elek, E., Tapiador, D., Taris, F., Tauran, G., Taylor, M. B., Teixeira, R., Terrett, D., Teyssand ier, P., Thuillot, W., Titarenko, A., Torra Clotet, F., Turon, C., Ulla, A., Utrilla, E., Uzzi, S., Vaillant, M., Valentini, G., Valette, V., van Elteren, A., Van Hemelryck, E., van Leeuwen, M., Vaschetto, M., Vecchiato, A., Veljanoski, J., Viala, Y., Vicente, D., Vogt, S., von Essen, C., Voss, H., Votruba, V., Voutsinas, S., Walmsley, G., Weiler, M., Wertz, O., Wevers, T., Wyrzykowski, Ł., Yoldas, A., Žerjal, M., Ziaeepour, H., Zorec, J., Zschocke, S., Zucker, S., Zurbach, C., and Zwitter, T. (2018). Gaia Data Release 2. Summary of the contents and survey properties. *A&A*, 616:A1.

Gail, H.-P., Tamanai, A., Pucci, A., and Dohmen, R. (2020). Non-stoichiometric amorphous magnesium-iron silicates in circumstellar dust shells. Dust growth in outflows from supergiants. *A&A*, 644:A139.

Gazak, J. Z., Kudritzki, R., Evans, C., Patrick, L., Davies, B., Bergemann, M., Plez, B., Bresolin, F., Bender, R., Wegner, M., Bonanos, A. Z., and Williams,

S. J. (2015). Red Supergiants as Cosmic Abundance Probes: The Sculptor Galaxy NGC 300. *ApJ*, 805(2):182.

Georgy, C., Ekström, S., Eggenberger, P., Meynet, G., Haemmerlé, L., Maeder, A., Granada, A., Groh, J. H., Hirschi, R., Mowlavi, N., Yusof, N., Charbonnel, C., Decressin, T., and Barblan, F. (2013). Grids of stellar models with rotation. III. Models from 0.8 to 120 M_{okay} at a metallicity Z = 0.002. *A&A*, 558:A103.

Gillessen, S., Eisenhauer, F., Perrin, G., Brandner, W., Straubmeier, C., Perraut, K., Amorim, A., Schöller, M., Araujo-Hauck, C., Bartko, H., Baumeister, H., Berger, J. P., Carvas, P., Cassaing, F., Chapron, F., Choquet, E., Clenet, Y., Collin, C., Eckart, A., Fedou, P., Fischer, S., Gendron, E., Genzel, R., Gitton, P., Gonte, F., Gräter, A., Haguenauer, P., Haug, M., Haubois, X., Henning, T., Hippler, S., Hofmann, R., Jocou, L., Kellner, S., Kervella, P., Klein, R., Kudryavtseva, N., Lacour, S., Lapeyrere, V., Laun, W., Lena, P., Lenzen, R., Lima, J., Moratschke, D., Moch, D., Moulin, T., Naranjo, V., Neumann, U., Nolot, A., Paumard, T., Pfuhl, O., Rabien, S., Ramos, J., Rees, J. M., Rohloff, R. R., Rouan, D., Rousset, G., Sevin, A., Thiel, M., Wagner, K., Wiest, M., Yazici, S., and Ziegler, D. (2010). GRAVITY: a four-telescope beam combiner instrument for the VLTI. In Danchi, W. C., Delplancke, F., and Rajagopal, J. K., editors, *Optical and Infrared Interferometry II*, volume 7734 of *Society of Photo-Optical Instrumentation Engineers (SPIE) Conference Series*, page 77340Y.

Goldman, S. R., van Loon, J. T., Zijlstra, A. A., Green, J. A., Wood, P. R., Nanni, A., Imai, H., Whitelock, P. A., Matsuura, M., Groenewegen, M. A. T., and Gómez, J. F. (2017). The wind speeds, dust content, and mass-loss rates of evolved AGB and RSG stars at varying metallicity. *MNRAS*, 465(1):403–433.

González-Fernández, C., Dorda, R., Negueruela, I., and Marco, A. (2015). A new survey of cool supergiants in the Magellanic Clouds. *A&A*, 578:A3.

González-Torà, G., Davies, B., Kudritzki, R.-P., and Plez, B. (2021). The temperatures of red supergiants in low-metallicity environments. *MNRAS*, 505(3):4422–4443.

González-Torà, G., Urbaneja, M. A., Przybilla, N., Dreizler, S., Roth, M. M., Kamann, S., and Castro, N. (2022). MUSE crowded field 3D spectroscopy in NGC 300. II. Quantitative spectroscopy of BA-type supergiants. *A&A*, 658:A117.

González-Torà, G., Wittkowski, M., Davies, B., Plez, B., and Kravchenko, K. (2023). The effect of winds on atmospheric layers of red supergiants. I. Modelling for interferometric observations. *A&A*, 669:A76.

Gordon, K. D., Clayton, G. C., Misselt, K. A., Land olt, A. U., and Wolff, M. J. (2003). A Quantitative Comparison of the Small Magellanic Cloud, Large Magellanic Cloud, and Milky Way Ultraviolet to Near-Infrared Extinction Curves. *ApJ*, 594(1):279–293.

Górski, M., Zgirski, B., Pietrzyński, G., Gieren, W., Wielgórski, P., Graczyk, D., Kudritzki, R.-P., Pilecki, B., Narloch, W., Karczmarek, P., Suchomska, K., and Taormina, M. (2020). Empirical Calibration of the Reddening Maps in the Magellanic Clouds. *ApJ*, 889(2):179.

Gottlieb, C. A., Decin, L., Richards, A. M. S., De Ceuster, F., Homan, W., Wallström, S. H. J., Danilovich, T., Millar, T. J., Montargès, M., Wong, K. T., McDonald, I., Baudry, A., Bolte, J., Cannon, E., De Beck, E., de Koter, A., El Mellah, I., Etoka, S., Gobrecht, D., Gray, M., Herpin, F., Jeste, M., Kervella, P., Khouri, T., Lagadec, E., Maes, S., Malfait, J., Menten, K. M., Müller, H. S. P., Pimpanuwat, B., Plane, J. M. C., Sahai, R., Van de Sande, M., Waters, L. B. F. M., Yates, J., and Zijlstra, A. (2022). ATOMIUM: ALMA tracing the origins of molecules in dust forming oxygen rich M-type stars. Motivation, sample, calibration, and initial results. *A&A*, 660:A94.

Graczyk, D., Pietrzyński, G., Thompson, I. B., Gieren, W., Pilecki, B., Konorski, P., Udalski, A., Soszyński, I., Villanova, S., Górski, M., Suchomska, K., Karczmarek, P., Kudritzki, R.-P., Bresolin, F., and Gallenne, A. (2014). The Araucaria Project. The Distance to the Small Magellanic Cloud from Late-type Eclipsing Binaries. *ApJ*, 780(1):59.

Gravity Collaboration, Abuter, R., Accardo, M., Amorim, A., Anugu, N., Ávila, G., Azouaoui, N., Benisty, M., Berger, J. P., Blind, N., Bonnet, H., Bourget, P., Brandner, W., Brast, R., Buron, A., Burtscher, L., Cassaing, F., Chapron, F., Choquet, É., Clénet, Y., Collin, C., Coudé Du Foresto, V., de Wit, W., de Zeeuw, P. T., Deen, C., Delplancke-Ströbele, F., Dembet, R., Derie, F., Dexter, J., Duvert, G., Ebert, M., Eckart, A., Eisenhauer, F., Esselborn, M., Fédou, P., Finger, G., Garcia, P., Garcia Dabo, C. E., Garcia Lopez, R., Gendron, E., Genzel, R., Gillessen, S., Gonte, F., Gordo, P., Grould, M., Grözinger, U., Guieu, S., Haguenauer, P., Hans, O., Haubois, X., Haug, M., Haussmann,

F., Henning, T., Hippler, S., Horrobin, M., Huber, A., Hubert, Z., Hubin, N., Hummel, C. A., Jakob, G., Janssen, A., Jochum, L., Jocou, L., Kaufer, A., Kellner, S., Kendrew, S., Kern, L., Kervella, P., Kiekebusch, M., Klein, R., Kok, Y., Kolb, J., Kulas, M., Lacour, S., Lapeyrère, V., Lazareff, B., Le Bouquin, J. B., Lèna, P., Lenzen, R., Lévêque, S., Lippa, M., Magnard, Y., Mehrgan, L., Mellein, M., Mérand, A., Moreno-Ventas, J., Moulin, T., Müller, E., Müller, F., Neumann, U., Oberti, S., Ott, T., Pallanca, L., Panduro, J., Pasquini, L., Paumard, T., Percheron, I., Perraut, K., Perrin, G., Pflüger, A., Pfuhl, O., Phan Duc, T., Plewa, P. M., Popovic, D., Rabien, S., Ramírez, A., Ramos, J., Rau, C., Riquelme, M., Rohloff, R. R., Rousset, G., Sanchez-Bermudez, J., Scheithauer, S., Schöller, M., Schuhler, N., Spyromilio, J., Straubmeier, C., Sturm, E., Suarez, M., Tristram, K. R. W., Ventura, N., Vincent, F., Waisberg, I., Wank, I., Weber, J., Wieprecht, E., Wiest, M., Wiezorrek, E., Wittkowski, M., Woillez, J., Wolff, B., Yazici, S., Ziegler, D., and Zins, G. (2017). First light for GRAVITY: Phase referencing optical interferometry for the Very Large Telescope Interferometer. *A&A*, 602:A94.

Groenewegen, M. A. T., Sloan, G. C., Soszyński, I., and Petersen, E. A. (2009). Luminosities and mass-loss rates of SMC and LMC AGB stars and red supergiants. *A&A*, 506(3):1277–1296.

Groh, J. H., Ekström, S., Georgy, C., Meynet, G., Choplin, A., Eggenberger, P., Hirschi, R., Maeder, A., Murphy, L. J., Boian, I., and Farrell, E. J. (2019). Grids of stellar models with rotation. IV. Models from 1.7 to 120 M_{okay} at a metallicity Z = 0.0004. *A&A*, 627:A24.

Guinan, E. F., Wasatonic, R. J., and Calderwood, T. J. (2019). The Fainting of the Nearby Red Supergiant Betelgeuse. *The Astronomer's Telegram*, 13341:1.

Gustafsson, B., Edvardsson, B., Eriksson, K., Jørgensen, U. G., Nordlund, Å., and Plez, B. (2008). A grid of MARCS model atmospheres for late-type stars. I. Methods and general properties. *A&A*, 486(3):951–970.

Hansen, C., Kawaler, S., and Trimble, V. (2012). *Stellar Interiors: Physical Principles, Structure, and Evolution.* Astronomy and Astrophysics Library. Springer New York.

Harper, G. M., Brown, A., and Lim, J. (2001). A Spatially Resolved, Semiempirical Model for the Extended Atmosphere of α Orionis (M2 Iab). *ApJ*, 551(2):1073–1098.

Hauschildt, P. H. and Baron, E. (1999). Numerical solution of the expanding stellar atmosphere problem. *Journal of Computational and Applied Mathematics*, 109(1):41–63.

Hayashi, C. and Hoshi, R. (1961). The Outer Envelope of Giant Stars with Surface Convection Zone. *PASJ*, 13:442–449.

Heger, A., Fryer, C. L., Woosley, S. E., Langer, N., and Hartmann, D. H. (2003). How Massive Single Stars End Their Life. *ApJ*, 591(1):288–300.

Hirschi, R., Maeder, A., Meynet, G., Chiappini, C., and Ekström, S. (2007). Evolution of the First Stellar Generations. In Emsellem, E., Wozniak, H., Massacrier, G., Gonzalez, J. F., Devriendt, J., and Champavert, N., editors, *EAS Publications Series*, volume 24 of *EAS Publications Series*, pages 263–268.

Hirschi, R., Meynet, G., and Maeder, A. (2004). Stellar evolution with rotation. XII. Pre-supernova models. *A&A*, 425:649–670.

Höfner, S. and Olofsson, H. (2018). Mass loss of stars on the asymptotic giant branch. Mechanisms, models and measurements. *A&A Rev.*, 26(1):1.

Humphreys, R. M. and Davidson, K. (1979). Studies of luminous stars in nearby galaxies. III. Comments on the evolution of the most massive stars in the Milky Way and the Large Magellanic Cloud. *ApJ*, 232:409–420.

Humphreys, R. M. and Jones, T. J. (2022). Episodic Gaseous Outflows and Mass Loss from Red Supergiants. *AJ*, 163(3):103.

Humphreys, R. M., Strecker, D. W., and Ney, E. P. (1972). Spectroscopic and Photometric Observations of M Supergiants in Carina. *ApJ*, 172:75.

Ivezic, Z. and Elitzur, M. (1997). Self-similarity and scaling behaviour of infrared emission from radiatively heated dust - I. Theory. *MNRAS*, 287(4):799–811.

Ivezic, Z., Nenkova, M., and Elitzur, M. (1999). DUSTY: Radiation transport in a dusty environment.

Jones, A., Noll, S., Kausch, W., Szyszka, C., and Kimeswenger, S. (2013). An advanced scattered moonlight model for Cerro Paranal. *A&A*, 560:A91.

Josselin, E. and Plez, B. (2007). Atmospheric dynamics and the mass loss process in red supergiant stars. *A&A*, 469(2):671–680.

Kaeufl, H.-U., Ballester, P., Biereichel, P., Delabre, B., Donaldson, R., Dorn, R., Fedrigo, E., Finger, G., Fischer, G., Franza, F., Gojak, D., Huster, G., Jung, Y., Lizon, J.-L., Mehrgan, L., Meyer, M., Moorwood, A., Pirard, J.-F., Paufique, J., Pozna, E., Siebenmorgen, R., Silber, A., Stegmeier, J., and Wegerer, S. (2004). CRIRES: a high-resolution infrared spectrograph for ESO's VLT. In Moorwood, A. F. M. and Iye, M., editors, *Ground-based Instrumentation for Astronomy*, volume 5492 of *Society of Photo-Optical Instrumentation Engineers (SPIE) Conference Series*, pages 1218–1227.

Karovicova, I., Wittkowski, M., Ohnaka, K., Boboltz, D. A., Fossat, E., and Scholz, M. (2013). New insights into the dust formation of oxygen-rich AGB stars. *A&A*, 560:A75.

Kee, N. D., Sundqvist, J. O., Decin, L., de Koter, A., and Sana, H. (2021). Analytic, dust-independent mass-loss rates for red supergiant winds initiated by turbulent pressure. *A&A*, 646:A180.

Keenan, P. C. and McNeil, R. C. (1989). The Perkins Catalog of Revised MK Types for the Cooler Stars. *ApJS*, 71:245.

Kervella, P., Decin, L., Richards, A. M. S., Harper, G. M., McDonald, I., O'Gorman, E., Montargès, M., Homan, W., and Ohnaka, K. (2018). The close circumstellar environment of Betelgeuse. V. Rotation velocity and molecular envelope properties from ALMA. *A&A*, 609:A67.

Kirchhoff, G. (1862). Sullo spettro solare, e sugli spettri degli elementi chimici. *Il Nuovo Cimento*, 16(1):209–232.

Kravchenko, K., Wittkowski, M., Jorissen, A., Chiavassa, A., Van Eck, S., Anderson, R. I., Freytag, B., and Käufl, U. (2020). Tomography of cool giant and supergiant star atmospheres. III. Validation of the method on VLTI/AMBER observations of the Mira star S Ori. *A&A*, 642:A235.

Kudritzki, R.-P. and Puls, J. (2000). Winds from Hot Stars. *ARA&A*, 38:613–666.

Lapeyrere, V., Kervella, P., Lacour, S., Azouaoui, N., Garcia-Dabo, C. E., Perrin, G., Eisenhauer, F., Perraut, K., Straubmeier, C., Amorim, A., and Brandner, W. (2014). GRAVITY data reduction software. In Rajagopal, J. K., Creech-Eakman, M. J., and Malbet, F., editors, *Optical and Infrared Interferometry IV*, volume 9146 of *Society of Photo-Optical Instrumentation Engineers (SPIE) Conference Series*, page 91462D.

Lardo, C., Davies, B., Kudritzki, R. P., Gazak, J. Z., Evans, C. J., Patrick, L. R., Bergemann, M., and Plez, B. (2015). Red Supergiants as Cosmic Abundance Probes: The First Direct Metallicity Determination of NGC 4038 in the Antennae. *ApJ*, 812(2):160.

Le Bouquin, J. B., Berger, J. P., Lazareff, B., Zins, G., Haguenauer, P., Jocou, L., Kern, P., Millan-Gabet, R., Traub, W., Absil, O., Augereau, J. C., Benisty, M., Blind, N., Bonfils, X., Bourget, P., Delboulbe, A., Feautrier, P., Germain, M., Gitton, P., Gillier, D., Kiekebusch, M., Kluska, J., Knudstrup, J., Labeye, P., Lizon, J. L., Monin, J. L., Magnard, Y., Malbet, F., Maurel, D., Ménard, F., Micallef, M., Michaud, L., Montagnier, G., Morel, S., Moulin, T., Perraut, K., Popovic, D., Rabou, P., Rochat, S., Rojas, C., Roussel, F., Roux, A., Stadler, E., Stefl, S., Tatulli, E., and Ventura, N. (2011). PIONIER: a 4-telescope visitor instrument at VLTI. *A&A*, 535:A67.

Levesque, E. (2015). Mass Loss in Massive Stars Across the H-R Diagram: Transients, Dust Production, and the End Stages of Stellar Evolution. In *IAU General Assembly*, volume 29, page 2258458.

Levesque, E. M. and Massey, P. (2012). Spectral Types of Red Supergiants in NGC 6822 and the Wolf-Lundmark-Melotte Galaxy. *AJ*, 144(1):2.

Levesque, E. M., Massey, P., Olsen, K. A. G., and Plez, B. (2007a). Late-Type Red Supergiants: Too Cool for the Magellanic Clouds? *ApJ*, 667(1):202–212.

Levesque, E. M., Massey, P., Olsen, K. A. G., and Plez, B. (2007b). The Coolest Stars in the Clouds: Unusual Red Supergiants in the Magellanic Clouds. *arXiv e-prints*, page arXiv:0708.2914.

Levesque, E. M., Massey, P., Olsen, K. A. G., and Plez, B. (2009). *The Coolest Stars in the Clouds: Unusual Red Supergiants in the Magellanic Clouds*, volume 412 of *Astronomical Society of the Pacific Conference Series*, page 33.

Levesque, E. M., Massey, P., Olsen, K. A. G., Plez, B., Josselin, E., Maeder, A., and Meynet, G. (2005). The Effective Temperature Scale of Galactic Red Supergiants: Cool, but Not As Cool As We Thought. *ApJ*, 628(2):973–985.

Levesque, E. M., Massey, P., Olsen, K. A. G., Plez, B., Meynet, G., and Maeder, A. (2006). The Effective Temperatures and Physical Properties of Magellanic Cloud Red Supergiants: The Effects of Metallicity. *ApJ*, 645(2):1102–1117.

Levesque, E. M., Massey, P., Żytkow, A. N., and Morrell, N. (2015). Discovery of a Thorne-Żytkow object candidate in the Small Magellanic Cloud. In Meynet, G., Georgy, C., Groh, J., and Stee, P., editors, *New Windows on Massive Stars*, volume 307 of *IAU Symposium*, pages 57–63.

Lim, J., Carilli, C. L., White, S. M., Beasley, A. J., and Marson, R. G. (1998). Large convection cells as the source of Betelgeuse's extended atmosphere. *Nature*, 392(6676):575–577.

Lopez, B., Lagarde, S., Jaffe, W., Petrov, R., Schöller, M., Antonelli, P., Beckmann, U., Berio, P., Bettonvil, F., Glindemann, A., Gonzalez, J. C., Graser, U., Hofmann, K. H., Millour, F., Robbe-Dubois, S., Venema, L., Wolf, S., Henning, T., Lanz, T., Weigelt, G., Agocs, T., Bailet, C., Bresson, Y., Bristow, P., Dugué, M., Heininger, M., Kroes, G., Laun, W., Lehmitz, M., Neumann, U., Augereau, J. C., Avila, G., Behrend, J., van Belle, G., Berger, J. P., van Boekel, R., Bonhomme, S., Bourget, P., Brast, R., Clausse, J. M., Connot, C., Conzelmann, R., Cruzalèbes, P., Csepany, G., Danchi, W., Delbo, M., Delplancke, F., Dominik, C., van Duin, A., Elswijk, E., Fantei, Y., Finger, G., Gabasch, A., Gay, J., Girard, P., Girault, V., Gitton, P., Glazenborg, A., Gonté, F., Guitton, F., Guniat, S., De Haan, M., Haguenauer, P., Hanenburg, H., Hogerheijde, M., ter Horst, R., Hron, J., Hugues, Y., Hummel, C., Idserda, J., Ives, D., Jakob, G., Jasko, A., Jolley, P., Kiraly, S., Köhler, R., Kragt, J., Kroener, T., Kuindersma, S., Labadie, L., Leinert, C., Le Poole, R., Lizon, J. L., Lucuix, C., Marcotto, A., Martinache, F., Martinot-Lagarde, G., Mathar, R., Matter, A., Mauclert, N., Mehrgan, L., Meilland, A., Meisenheimer, K., Meisner, J., Mellein, M., Menardi, S., Menut, J. L., Merand, A., Morel, S., Mosoni, L., Navarro, R., Nussbaum, E., Ottogalli, S., Palsa, R., Panduro, J., Pantin, E., Parra, T., Percheron, I., Duc, T. P., Pott, J. U., Pozna, E., Przygodda, F., Rabbia, Y., Richichi, A., Rigal, F., Roelfsema, R., Rupprecht, G., Schertl, D., Schmidt, C., Schuhler, N., Schuil, M., Spang, A., Stegmeier, J., Thiam, L., Tromp, N., Vakili, F., Vannier, M., Wagner, K., and Woillez, J. (2014). An Overview of the MATISSE Instrument — Science, Concept and Current Status. *The Messenger*, 157:5–12.

Lopez, B., Lagarde, S., Petrov, R. G., Jaffe, W., Antonelli, P., Allouche, F., Berio, P., Matter, A., Meilland, A., Millour, F., Robbe-Dubois, S., Henning, T., Weigelt, G., Glindemann, A., Agocs, T., Bailet, C., Beckmann, U., Bettonvil, F., van Boekel, R., Bourget, P., Bresson, Y., Bristow, P., Cruzalèbes, P., Eldswijk, E., Fanteï Caujolle, Y., González Herrera, J. C., Graser, U., Guajardo,

P., Heininger, M., Hofmann, K. H., Kroes, G., Laun, W., Lehmitz, M., Leinert, C., Meisenheimer, K., Morel, S., Neumann, U., Paladini, C., Percheron, I., Riquelme, M., Schoeller, M., Stee, P., Venema, L., Woillez, J., Zins, G., Ábrahám, P., Abadie, S., Abuter, R., Accardo, M., Adler, T., Alonso, J., Augereau, J. C., Böhm, A., Bazin, G., Beltran, J., Bensberg, A., Boland, W., Brast, R., Burtscher, L., Castillo, R., Chelli, A., Cid, C., Clausse, J. M., Connot, C., Conzelmann, R. D., Danchi, W. C., Delbo, M., Drevon, J., Dominik, C., van Duin, A., Ebert, M., Eisenhauer, F., Flament, S., Frahm, R., Gámez Rosas, V., Gabasch, A., Gallenne, A., Garces, E., Girard, P., Glazenborg, A., Gonté, F. Y. J., Guitton, F., de Haan, M., Hanenburg, H., Haubois, X., Hocdé, V., Hogerheijde, M., ter Horst, R., Hron, J., Hummel, C. A., Hubin, N., Huerta, R., Idserda, J., Isbell, J. W., Ives, D., Jakob, G., Jaskó, A., Jochum, L., Klarmann, L., Klein, R., Kragt, J., Kuindersma, S., Kokoulina, E., Labadie, L., Lacour, S., Leftley, J., Le Poole, R., Lizon, J. L., Lopez, M., Lykou, F., Mérand, A., Marcotto, A., Mauclert, N., Maurer, T., Mehrgan, L. H., Meisner, J., Meixner, K., Mellein, M., Menut, J. L., Mohr, L., Mosoni, L., Navarro, R., Nußbaum, E., Pallanca, L., Pantin, E., Pasquini, L., Phan Duc, T., Pott, J. U., Pozna, E., Richichi, A., Ridinger, A., Rigal, F., Rivinius, T., Roelfsema, R., Rohloff, R. R., Rousseau, S., Salabert, D., Schertl, D., Schuhler, N., Schuil, M., Shabun, K., Soulain, A., Stephan, C., Toledo, P., Tristram, K., Tromp, N., Vakili, F., Varga, J., Vinther, J., Waters, L. B. F. M., Wittkowski, M., Wolf, S., Wrhel, F., and Yoffe, G. (2022). MATISSE, the VLTI mid-infrared imaging spectrointerferometer. *A&A*, 659:A192.

López Ariste, A., Georgiev, S., Mathias, P., Lèbre, A., Wavasseur, M., Josselin, E., Konstantinova-Antova, R., and Roudier, T. (2022). Three-dimensional imaging of convective cells in the photosphere of Betelgeuse. *A&A*, 661:A91.

Maeder, A. (1999). Massive Star Fromation and Evolution in Local Group Galaxies: Successes and Difficulties. In Whitelock, P. and Cannon, R., editors, *The Stellar Content of Local Group Galaxies*, volume 192 of *IAU Symposium*, page 291.

Maeder, A. and Meynet, G. (2001). Stellar evolution with rotation. VII. . Low metallicity models and the blue to red supergiant ratio in the SMC. *A&A*, 373:555–571.

Magic, Z., Weiss, A., and Asplund, M. (2015). The Stagger-grid: A grid of 3D stellar atmosphere models. III. The relation to mixing length convection theory. *A&A*, 573:A89.

Malbet, F. and Perrin, G. (2007). Foreword: Proceedings of the Euro Summer School "Observation and Data Reduction with with the VLT Interferometer" (¡A href="http://vltischool.obs.ujf-grenoble.fr"¿http://vltischool.obs.ujf-grenoble.fr¡/A¿). *New A Rev.*, 51(8-9):563–564.

McConnachie, A. W. (2012). The Observed Properties of Dwarf Galaxies in and around the Local Group. *AJ*, 144(1):4.

McConnachie, A. W., Irwin, M. J., Ferguson, A. M. N., Ibata, R. A., Lewis, G. F., and Tanvir, N. (2005). Distances and metallicities for 17 Local Group galaxies. *MNRAS*, 356(3):979–997.

McDonald, S. L. E., Davies, B., and Beasor, E. R. (2022). Red supergiants in M31: the Humphreys-Davidson limit at high metallicity. *MNRAS*, 510(3):3132–3144.

McMahon, R. G., Banerji, M., Gonzalez, E., Koposov, S. E., Bejar, V. J., Lodieu, N., Rebolo, R., and VHS Collaboration (2013). First Scientific Results from the VISTA Hemisphere Survey (VHS). *The Messenger*, 154:35–37.

Mell, P. and Grance, T. (2011). The nist definition of cloud computing.

Melotte, P. J. (1926). New nebulæ shown on Franklin-Adams chart plates. *MNRAS*, 86:636–638.

Meynet, G., Chomienne, V., Ekström, S., Georgy, C., Granada, A., Groh, J., Maeder, A., Eggenberger, P., Levesque, E., and Massey, P. (2015). Impact of mass-loss on the evolution and pre-supernova properties of red supergiants. *A&A*, 575:A60.

Meynet, G., Eggenberger, P., Ekström, S., Georgy, C., Groh, J., Maeder, A., Saio, H., and Moriya, T. (2013a). Four open questions in massive star evolution. In Alecian, G., Lebreton, Y., Richard, O., and Vauclair, G., editors, *EAS Publications Series*, volume 63 of *EAS Publications Series*, pages 373–383.

Meynet, G., Georgy, C., Hirschi, R., Maeder, A., Massey, P., Przybilla, N., and Nieva, M. F. (2011). Red Supergiants, Luminous Blue Variables and Wolf-Rayet stars: the single massive star perspective. *Bulletin de la Societe Royale des Sciences de Liege*, 80:266–278.

Meynet, G., Haemmerlé, L., Ekström, S., Georgy, C., Groh, J., and Maeder, A. (2013b). The past and future evolution of a star like Betelgeuse. In Kervella, P., Le Bertre, T., and Perrin, G., editors, *EAS Publications Series*, volume 60 of *EAS Publications Series*, pages 17–28.

Meynet, G. and Maeder, A. (2000). Stellar evolution with rotation. V. Changes in all the outputs of massive star models. *A&A*, 361:101–120.

Meynet, G. and Maeder, A. (2002). Stellar evolution with rotation. VIII. Models at Z = 10^{-5} and CNO yields for early galactic evolution. *A&A*, 390:561–583.

Meynet, G., Maeder, A., Georgy, C., Ekström, S., Eggenberger, P., Barblan, F., and Song, H. F. (2017). Massive stars, successes and challenges. In Eldridge, J. J., Bray, J. C., McClelland, L. A. S., and Xiao, L., editors, *The Lives and Death-Throes of Massive Stars*, volume 329 of *IAU Symposium*, pages 3–14.

Mihalas, D. (1978). *Stellar atmospheres*.

Millour, F., Berio, P., Heininger, M., Hofmann, K. H., Schertl, D., Weigelt, G., Guitton, F., Jaffe, W., Beckmann, U., Petrov, R., Allouche, F., Robbe-Dubois, S., Lagarde, S., Soulain, A., Meilland, A., Matter, A., Cruzalèbes, P., and Lopez, B. (2016). Data reduction for the MATISSE instrument. In Malbet, F., Creech-Eakman, M. J., and Tuthill, P. G., editors, *Optical and Infrared Interferometry and Imaging V*, volume 9907 of *Society of Photo-Optical Instrumentation Engineers (SPIE) Conference Series*, page 990723.

Minniti, D. and Zijlstra, A. A. (1997). Stellar Populations of the Dwarf Irregular Galaxy WLM. *AJ*, 114:147–160.

Modigliani, A., Goldoni, P., Royer, F., Haigron, R., Guglielmi, L., François, P., Horrobin, M., Bristow, P., Vernet, J., Moehler, S., Kerber, F., Ballester, P., Mason, E., and Christensen, L. (2010). The X-shooter pipeline. In *Proc. SPIE*, volume 7737 of *Society of Photo-Optical Instrumentation Engineers (SPIE) Conference Series*, page 773728.

Monnier, J. D. (2007). Phases in interferometry. *New A Rev.*, 51(8-9):604–616.

Monnier, J. D., Tuthill, P. G., Lopez, B., Cruzalebes, P., Danchi, W. C., and Haniff, C. A. (1999). The Last Gasps of VY Canis Majoris: Aperture Synthesis and Adaptive Optics Imagery. *ApJ*, 512(1):351–361.

Montargès, M., Cannon, E., de Koter, A., Khouri, T., Lagadec, E., Kervella, P., Decin, L., McDonald, I., Homan, W., Waters, L. B. F. M., Sahai, R., Gottlieb, C. A., Malfait, J., Maes, S., Pimpanuwat, B., Jeste, M., Danilovich, T., De Ceuster, F., Van de Sande, M., Gobrecht, D., Wallström, S. H. J., Wong, K. T., El Mellah, I., Bolte, J., Herpin, F., Richards, A. M. S., Baudry, A., Etoka, S., Gray, M. D., Millar, T. J., Menten, K. M., Müller, H. S. P., Plane, J. M. C., Yates, J., and Zijlstra, A. (2023). The VLT/SPHERE view of the ATOMIUM cool evolved star sample. I. Overview: Sample characterization through polarization analysis. *arXiv e-prints*, page arXiv:2301.02081.

Montargès, M., Cannon, E., Lagadec, E., de Koter, A., Kervella, P., Sanchez-Bermudez, J., Paladini, C., Cantalloube, F., Decin, L., Scicluna, P., Kravchenko, K., Dupree, A. K., Ridgway, S., Wittkowski, M., Anugu, N., Norris, R., Rau, G., Perrin, G., Chiavassa, A., Kraus, S., Monnier, J. D., Millour, F., Le Bouquin, J. B., Haubois, X., Lopez, B., Stee, P., and Danchi, W. (2021). A dusty veil shading Betelgeuse during its Great Dimming. *Nature*, 594(7863):365–368.

Montargès, M., Chiavassa, A., Kervella, P., Ridgway, S. T., Perrin, G., Le Bouquin, J. B., and Lacour, S. (2017). The convective surface of the red supergiant Antares. VLTI/PIONIER interferometry in the near infrared. *A&A*, 605:A108.

Montargès, M., Kervella, P., Perrin, G., Ohnaka, K., Chiavassa, A., Ridgway, S. T., and Lacour, S. (2014). Properties of the CO and H_2O MOLsphere of the red supergiant Betelgeuse from VLTI/AMBER observations. *A&A*, 572:A17.

Montargès, M., Norris, R., Chiavassa, A., Tessore, B., Lèbre, A., and Baron, F. (2018). The convective photosphere of the red supergiant CE Tauri. I. VLTI/-PIONIER H-band interferometric imaging. *A&A*, 614:A12.

Noll, S., Kausch, W., Barden, M., Jones, A. M., Szyszka, C., Kimeswenger, S., and Vinther, J. (2012). An atmospheric radiation model for Cerro Paranal. I. The optical spectral range. *A&A*, 543:A92.

Ochsenbein, F., Bauer, P., and Marcout, J. (2000). The VizieR database of astronomical catalogues. *A&AS*, 143:23–32.

O'Gorman, E., Harper, G. M., Ohnaka, K., Feeney-Johansson, A., Wilkeneit-Braun, K., Brown, A., Guinan, E. F., Lim, J., Richards, A. M. S., Ryde, N.,

and Vlemmings, W. H. T. (2020). ALMA and VLA reveal the lukewarm chromospheres of the nearby red supergiants Antares and Betelgeuse. *A&A*, 638:A65.

O'Gorman, E., Kervella, P., Harper, G. M., Richards, A. M. S., Decin, L., Montargès, M., and McDonald, I. (2017). The inhomogeneous submillimeter atmosphere of Betelgeuse. *A&A*, 602:L10.

Ohnaka, K. (2014). High spectral resolution spectroscopy of the SiO fundamental lines in red giants and red supergiants with VLT/VISIR. *A&A*, 561:A47.

Ohnaka, K., Hofmann, K. H., Benisty, M., Chelli, A., Driebe, T., Millour, F., Petrov, R., Schertl, D., Stee, P., Vakili, F., and Weigelt, G. (2009). Spatially resolving the inhomogeneous structure of the dynamical atmosphere of Betelgeuse with VLTI/AMBER. *A&A*, 503(1):183–195.

Ohnaka, K., Hofmann, K. H., Schertl, D., Weigelt, G., Baffa, C., Chelli, A., Petrov, R., and Robbe-Dubois, S. (2013). High spectral resolution imaging of the dynamical atmosphere of the red supergiant Antares in the CO first overtone lines with VLTI/AMBER. *A&A*, 555:A24.

Ohnaka, K., Weigelt, G., Millour, F., Hofmann, K. H., Driebe, T., Schertl, D., Chelli, A., Massi, F., Petrov, R., and Stee, P. (2011). Imaging the dynamical atmosphere of the red supergiant Betelgeuse in the CO first overtone lines with VLTI/AMBER. *A&A*, 529:A163.

Paczyński, B. (1970). Evolution of Single Stars. I. Stellar Evolution from Main Sequence to White Dwarf or Carbon Ignition. *Acta Astron.*, 20:47.

Paladini, C., Klotz, D., Sacuto, S., Lagadec, E., Wittkowski, M., Richichi, A., Hron, J., Jorissen, A., Groenewegen, M. A. T., Kerschbaum, F., Verhoelst, T., Rau, G., Olofsson, H., Zhao-Geisler, R., and Matter, A. (2017). The VLTI/MIDI view on the inner mass loss of evolved stars from the Herschel MESS sample. *A&A*, 600:A136.

Paxton, B., Bildsten, L., Dotter, A., Herwig, F., Lesaffre, P., and Timmes, F. (2011). Modules for Experiments in Stellar Astrophysics (MESA). *ApJS*, 192(1):3.

Perrin, G. (2003). The calibration of interferometric visibilities obtained with single-mode optical interferometers. Computation of error bars and correlations. *A&A*, 400:1173–1181.

Perrin, G., Verhoelst, T., Ridgway, S. T., Cami, J., Nguyen, Q. N., Chesneau, O., Lopez, B., Leinert, C., and Richichi, A. (2007). The molecular and dusty composition of Betelgeuse's inner circumstellar environment. *A&A*, 474(2):599–608.

Pesnell, W. D., Thompson, B. J., and Chamberlin, P. C. (2012). The Solar Dynamics Observatory (SDO). *Sol. Phys.*, 275(1-2):3–15.

Petrov, R. G., Malbet, F., Weigelt, G., Antonelli, P., Beckmann, U., Bresson, Y., Chelli, A., Dugué, M., Duvert, G., Gennari, S., Glück, L., Kern, P., Lagarde, S., Le Coarer, E., Lisi, F., Millour, F., Perraut, K., Puget, P., Rantakyrö, F., Robbe-Dubois, S., Roussel, A., Salinari, P., Tatulli, E., Zins, G., Accardo, M., Acke, B., Agabi, K., Altariba, E., Arezki, B., Aristidi, E., Baffa, C., Behrend, J., Blöcker, T., Bonhomme, S., Busoni, S., Cassaing, F., Clausse, J. M., Colin, J., Connot, C., Delboulbé, A., Domiciano de Souza, A., Driebe, T., Feautrier, P., Ferruzzi, D., Forveille, T., Fossat, E., Foy, R., Fraix-Burnet, D., Gallardo, A., Giani, E., Gil, C., Glentzlin, A., Heiden, M., Heininger, M., Hernandez Utrera, O., Hofmann, K. H., Kamm, D., Kiekebusch, M., Kraus, S., Le Contel, D., Le Contel, J. M., Lesourd, T., Lopez, B., Lopez, M., Magnard, Y., Marconi, A., Mars, G., Martinot-Lagarde, G., Mathias, P., Mège, P., Monin, J. L., Mouillet, D., Mourard, D., Nussbaum, E., Ohnaka, K., Pacheco, J., Perrier, C., Rabbia, Y., Rebattu, S., Reynaud, F., Richichi, A., Robini, A., Sacchettini, M., Schertl, D., Schöller, M., Solscheid, W., Spang, A., Stee, P., Stefanini, P., Tallon, M., Tallon-Bosc, I., Tasso, D., Testi, L., Vakili, F., von der Lühe, O., Valtier, J. C., Vannier, M., and Ventura, N. (2007). AMBER, the near-infrared spectro-interferometric three-telescope VLTI instrument. *A&A*, 464(1):1–12.

Pickles, A. and Depagne, É. (2010). All-Sky Spectrally Matched UBVRI - ZY and u′ g′ r′ i′ z′ Magnitudes for Stars in the Tycho2 Catalog. *PASP*, 122(898):1437.

Pietrzyński, G., Graczyk, D., Gieren, W., Thompson, I. B., Pilecki, B., Udalski, A., Soszyński, I., Kozłowski, S., Konorski, P., Suchomska, K., Bono, G., Moroni, P. G. P., Villanova, S., Nardetto, N., Bresolin, F., Kudritzki, R. P., Storm, J., Gallenne, A., Smolec, R., Minniti, D., Kubiak, M., Szymański, M. K., Poleski, R., Wyrzykowski, Ł., Ulaczyk, K., Pietrukowicz, P., Górski, M., and Karczmarek, P. (2013). An eclipsing-binary distance to the Large Magellanic Cloud accurate to two per cent. *Nature*, 495(7439):76–79.

Planck, M. (1900). Ueber irreversible Strahlungsvorgänge. *Annalen der Physik*, 306(1):69–122.

Plez, B. (2012). Turbospectrum: Code for spectral synthesis.

Prandtl, L. (1925). 7. Bericht über Untersuchungen zur ausgebildeten Turbulenz. *Zeitschrift Angewandte Mathematik und Mechanik*, 5(2):136–139.

Puls, J., Markova, N., and Scuderi, S. (2008). Stellar Winds from Massive Stars - What are the REAL Mass-Loss Rates? In de Koter, A., Smith, L. J., and Waters, L. B. F. M., editors, *Mass Loss from Stars and the Evolution of Stellar Clusters*, volume 388 of *Astronomical Society of the Pacific Conference Series*, page 101.

Puls, J., Sundqvist, J. O., and Markova, N. (2015). Physics of Mass Loss in Massive Stars. In Meynet, G., Georgy, C., Groh, J., and Stee, P., editors, *New Windows on Massive Stars*, volume 307 of *IAU Symposium*, pages 25–36.

Rejkuba, M., Minniti, D., Gregg, M. D., Zijlstra, A. A., Alonso, M. V., and Goudfrooij, P. (2000). Deep Hubble Space Telescope STIS Color-Magnitude Diagrams of the Dwarf Irregular Galaxy WLM: Detection of the Horizontal Branch. *AJ*, 120(2):801–809.

Richards, A. M. S. and Yates, J. A. (1998). Maser Mapping of Dust-Driven Winds from Red Supergiants. *Irish Astronomical Journal*, 25:7.

Rybicki, G. B. and Lightman, A. P. (1979). *Radiative processes in astrophysics*.

Salasnich, B., Bressan, A., and Chiosi, C. (1999). Evolution of massive stars under new mass-loss rates for RSG: is the mystery of the missing blue gap solved? *A&A*, 342:131–152.

Sandage, A. and Carlson, G. (1985). The brightest stars in nearby galaxies. VI. Cepheids and the brightest stars in WLM. *AJ*, 90:1464–1473.

Sanner, F. (1976). Mass loss in the red giants and supergiants. *ApJ*, 204:L41–L45.

Schaye, J., Crain, R. A., Bower, R. G., Furlong, M., Schaller, M., Theuns, T., Dalla Vecchia, C., Frenk, C. S., McCarthy, I. G., Helly, J. C., Jenkins, A., Rosas-Guevara, Y. M., White, S. D. M., Baes, M., Booth, C. M., Camps, P., Navarro, J. F., Qu, Y., Rahmati, A., Sawala, T., Thomas, P. A., and Trayford, J.

(2015). The EAGLE project: simulating the evolution and assembly of galaxies and their environments. *MNRAS*, 446(1):521–554.

Schlafly, E., Green, G., Finkbeiner, D. P., and Rix, H. (2014). The Dust to 5 kpc from Pan-STARRS1. In *American Astronomical Society Meeting Abstracts #223*, volume 223 of *American Astronomical Society Meeting Abstracts*, page 116.04.

Schmitt, J. H. M. M., Schröder, K. P., Rauw, G., Hempelmann, A., Mittag, M., González-Pérez, J. N., Czesla, S., Wolter, U., Jack, D., Eenens, P., and Trinidad, M. A. (2014). TIGRE: A new robotic spectroscopy telescope at Guanajuato, Mexico. *Astronomische Nachrichten*, 335(8):787.

Schröder, K. P. and Cuntz, M. (2005). A New Version of Reimers' Law of Mass Loss Based on a Physical Approach. *ApJ*, 630(1):L73–L76.

Smartt, S. J. (2009). Progenitors of Core-Collapse Supernovae. *ARA&A*, 47(1):63–106.

Smith, N., Humphreys, R. M., Davidson, K., Gehrz, R. D., Schuster, M. T., and Krautter, J. (2001). The Asymmetric Nebula Surrounding the Extreme Red Supergiant VY Canis Majoris. *AJ*, 121(2):1111–1125.

Speck, A. K., Barlow, M. J., Sylvester, R. J., and Hofmeister, A. M. (2000). Dust features in the 10-mu m infrared spectra of oxygen-rich evolved stars. *A&AS*, 146:437–464.

Spitzer, L. (1978). *Physical processes in the interstellar medium*.

Tabernero, H. M., Dorda, R., Negueruela, I., and González-Fernández, C. (2018). An LTE effective temperature scale for red supergiants in the Magellanic clouds. *MNRAS*, 476(3):3106–3123.

Trampedach, R. and Stein, R. F. (2011). The Mass Mixing Length in Convective Stellar Envelopes. *ApJ*, 731(2):78.

Trampedach, R., Stein, R. F., Christensen-Dalsgaard, J., Nordlund, Å., and Asplund, M. (2014). Improvements to stellar structure models, based on a grid of 3D convection simulations - II. Calibrating the mixing-length formulation. *MNRAS*, 445(4):4366–4384.

Trundle, C., Dufton, P. L., Hunter, I., Evans, C. J., Lennon, D. J., Smartt, S. J., and Ryans, R. S. I. (2007). The VLT-FLAMES survey of massive stars: evolution of surface N abundances and effective temperature scales in the Galaxy and Magellanic Clouds. *A&A*, 471(2):625–643.

Tsuji, T. (1988). High resolution spectroscopy of CO in the infrared spectra of cool stars. II. Quasi-static molecular dissociation zone in the outer atmosphere of red giant stars. *A&A*, 197:185–199.

Tuthill, P. G., Monnier, J. D., and Danchi, W. C. (2001). A dusty torus around the luminous young star LkHα101. *Nature*, 409(6823):1012–1014.

Uitenbroek, H., Dupree, A. K., and Gilliland, R. L. (1996). Spatially resolved HST spectra of α Orionis' chromosphere. In *Bulletin of the American Astronomical Society*, volume 28, page 942.

Urbaneja, M. A., Kudritzki, R.-P., Bresolin, F., Przybilla, N., Gieren, W., and Pietrzyński, G. (2008). The Araucaria Project: The Local Group Galaxy WLM—Distance and Metallicity from Quantitative Spectroscopy of Blue Supergiants. *ApJ*, 684(1):118–135.

van Belle, G. T. (2015). Basics of Optical Interferometry: A Gentle Introduction. In Meynet, G., Georgy, C., Groh, J., and Stee, P., editors, *New Windows on Massive Stars*, volume 307, pages 252–260.

van Loon, J. T., Cioni, M. R. L., Zijlstra, A. A., and Loup, C. (2005). An empirical formula for the mass-loss rates of dust-enshrouded red supergiants and oxygen-rich Asymptotic Giant Branch stars. *A&A*, 438(1):273–289.

Vernet, J., Dekker, H., D'Odorico, S., Kaper, L., Kjaergaard, P., Hammer, F., Randich, S., Zerbi, F., Groot, P. J., Hjorth, J., Guinouard, I., Navarro, R., Adolfse, T., Albers, P. W., Amans, J. P., Andersen, J. J., Andersen, M. I., Binetruy, P., Bristow, P., Castillo, R., Chemla, F., Christensen, L., Conconi, P., Conzelmann, R., Dam, J., de Caprio, V., de Ugarte Postigo, A., Delabre, B., di Marcantonio, P., Downing, M., Elswijk, E., Finger, G., Fischer, G., Flores, H., François, P., Goldoni, P., Guglielmi, L., Haigron, R., Hanenburg, H., Hendriks, I., Horrobin, M., Horville, D., Jessen, N. C., Kerber, F., Kern, L., Kiekebusch, M., Kleszcz, P., Klougart, J., Kragt, J., Larsen, H. H., Lizon, J. L., Lucuix, C., Mainieri, V., Manuputy, R., Martayan, C., Mason, E., Mazzoleni, R., Michaelsen, N., Modigliani, A., Moehler, S., Møller, P., Norup Sørensen, A.,

Nørregaard, P., Péroux, C., Patat, F., Pena, E., Pragt, J., Reinero, C., Rigal, F., Riva, M., Roelfsema, R., Royer, F., Sacco, G., Santin, P., Schoenmaker, T., Spano, P., Sweers, E., Ter Horst, R., Tintori, M., Tromp, N., van Dael, P., van der Vliet, H., Venema, L., Vidali, M., Vinther, J., Vola, P., Winters, R., Wistisen, D., Wulterkens, G., and Zacchei, A. (2011). X-shooter, the new wide band intermediate resolution spectrograph at the ESO Very Large Telescope. *A&A*, 536:A105.

Wenger, M., Ochsenbein, F., Egret, D., Dubois, P., Bonnarel, F., Borde, S., Genova, F., Jasniewicz, G., Laloë, S., Lesteven, S., and Monier, R. (2000). The SIMBAD astronomical database. The CDS reference database for astronomical objects. *A&AS*, 143:9–22.

Wittkowski, M., Arroyo-Torres, B., Marcaide, J. M., Abellan, F. J., Chiavassa, A., and Guirado, J. C. (2017). VLTI/AMBER spectro-interferometry of the late-type supergiants V766 Cen (=HR 5171 A), σ Oph, BM Sco, and HD 206859. *A&A*, 597:A9.

Wittkowski, M., Aufdenberg, J. P., and Kervella, P. (2004). Tests of stellar model atmospheres by optical interferometry. VLTI/VINCI limb-darkening measurements of the M4 giant ψ Phe. *A&A*, 413:711–723.

Wittkowski, M., Boboltz, D. A., Ohnaka, K., Driebe, T., and Scholz, M. (2007). The Mira variable S Orionis: relationships between the photosphere, molecular layer, dust shell, and SiO maser shell at 4 epochs. *A&A*, 470(1):191–210.

Wittkowski, M., Chiavassa, A., Baron, F., Freytag, B., Höfner, S., and Paladini, C. (2021). Investigating mass loss from RSG and AGB stars using the new VLTI-MATISSE imaging instrument. In *The 20.5th Cambridge Workshop on Cool Stars, Stellar Systems, and the Sun (CS20.5)*, Cambridge Workshop on Cool Stars, Stellar Systems, and the Sun, page 310.

Wittkowski, M., Hauschildt, P. H., Arroyo-Torres, B., and Marcaide, J. M. (2012). Fundamental properties and atmospheric structure of the red supergiant VY Canis Majoris based on VLTI/AMBER spectro-interferometry. *A&A*, 540:L12.

Wittkowski, M., Rau, G., Chiavassa, A., Höfner, S., Scholz, M., Wood, P. R., de Wit, W. J., Eisenhauer, F., Haubois, X., and Paumard, T. (2018). VLTI-GRAVITY measurements of cool evolved stars. I. Variable photosphere and extended atmosphere of the Mira star R Peg. *A&A*, 613:L7.

Wolf, C., Onken, C. A., Luvaul, L. C., Schmidt, B. P., Bessell, M. S., Chang, S.-W., Da Costa, G. S., Mackey, D., Martin-Jones, T., Murphy, S. J., Preston, T., Scalzo, R. A., Shao, L., Smillie, J., Tisserand, P., White, M. C., and Yuan, F. (2018). SkyMapper Southern Survey: First Data Release (DR1). *PASA*, 35:e010.

Wolf, M. (1909). Über einen größeren Nebelfleck in Cetus. *Astronomische Nachrichten*, 183(12):187.

Wood, P. R. (1979). Pulsation and mass loss in Mira variables. *ApJ*, 227:220–231.